

Dynamic Fluid-Structure-Vehicle-Interaction Analysis for Submerged Floating Tunnels: a Comfort Assessment

Davide La Zara

Delft University of Technology

Dynamic Fluid - Structure - Vehicle - Interaction Analysis for Submerged Floating Tunnels: a Comfort Assessment

by

D. La Zara

to obtain the degree of Master of Science
at the Delft University of Technology,
to be defended publicly on Wednesday July 17, 2019 at 10:00 AM.

Student number: 4754271
Project duration: August 20, 2018 – July 31, 2019
Thesis committee: Dr. ir. K.N. van Dalen, TU Delft, chairman
Prof. Dr. ir. A.V. Metrikine, TU Delft
Dr. ir. D.J. Peters, Royal HaskoningDHV
Dr. ir. X. Chen, TEC / Royal HaskoningDHV
Ir. L.J.M. Houben, TU Delft



Keywords: dynamics, SFT, FSVI, comfort

Front & Back: D. La Zara. Cover Image by CCCC/HPDI

An electronic version of this thesis is available at <http://repository.tudelft.nl/>.



Abstract

Crossing waterways is crucial to improve transport connections. In particular, new crossing methods are needed when the distance to be covered increases. Submerged Floating Tunnel (SFT) have been recently emerging as a cost-effective feasible crossing technique to connect fjords in Norway. However, only very little research has addressed the vehicle-structure interaction, with attention to the passengers, so far. In the current thesis, an algorithm was developed to study the Fluid-Structure-Vehicle Interaction (FSVI), where the tunnel has been modelled as a Euler Bernoulli beam, the train car as a 6DOFs system, the supporting cables as linear springs, and the fluid by the Morison's hydrodynamic force expression. The Sperling ride quality and comfort indices were used to address the human comfort while crossing the tunnel. It is found that, due to low-frequency hydrodynamic environment, the influence of the FSVI on the Sperling's indices is limited, i.e. "just noticeable" from the classification table. Low-frequency flow field may cause motion sickness rather than cause comfort/discomfort during ride. The illness rating, which is the indicator of the motion sickness, gave positive outcomes due to the small amplitude of the accelerations, and therefore no illness is expected to be felt by passengers. This study shows that displacement and acceleration can be controlled and kept inside the proposed boundaries under storm sea states, and the comfort while crossing can be guaranteed. The approach here used can be applied to other sea states with higher frequency content to address the comfort in storm with smaller return period, which may also be important to address the fatigue resistance of the structure.

Acknowledgements

July 17th 2019. This is going to be a day that I will not forget. Today a big chapter of my life closes. A chapter that started more than twenty years ago in kindergarten and leads me here. I feel blessed for the possibility of concluding this path in such a grateful university as TU Delft. The last two years have been as full of memories as hard work. But of course, none of this would have been possible without the support of those who accompanied me through the years.

The first and biggest thank you goes to my parents, whose unconditional love and support allow me living this incredible adventure of studying abroad. I owe a lot of gratitude to my brother, whose presence here made everything easier since the day it started, as it made it feel more home. Also, I cannot forget to mention the last member of the family, my beloved dog, my shade wherever I go, who gives the warmest welcome every time I go back home.

I want to thank the second family, my friends, all of them from the ones I talk almost every day to the ones I occasionally call or text. To my dears Eleonora and Ilaria, two of the most wonderful people I have ever met, who continuously support me since high school. From Francesca, Giulia, Gianluca and Arianna with whom I started this Dutch life partying at the introduction programme, to the Greek, Spanish and Structural Engineering families with which I have shared countless dinners, Italian cuisine based, beers and parties. I also feel lucky for the chance of having Daniela, from the Sapienza team, here for a semester. I can not forget to mention the rest of the team: Riccardo, Flavio, Andrea, Yvonne, Anna, Giorgia, Giulia, Alessandra, Benedetta, Gabriele, Gianluca, Ludovico, Livio, Lorenzo, Martina, Valeria, Giorgio, Valerio, Alessio, Andrea; all of you have been close to me in all the good and the bad times and I am blessed for having in my life and for calling you my friends.

I would also like to thank TU Delft for giving me the chance to conclude my studies here and all the professors and fellow students that helped me during these master programme and made the transition to this new university softer. To my university supervisors and engineers at Royal HaskoningDHV for letting me participate in this research about the submerged floating tunnel and for teaching how to organise a research.

I will come full circle by thanking the rest of my family, in particular, my grandparents who more than anyone taught me the importance of the family and share the love with each other. Another thank you goes to my aunts who helped me cultivate my second passion, cooking, allowing me to join the Christmas cook-off.

Thank you.

Contents

List of Figures	ix
List of Tables	xi
1 Introduction	1
1.1 The Submerged Floating Tunnel (SFT): a new concept for crossing waterways	1
1.2 Structural Features	2
1.2.1 Structural requirements	2
1.2.2 Construction materials.	4
1.2.3 SFT module configuration	5
1.2.4 Anchoring System	6
1.3 Traffic Load	8
1.4 Problem Definition	9
1.5 Scope	9
1.6 Approach	9
1.7 Assumptions	10
2 Structural Loads	11
2.1 Introduction	11
2.2 Permanent Load	11
2.3 Variable/Functional Load	12
2.4 Environmental Load	12
2.4.1 Tide	12
2.4.2 Current	12
2.4.3 Wave.	12
2.4.4 Hydrodynamic Forces	14
2.4.5 Accidental Load	16
3 Ride Comfort	19
3.1 Introduction	19
3.2 Ride Quality.	19
3.3 Ride Comfort	20
4 Methodology	23
4.1 Introduction	23
4.2 Vehicle Model.	23
4.2.1 Moving Load	23
4.2.2 Moving Mass.	23
4.2.3 Moving Sprung Mass.	24
4.2.4 Moving Train Car.	24
4.2.5 Moving Train Car with Rail Irregularities	24
4.3 Tunnel Model	25
4.3.1 Simply Supported SFT	25
4.3.2 Cable Supported SFT.	25
4.4 Fluid-Structure-Vehicle Interaction	27
4.5 Solution Method	27
4.6 Simulation Method	29

5	Case Study	31
5.1	Introduction	31
5.2	Cross-Section Geometry and Dimension	31
5.3	Tunnel Arrangement	32
5.3.1	Modal Analysis.	34
5.4	Cable Properties	35
5.5	Sea Loading.	36
5.6	Train Car Parameters	40
5.7	Longitudinal Rail Defect	42
6	Results	43
6.1	Introduction	43
6.2	Influence of the Vehicle Model	43
6.3	Influence of the Cable Inclination.	48
6.4	Influence of the Load Case	49
6.5	Influence of the Rail Irregularity together with Load Case.	52
6.6	Influence of the Amplitude and Wavelength of the Rail Irregularity	54
6.7	Influence of the Damping of the Suspension Systems.	55
6.8	Influence of the Whole Train	58
6.9	Concluding remarks	61
7	Discussion of Results	63
7.1	Introduction	63
7.2	Structural Behaviour	63
7.3	Motion Sickness.	66
7.4	Comfort and Exposure Limit	67
8	Conclusions and Recommendations	69
8.1	Conclusions.	69
8.2	Recommendations	70
A	Solution of Dynamic Bending Vibration of Euler-Bernoulli Beam	75
B	Determination of cable stiffness	77
B.1	Vertical Cables Stiffness in Sway Motion	77
B.2	Vertical Cables Stiffness in Heave Motion	78
B.3	Inclined Cables Stiffness in Sway Motion	78
B.4	Inclined Cables Stiffness in Heave Motion	79
C	Solution of Dynamic Bending Vibration of BOEF	81
D	FSVI using the BOES model	83
D.1	Orthogonality in y-direction	84
D.2	Orthogonality in z-direction	84
D.3	Orthogonality in ϕ -direction	85
D.4	Matrix Assembling	87
E	Train car model derivation	91
F	Train car eigenvalue problem	95

List of Figures

1.1 Akashi Kaikyō Bridge	1
1.2 Flowchart of the preliminary design procedure	3
1.3 Cost Comparison Suspension Bridge and SFT	4
1.4 SFT having circular cross-section	5
1.5 SFT having polygonal cross-section	6
1.6 SFT having circular cross-section and connected with truss	6
1.7 Supporting system of SFT.	7
1.8 Cable configurations	7
1.9 Configurations of SFT.	8
2.1 Wave profile for different theories.	13
2.2 Cable configurations	15
2.3 Wave Loading Regimes	16
2.4 SFT collision with a submarine	17
3.1 Weighting Factors	20
3.2 irregularities	21
3.3 irregularities	21
4.1 Moving load model	23
4.2 Moving mass model	23
4.3 Moving sprung mass model	24
4.4 Moving train car model	24
4.5 Moving train car model with rail irregularities	25
4.6 SFT with tensile cable	25
4.7 Beam on Discrete Elastic Supports (BOES) vs. Beam on Elastic Foundation (BOEF)	26
4.8 First 10 Mode Shapes	28
5.1 Twin-Track Bore Tunnel	31
5.2 Tunnel Arrangement	32
5.3 Cable Stiffness vs. Inclination θ	33
5.4 Natural Frequency	34
5.5 Cable Characteristic Sections	36
5.6 Pierson-Moskowitz and JONSWAP Spectra for the two significant wave heights considered	36
5.7 Wave Parameters	37
5.8 Particle velocity at tunnel location	40
5.9 Train Car	41
6.1 Midspan Response for Different Vehicle Models	45
6.2 Vehicle Critical Velocity at each mode	45
6.3 Maximum Displacement vs. Velocity at midspan	46
6.4 Maximum Displacement vs. Velocity for a BOES and a BOEF	46
6.5 Maximum Displacement vs. Velocity for different tunnel length with cable spacing $100m$	47
6.6 Displacement Envelope for $V = V_{cr}$	47
6.7 Midspan Response for Different Cable Inclination	48
6.8 Maximum Horizontal Displacement at midspan	49
6.9 Midspan Response for Different Load Cases	50
6.10 Variance Spectrum of Acceleration at midspan for different load cases	51
6.11 Midspan Vertical Acceleration Variance Spectrum	52

6.12	Variance Spectrum of Displacement for Different Load Cases	53
6.13	Variance Spectrum of Train Car Acceleration for Different Defect Amplitude and Wavelength	55
6.14	Ride Quality and Comfort Index vs. Irregularity Amplitude and Wavelength	55
6.15	Variance Spectrum of Train Car Acceleration for Different Suspension Characteristics	57
6.16	Influence of the primary and secondary suspension damping	58
6.17	Comparison Power Spectra of the Acceleration between Single and Full Train	59
6.18	Displacement Envelope	60
6.19	Moment Envelope	60
7.1	Hydrodynamic displacements along the length of the SFT with time	64
7.2	Hydrodynamic bending moments along the length of the SFT with time, Load Case 8	64
7.3	Comparison Steady-State Acceleration Amplitude Spectra at different locations	66
7.4	Standard ISO 2631 (1980) Bounds Vertical Acceleration	67
B.1	Vertical Cable Sway Motion	77
B.2	Vertical Cable Heave Motion	78
B.3	Inclined Cable Sway Motion	79
B.4	Inclined Cable Heave Motion	79
E.1	Horizontal Displacement	91

List of Tables

1.1	Limiting Deflection and Acceleration	8
2.1	Load Classification	11
3.1	Ride Quality Scale	20
3.2	Ride Comfort Scale	21
5.1	Material Properties	32
5.2	Cross-Section Dimensions	32
5.3	Cross-Section Stiffness and Permanent Loads	32
5.4	Cable Inclination and Stiffness	33
5.5	Wet Natural Frequencies	34
5.6	Dry Natural Frequencies	35
5.7	Cable Material Properties	35
5.8	Wave Parameters	36
5.9	Applicability of Morison's Formulation	37
5.10	Train Car Parameters	41
5.11	Train Car Natural Frequencies	42
5.12	Amplitude and Wavelength of the Defect as in Choi et al. [4]	42
6.1	Environmental Load Case Specification	49
6.2	Amplitude and Wavelength of the Defect	52
6.3	Damping Ratios Input	56
6.4	Sperling's Ride Quality and Comfort Indices	59
7.1	Deflection and Motion Limits	65
7.2	Illness Rating Rank	66
7.3	Illness Rating Results	67

Acronyms

SFT	Submerged Floating Tunnel
BWR	Buoyancy-to-Weight Ratio
RF	Residual Forces
RB	Residual Buoyancy
RW	Residual Weight
G_I	self-weight
$F_{buoyancy}$	upwards buoyancy force
G_{II}	ballast water
Q	Live Load
V	Volume
SF	scaling factor
FCA	Fatigue Crack Arrestor
FSI	Fluid-Structure Interaction
VSI	Vehicle-Structure Interaction
FSVI	Fluid-Structure-Vehicle Interaction
FRP	Fibre Reinforced Polymers
Re	Reynolds number
KC	Keulegan-Carpenter number
FEM	Finite Element Method
FFT	Fast Fourier Transform
FRA	Federal Railroad Administration
BOES	Beam on Discrete Elastic Supports
BOEF	Beam on Elastic Foundation
ODE	Ordinary Differential Equation
PDE	Partial Differential Equation
SDOF	Single Degree of Freedom
MDOF	Multiple Degrees of Freedom
RMS	Root Mean Square
MSDV	Motion Sickness Dose Value
VI	Vomiting Incidence
IR	Illness Rating

Introduction

1.1. The Submerged Floating Tunnel (SFT): a new concept for crossing waterways

Crossing waterways has always been one of the biggest challenges to be overcome by a civil engineer, being related to the necessity of expansion and development of the countries. In present days, it also relates to the increasing numbers of commuters who are willing for faster connections.

The risks and uncertainties recurring in the design of such infrastructures increase, as the distance to be covered increases. As technology evolves providing new construction materials, which are stronger and more durable, structural engineers pushed themselves in the design of long suspension bridges to cross deep-water straits or rivers. The longest single span bridge ever constructed is the Akashi Kaikyō Bridge in Japan. This bridge was constructed during the 90s and it is a stiffened truss suspension bridge with three spans and two hinges¹, whose main span measures 1991 m. Behind the design decision of the stiffened truss structure, there is the necessity of providing enough lateral and torsional stiffness to the deck to avoid instability phenomena. Such problem can be dealt with the implementation of a spatial cable system. Its beneficial effect can be observed in the application for the pipeline bridges ("Cable Supported Bridges: Concept and Design").



Figure 1.1: Akashi Kaikyō Bridge. Picture taken from Wikipedia, https://en.wikipedia.org/wiki/Akashi_Kaikyō_Bridge.

The use of long single-span suspension bridges is not just a matter of holding a record. In many cases a single-span is required since no intermediate pillars can be installed due to a very deep seabed. Adding pillars would cause execution problems due to environmental conditions. This is what happened when, by the end of the 60s, the project of the Messina Strait crossing moved from just concepts to technically possible and complete proposal. A worldwide competition was opened by the Italian Ministry of Public Works in 1969 and it attracted more than one hundred design proposals. The two that may be remarkable to highlight are a single span 3000 m suspension bridge proposed by the Gruppo Ponte Di Messina (GPM) and a road a rail floating tunnel anchored at the seabed proposed by the Grant JV.

¹"Akashi-Kaikyō Bridge". Honshu-Shikoku Bridge Expressway Company Limited. Retrieved 6 April 2009.

The SFT concept was first invented in Norway at the beginning of the XXth century, but the technology at that time didn't allow to build such offshore structures. Moreover, in the last decades several immersed tunnels have been built, providing a good understanding in dealing with a modular structure and the requirement of the waterproof joints. A SFT is a pipe-like structure which is laying at a predefined depth to allow vessels to navigate without interruption. It is stuck in its position by different anchorage system: cables, tension legs or piles, that have the anchorage at the seabed, or buoyant islands, that float over the tunnel length. The tunnel is subjected to two types of permanent loads: self-weight and buoyancy. In most researches, the tunnel cross-section has been designed such that the residual buoyancy is directed upwards. Depending on the depth of the seabed one can also prefer the tension legs over the cable since long cables' shape tend to modify into a parabola due to the increasing weight. Hence, the use of small tubes in the anchors can provide an extra buoyancy upwards force. The pretension in the anchors is driven by the amount of the residual buoyancy and these have also the function to reduce the deflections and stresses caused by the environmental loads.

The construction of the SFT seems to be still a challenge because no infrastructure of this type has been built yet. The lack of data on its actual behaviour makes engineers still sceptical of this technology even though it presents different advantages compared to the other waterway crossings. The construction of a full-scale prototype seems to be the breakthrough for the spread of this crossing solution.

1.2. Structural Features

1.2.1. Structural requirements

The design of the cross-section's geometry of the SFT has to comply with some requirements:

1. The internal diameter needs to be assumed in order to be able to accommodate the road or railway tracks, lateral maintenance corridors and ventilation systems for the fire safety.
2. The thickness of the concrete tube as well as additional internal separation walls must be designed so that the required structural performances (stiffness, strength, ductility) are met. This has to be valid for both serviceability and ultimate limit states. Moreover, the designer needs to pay particular attention to the durability and permeability of the concrete mix to ensure waterproofing of the tunnel.
3. The Buoyancy-to-Weight Ratio (BWR), which is the ratio between the upwards buoyancy force and the sum of the selfweight and live loads, needs to be larger than a lower bound, e.g. $BWR \geq 1.20$. Setting a lower bound of the residual buoyancy aims to guarantee that no slacking of the cables occurs in working condition. For the case of the buoyant island, where the SFT results to be heavier than displaced surrounding fluid, different criteria have to be fulfilled. Moreover, the magnitude of the external diameter of the cross section, which defines both downwards and upwards forces, results to influence the hydrodynamic actions too, being them proportional to the diameter.

In the first feasibility studies present in literature usually a too large lower bound of the BWR was considered, e.g. $BWR=1.70$, being the slackening of the anchorages a scenario to be avoided. A positive feedback was obtained thanks to numerical studies, which confirmed that larger values of the BWR could improve the structural performance of the SFT in case of severe environmental loading conditions. To corroborate this Brancaloni et al. [2] found that the increase of the BWR from 1.25 to 1.40 can lead to remarkable improvements of the SFT response to rough sea conditions.

Figure 1.2 shows through a flow chart the conceptual procedure applied for the design of the SFT's cross-section, as done also in Martire [28]. From the aforementioned design requisites, it is important to satisfy points 1 and 3 in early-design. Assumed the operative conditions for the chosen crossing, which depend on the type of infrastructure to be installed in the tunnel, i.e. motorway or railway and the fire exits, and once the construction materials and the shape of the cross-section are defined, a pre-design can be performed. From this step, some relevant information can be determined such as the upwards buoyancy force ($F_{buoyancy}$) and the self-weight (G_I). By setting a threshold for the minimum admissible value of the BWR, e.g. $\alpha = 1.20 - 1.40$, it is hence possible to compute the amount of ballast water (G_{II}), if required, in order to impose the condition:

$$BWR = \alpha \tag{1.1}$$

which will drive the minimum pre-tensioning force of the cables system minimising the permanent stresses in the tunnel, anchorages and foundations blocks.

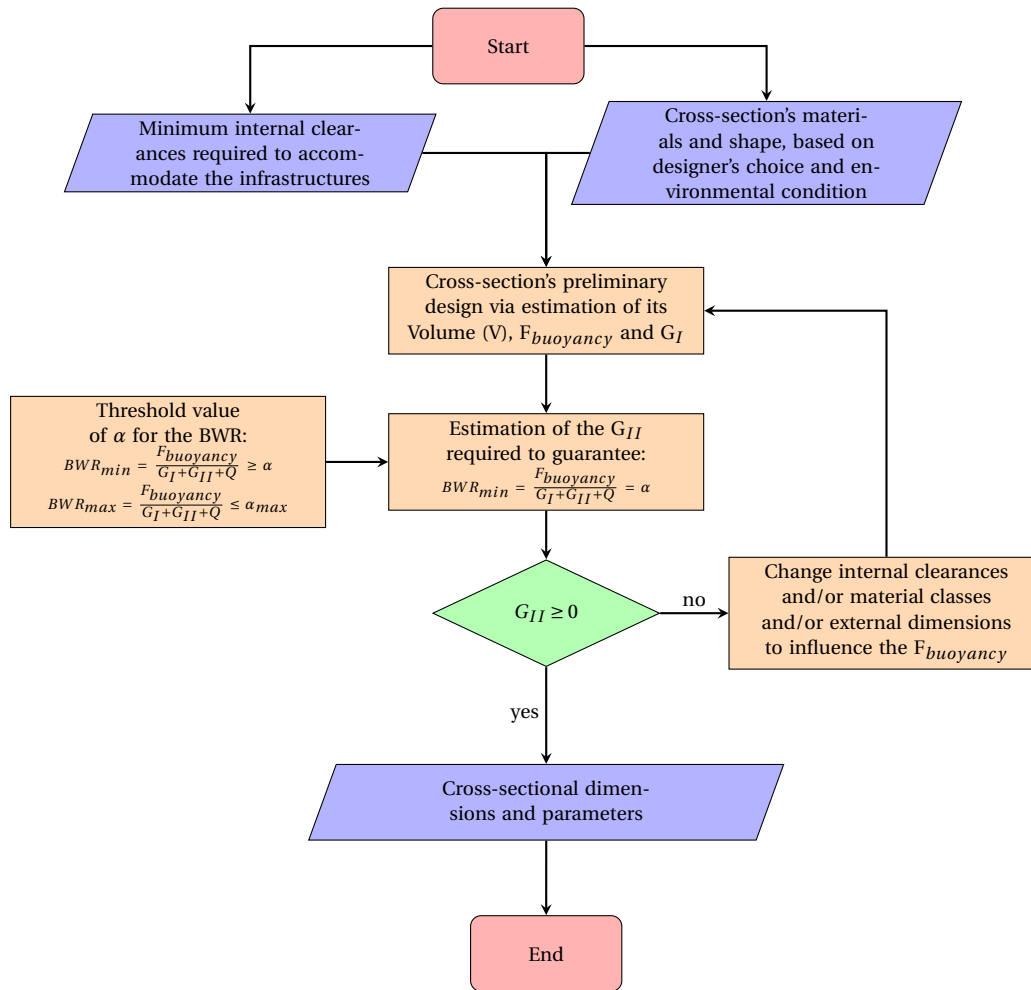


Figure 1.2: Flowchart of the preliminary design procedure, where G_I = structural load, G_{II} = ballast water, Q = live loads

Based on the assumed dimensions, if G_{II} results to be smaller than 0, it means the structure has a very limited upwards buoyancy force. Hence, it is necessary to iterate the design calculation applying one or a combination of the following:

- increase the buoyancy via the external dimensions;
- decrease the self-weight of the tunnel via reduction, where possible, of the dimensions of the internal clearances (i.e. thickness of the walls and floors);
- decrease the self-weight of the tunnel via the choice of lighter materials.

The iterative design procedure terminates once the combination of cross-sectional dimensions that satisfy the requirement of the minimum value of the BWR is found. Then, the amount of ballast water to be stored can be also quantified. To reduce the permanent stresses inside the structure, it would seem appropriate to set also an upper limit to the BWR, as it has been done for the design of the SFT Prototype in Qiandao Lake, China, whose cross-section arrangement was made in order to have a BWR in the range of 1.20 and 1.30, leading to an acceptable performance of the cable system subjected to the environmental loading of waves, currents or earthquakes Mazzolani et al. [30, 31]. However, the SFT prototype for Qiandao Lake crossing constitutes a particular case since it is a small pedestrian crossing. With more complicated inner arrangements of the cross-section, required to accommodate the infrastructures, safety corridors and all the other functional facilities, imposing an upper-bound for the BWR may request more iterations in the design process to obtain the best combination which also meet this last requirement. So, at the end of the design process showed in

Figure 1.2 it is additionally asked to check:

$$BWR_{max} \leq \alpha_{max}. \quad (1.2)$$

In case this condition is not fulfilled, it is necessary perform an additional iteration. A way to reach this goal is to increase the global dimension of the tunnel. This affects both the amount of upwards buoyancy force and the weight of the structure, giving the possibility to lay in between the two boundary values. This increase of the cross-section dimension may be quantified with a scaling factor (SF).

Being the case that at an iteration the resulting BWR was not meeting the limit imposed by (1.2), the updated ballast water and BWR may be evaluated as a function of SF:

$$G_{II} = \frac{F_{buoyancy} - \alpha(G_I + Q)}{\alpha} \quad (1.3)$$

$$RB = F_{buoyancy} - (G_I + G_{II}) = F_{buoyancy}(1 - \frac{1}{\alpha}) + Q \quad (1.4)$$

When scaling the dimensions the Residual Buoyancy (RB) varies according to:

$$RB_{new} = SF F_{buoyancy} - (SF G_I + G_{II}) = SF F_{buoyancy}(1 - \frac{1}{\alpha}) + Q \quad (1.5)$$

Thus, the ratio between the two values of residual upwards buoyancy force is:

$$\frac{RB_{new}}{RB} = \frac{SF F_{buoyancy}(1 - \frac{1}{\alpha}) + Q}{F_{buoyancy}(1 - \frac{1}{\alpha}) + Q} > 1 \quad (1.6)$$

which can be noted to be greater than one, meaning that respecting both limitation increases both the BWR and the permanent stresses on the tunnel.

1.2.2. Construction materials

The choice of a construction material is driven by diverse criteria, such as the structural performances of the tunnel, the resistance to the environmental condition and the construction methods and costs. Regarding the resistance and duration of the structure it may be applied to main techniques, a composite structure with a outer steel sheet to increment the corrosion resistance of the internal reinforced concrete structure. The steel sheet need to be protected with special paintings to resist the chemical attack of chlorides present in the seawater. Such system may be implemented when regular cross-section shape is applied for the tunnel, i.e. circular cross-section, when the steel sheeting can be prefabricated with the requested diameter and thickness. When the designer opts for articulated shapes, i.e. polygonal shape, the composite structure may be substituted by ultra-durable concrete mixtures, i.e. alkali activated cementitious concrete, or by the new generation of self-healing concrete². From the economic point of view it has been shown that the cost increment as a function of the crossing length follows a linear trend, Figure 1.3 Minoretta [33], and it appears to be cost competitive with suspension bridges, especially when long distances need to be covered.

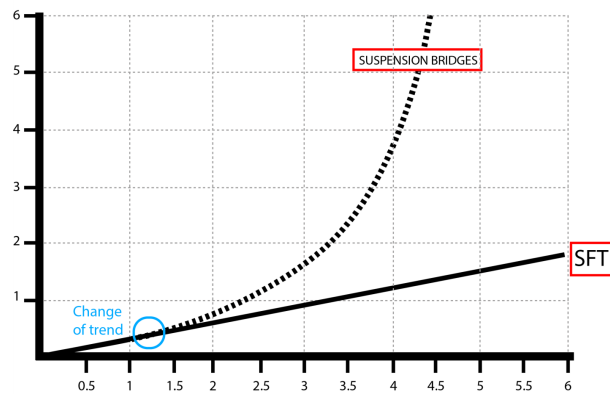


Figure 1.3: Cost Comparison Suspension Bridge and SFT, where the length of the crossing (km) is shown on the abscissa and the costs are on the ordinate

²Jonkers, H. M., Thijssen, A., Muyzer, G., Copuroglu, O., Schlangen, E. (2010). Application of bacteria as self-healing agent for the development of sustainable concrete. Ecological Engineering, Vol. 36, pp. 230-235.

The materials that appear to fulfil the requirements for the construction of the tunnel prefabricated sections of a SFT are:

- Steel;
- Reinforced Concrete;
- Prestressed Concrete, for joint waterproofing;
- Rubber foam, for corrosion protection.

The knowledge acquired in the offshore engineering and immersed tunnels guides to the choice of ordinary steel and concrete grades. However, to face the limited fatigue resistance of welded connection new steel types may be used, such the so called Fatigue Crack Arrestor (FCA)³. On the other side, concrete is well liked when large weight is required to stabilise the structure. In the SFT application downwards force due to self-weight is vital to control the stresses due to upwards buoyancy. It can also be highlighted the fire resistance of concrete, making it preferable as internal construction material compared to steel. During building face it seems reasonable to apply precompression the tunnel segments, increasing the structural performances and tensile strength of the tunnel and the degree of waterproofing.

1.2.3. SFT module configuration

The modules configuration can be categorised according to their geometrical shape, mainly referring to the outer shape, being that of relevance when evaluating the cross-sectional properties and the Fluid-Structure Interaction (FSI). The cross-section shape of a SFT can be as listed here below:

- circular, Figure 1.4;
- polygonal, elongated in the horizontal direction, Figure 1.5;
- circular tubes connected by a truss structure, Figure 1.6.

Circular cross-sections have been considered during the feasibility studies of the Messina Strait (Figure 1.4a; Bruschi et al. [3]), the Funka Bay's (Figure 1.4b; Kanie [19]) and the Qiandao Lake (Figure 1.4c; Mazzolani et al. [32]) crossings. It may be worth noting that a circular cross-section features translational movements due to wave loading, while rotational force components remain negligible (Brancaleoni et al. [2]). However, such shape results in more complex construction details and installation procedures when compared with rectangular shapes (Grantz [15]).

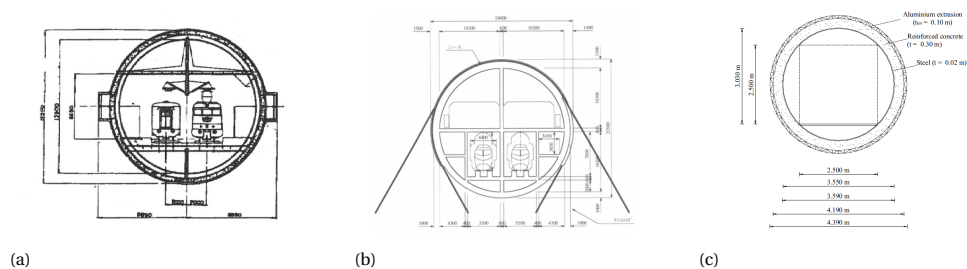


Figure 1.4: SFT having circular cross-section. (a) Strait of Messina crossing as proposed by ENI, IRI, IMI (Bruschi et al. [3]). (b) Funka Bay crossing as proposed by the society of SFT research in Hokkaido (Kanie [19]). (c) Qiandao Lake crossing as proposed by Mazzolani et al. [32]

Cross-sectional shapes featuring more mass placed in the flow direction are suitable for the cases when current velocities are driving the environmental loading. For this purpose elliptical or polygonal modules are developed and among the proposals it is worth mentioning the Jintang Strait crossing (Figure 1.5a; Lee [24]). Such proposed shape, however, might be complicated to fabricate and to overcome this problem it may be adopted a rectangular cross-section with aerodynamic streamlined inserts, as it is already applied in bridges such as the Great Belt East crossing (Figure 1.5b; Andersen et al, 2016⁴)

³Kazasidis M., 2018. Investigation of metal cored arc welded FCA (Fatigue Crack Arrestor) steel in terms of microstructure, toughness and tensile properties. PhD Thesis. National Technical University of Athens.

⁴Andersen, J. E., Farreras-Alcover, I., Chryssanthopoulos, M. K. (2016). Data-based models for fatigue reliability of orthotropic steel bridge decks based on temperature, traffic and strain monitoring. International Journal of Fatigue, Vol. 95, pp. 104-119.

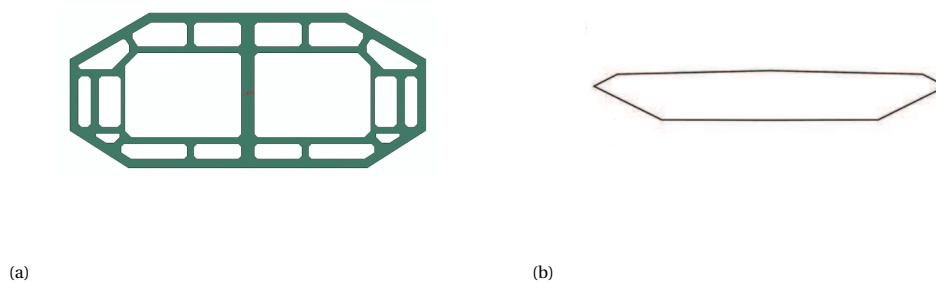


Figure 1.5: SFT having polygonal cross-section. (a) Strait of Jintang crossing (Lee et al, 2018). (b) Great Belt East bridge as proposed by Dissing+Weitling (Andersen et al, 2016)

Another possibility for the modules is the use of more circular tubes connected together via a truss structure to provide more stiffness to the global system in the flow direction. Such approach have been adopted by the Norwegian Public Roads Administration in the recent feasibility studies for their big project of the E39 Coastal Highway Route ⁵. It is worth mentioning the Bjørnafjord (Figure 1.6a; Søreide and Haugerud [38]) and the Sognefjord (Figure 1.6b; Fjeld et al. [12]) crossings.

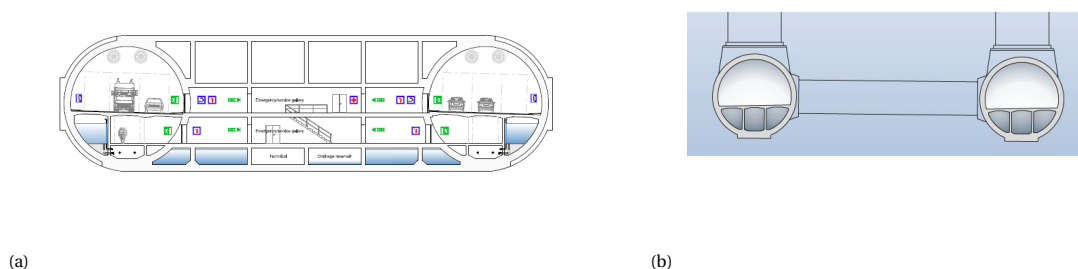


Figure 1.6: SFT having circular cross-section and connected with truss. (a) Bjørnafjord crossing as proposed by Statens Vegvesen (Søreide and Haugerud [38]). (b) Sognefjord crossing as proposed by Statens Vegvesen (Fjeld et al. [12])

1.2.4. Anchoring System

The most versatile material that can be used to design all different type of anchoring systems is steel. It is used in the offshore engineering application as it can be used for mooring cables design as well as for tension legs or tethers. In the last decades Fibre Reinforced Polymers (FRP) have made their appearance in the offshore engineering thanks to the excellent strength-to-weight-ratio and higher stiffness compared to steel. The most used fibres are Aramid or Carbon. However, FRPs feature an elastic behaviour up to failure and a relative small hardening branch (Kolstein [20]). Another suitable material is concrete, which becomes the main design material when designing with buoyant caissons.

The anchoring system is responsible for the counteraction to the residual forces acting on the tunnel and for the restraint of the displacements of the structure when environmental forces are acting on it. The Residual Forces (RF) can be of two species and they depend on the designer choice: the upwards RB, or the downwards Residual Weight (RW). In case the RF are equal to zero, the environmental conditions are favourable and the length of the crossing is relatively small, the designer may opt for a self-bearing crossing Figure 1.7.d to limit the stresses inside the structure. If the RF are in the buoyancy direction, the anchoring system requires to be made of tension members, which can be cable or tethers Figure 1.7.a. Lastly, when the RF are in the weight direction, the choice of the anchoring system may be driven by the depth of the seabed. Hence, the two alternatives are the column support Figure 1.7.c or the floating pontoons Figure 1.7.b.

⁵<https://www.vegvesen.no/en/roads/Roads+and+bridges/Road+projects/e39coastalhighwayroute>

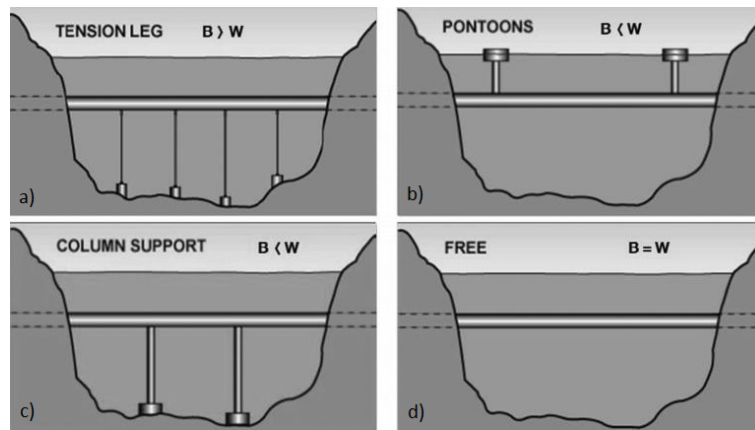
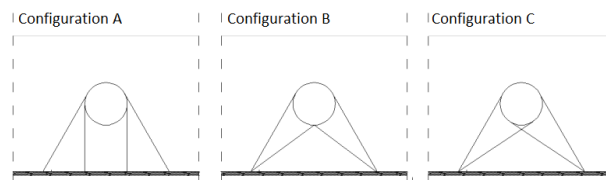


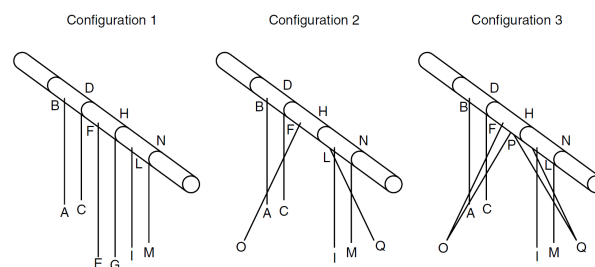
Figure 1.7: Supporting system SFT. Figure taken from (Kwark et al. [22])

The tunnel configuration with tension members may be the best choice when it is required to restrain possible high horizontal displacements due to harsh sea-states. This is thanks to the possibility of arrange the stabilising cables not only in the vertical direction. These can also be placed under an angle with respect to the vertical axis in order to provide the required horizontal supporting stiffness.

Hence, the geometrical configuration as well as the diameter of the cables is vital to quantify the stiffness of the supports. Generally, the adopted configuration is repeated at a prescribed inter-axis to provide a uniform stiffness. Different cables arrangement have been studied, Figure 1.8, to understand their influence on the dynamic response of the tunnel (Mazzolani et al. [31]). A cable setup based on inclined cables appears to be particularly efficient when earthquake loading is studied (Wahyuni et al. [41]). A supporting system based on vertical cables exclusively, Figure 1.8b, seems to be valid when the structure experience calm sea states, since numerical models predict limited horizontal stiffness, (Mazzolani et al. [31]). The alternation of groups composed of four inclined cables and a couple of vertical cables, Figure 1.8b, is the most effective arrangement, as it provides good stiffness to support the tunnel vertically, horizontally and torsionally, (Martire [28]).



(a)



(b)

Figure 1.8: (a) Configurations of SFT. Figure taken from (Wahyuni et al. [41]). (b) Configurations of SFT. Figure taken from (Mazzolani et al. [31])

As mentioned before, the horizontal deflection that the structure experiences under environmental loads, i.e. sea currents and waves, is important to be controlled to limit stresses and acceleration in the structure within acceptable boundaries. The Statens Vegvesen (Søreide and Haugerud [38]) in their feasibility study

for the Bjørnafjorden Crossing proposed a maximum allowed deflection and acceleration in the structure, Table 1.1

	Total Deflection	Acceleration
	(m)	(m/s ²)
Horizontal	$\frac{L}{200}$	0.3
Vertical	$\frac{L}{350}$	0.5

Table 1.1: Limiting Deflection and Acceleration

where L coincides with the cable interaxis.

Moreover, it is important to avoid slackening. This phenomenon may happen when all static loads contributes to minimise the tension in the tether and the dynamic effect of wave loading drives the slack, see ultimate limit state combination EQU in Figure 1.9. Søreide and Haugerud [38] reported that when happening, the time when the cable experience negative tension is short and hence, it is not critical.

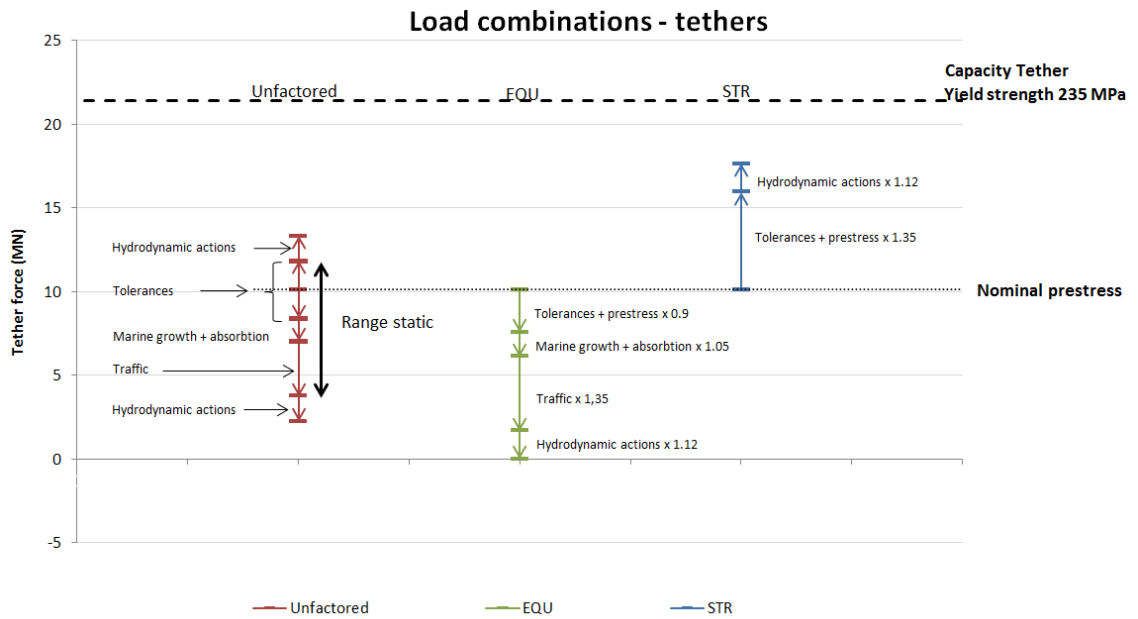


Figure 1.9: Configurations of SFT. Figure taken from Søreide and Haugerud [38]. Three load combinations are shown in which all loading sources are summed to identify possible slack in the tethers.

1.3. Traffic Load

The traffic load depends on the final use of the SFT, which may be railway, roadway or pedestrian crossings or combination of these. Usually standards, e.g. Eurocode 1, part 3, 1991, provide generalised loading conditions based on statistical data, since traffic has variation of its intensity within a day; these loading schemes aims to replicate the highest stress conditions produced on the structure. However, few researches are available in literature on the effect of moving loads, e.g. trains, on the global dynamic response of the SFT.

Tariverdilo et al. [40] studied the vibration of a SFT due to moving loads with two and three dimensional added masses and investigated the impact of vehicle's velocity and stiffness of the supporting cable system. The moving load has a velocity of 90m/s and it is considered as point force and the equally-spaced cables are simplified by continuous elastic foundation. The results indicate that the difference in the response of the 2D and 3D added masses models decreases as the cable system is stiffer. Hence, they concluded that in this case Morison's expression will yield reasonable results when studying the FSI.

Yuan et al. [44] investigated the influence of the speed of a single moving load on the dynamic response of the SFT. The SFT tube is simplified as an elastically supported beam with two springs and dashpots at each

end and the FSI is studied using the Morison's formula for the case of a steady-still fluid. They concluded that the dynamic response can be controlled by adjusting the vertical stiffness of cable system.

Jin and Kim [17] analysed the dynamic response of the SFT under moving loads and wave excitation. The tunnel is modelled with fixed supports at both ends and the analyses are divided in two steps. A first analysis in still-water is made to evaluate the impact of the BWR and vehicle's velocity, while the second analysis focused on the structural global response under both wave and moving loads.

Kwark et al. [22] in their study developed an algorithm for the dynamic FSVI. The tunnel is modelled with commercial Finite Element Method (FEM) software ABAQUS for the case when the BWR is greater than one and the vehicle used in the analyses is a Korean KTX high speed train. The FSI has been modelled through the concept of the added mass and the dynamic interaction analyses are conducted with superposition method when the KTX is moving along the submerged floating tunnel. The results revealed that the maximum vertical and lateral displacements occur at the midpoint between the two cables for the central section of the SFT.

Jiang and Liang [16] studied the main influence factors of traffic loads in the dynamic response of the SFT. Starting from the characteristics of the moving vehicles and the structural parameters of SFT, they proposed a calculation formula of traffic loads, which takes into account the several influencing factors. The orthogonal experiment method and the analytic hierarchy process are combined with FEM models to quantify the weight of each factor. They concluded that the weights of the influence factors vary with the choice of the judge index: road roughness and vehicle's speed have the highest weights if the maximum value of traffic loads is the judge index, whereas wave height and wheels' static loads if the maximum mid-span vertical displacement is the judge index.

1.4. Problem Definition

There are not so many researches into the traffic loading analysis regarding the SFT and none of these focus on the dynamic interaction between all parts of the system, i.e. the structure the vehicle and the water. The focus of the current thesis will be on the comfort analysis investigating the serviceability limit state of the structure and the following ride quality under specific storm scenarios. The local environmental conditions and the design of the tunnel are also important for the global response of the structure, as the location defines the forces and the cross-section dimensions define the stiffness of the tunnel. The structural stiffness has to be tuned carefully to let the frequency range characterising the local storm not fell within the range of the structural natural frequencies. Moreover, it has to provide enough stiffness to limit the deflections, which determine whether the tunnel can be traversed by the train, and the accelerations, which control the ride comfort in the train car while crossing the tunnel.

1.5. Scope

The background information available in literature and the problem definition have led to the following research scope: "The study of the degree of importance of the supporting configuration, the sea states, the suspension characteristics and the rail defect for the definition of the ride quality and comfort. The aim of this study is to asses the ride comfort and serviceability of the structure for specific environmental conditions of a SFT."

From this research objective, a main research question with some subquestions were formulated.

Main question

"Is it safe and comfortable to cross the tunnel under storm conditions?"

Subquestions

- Which load case is the most critical?
- Which system parameter affects most the ride comfort?
- Is the unevenness of the rail critical to the comfort assessment?

The project will investigate the magnitude of the tunnel's vibrations and displacements induced by the passing train. The impact of the various tunnel, cable and train parameters will be examined to provide for each a range that can be used for a future design of the tunnel.

1.6. Approach

The aim of this research, as mentioned above in section 1.5, is to describe how to address the comfort assessment of a train running inside a SFT under storm sea state. A general literature overview has been offered in

the previous sections to obtain a better understanding of this new crossing solution for tunnel engineering. A research topic has been selected from this study: the ride comfort assessment.

In chapter 2 the loads acting on the structure are identified and described. Particular emphasis is given to the environmental load cases, which are also the ones driving the structural integrity.

In chapter 3 it is described the definition of comfort and the criteria commonly used to evaluate it. Here, the attention is paid to the range of frequencies that regards to the so called whole-body vibrations, $0.5Hz < f < 80Hz$.

The solution methods used to compute the time-histories of the displacement and acceleration of the bending vibration and the train car masses are addressed in chapter 4. Different models are implemented depending on the scope of the simulation and in order to reduce the computational time required.

All the parameters that are implemented and varied during the course of the simulations are identified in chapter 5. Starting with the cross-section dimensions, whose minimum requirement is the accommodation of two railway tracks, then the configuration of the supporting system is addressed followed by the structural modal analysis which allows to approximate the natural frequencies which are helpful when discussing the global dynamic response. Last sections are, instead, dedicated to the load parameters, i.e. wave and vehicle characteristics.

The results of the simulations are presented in chapter 6 where they are divided in sections and each of these refer to a specific scope. The discussion and analysis of the results is separately treated in chapter 7 and a final overview on the obtained results with attention to the research questions is provided in chapter 8.

1.7. Assumptions

To obtain a solution for the problem, some simplification, valid for both the static and dynamic analysis, are applied.

- One train running inside the tunnel
- Constant velocity of the train
- Seabed is constant along the tunnel length
- Hinged boundary conditions
- Linear elastic constitutive relation for the cables
- Length of the crossing limited to $1km$ to avoid long computational time

2

Structural Loads

2.1. Introduction

This chapter summarises all relevant load cases acting on the SFT after construction. For the static analysis of the structure, all permanent structural and non-structural loads are considered. Among these loads there are self-weight of the structure, structural elements for the infrastructure and services, buoyancy etc. The exceptions are traffic loads, which are time dependent and hence, are playing a role for the dynamic response of the structure.

In the table below is proposed a list of the main loads acting on the structure according to the EN 1990 classification:

Load Classification	Load Description
G	Structural Weight
G	Non-structural Weight
G	Buoyancy
Q	Weight
Q	Current
Q	Wave
Q	Traffic

Table 2.1: Load Classification

The experience gained with the Immersed Tunnels gives the designer the advice to not forget the influence of hydrostatic pressure. It takes part in the buoyancy of the SFT and it generates stresses around the cross-section, which increase with the depth at which the tunnel is placed. The distribution, and so the increase, of the hydrostatic pressure depends on the density variation of the water.

2.2. Permanent Load

As shown in Table 2.1 the permanent loads comprise three classes, the structural weight, the non-structural weight and the buoyancy. To these it must be added the variable weight, which consists of the marine growth which concentrates at the seabed and at the sea surface. The effect of it will be secondary/minor being it located at an intermediate depth.

The two contributions to the total weight can be evaluated as: the selfweight of the tunnel and the additional structural loads.

$$G = G_1 + G_{2,1}. \quad (2.1)$$

The selfweight, as a function of the wall's thickness t_{wall} can be evaluated by the expression below.

$$G_1 = \rho g \pi \frac{D_{external}^2 - D_{internal}^2}{4}. \quad (2.2)$$

where $D_{external} = D_{internal} + 2 t_{wall}$.

The non-structural permanent loads are assumed to be in total $100 \frac{kN}{m}$, being them divided into:

$$G_{2,1} = q_{rail} + q_{services}. \quad (2.3)$$

Archimedes' principle states that the upward buoyant force acting on a body immersed in a fluid, is equal to the weight of the displaced fluid. Hence, the buoyancy force acting on the tunnel can be evaluated as show in expression below.

$$G_{2,2} = \rho_w g \pi \frac{D_{external}^2}{4}. \quad (2.4)$$

2.3. Variable/Functional Load

One class of the variable loads are the functional loads. These vary together with the infrastructure that is thought to be accommodated in the tunnel's cross-section, such as roadway, railway, cycling path and/or pedestrian lanes. Standards, e.g. EN 1991-3, often use statistical data to assess the most unfavourable loading condition on the structure

2.4. Environmental Load

Under the class of environmental loads, there are the change in the tide levels, waves and currents. The last two often represent the most important and dangerous environmental actions for a SFT. For this reason it seems important to study the water-structure interaction.

2.4.1. Tide

The tide effect on the SFT is based on the change of the buoyant forces as well as the hydrostatic pressure on the tunnel's cross-section, which will increase or decrease due to the change in water levels. So, this movement can be seen as a vertical current acting on the structure

2.4.2. Current

With current, generally, it is meant the wind generated currents, which are generated via the transportation of the energy from the wind to the sea surface. The movement in the water particles generated by this type of current is mainly in the direction of the wind force, e.g. horizontal direction. The magnitude is assumed to be constant with respect to time, being the changes really small, e.g. quasi-static.

When designing, it is required to collect the data from prescribed depth to model the velocity profile, or analytical expressions are available in literature, see Martire [28]:

$$V_c(z) = V_0 \left(\frac{z+d}{d} \right). \quad (2.5)$$

where V_0 is the wind-induced current velocity at sea surface level.

2.4.3. Wave

The kinematic of the water particles under wave condition is an oscillatory motion. Waves are started by two sources:

- wind-driven waves, or surface waves, are created by the friction between wind and surface water. As wind blows across the surface of the ocean or a lake, the continual disturbance creates a wave crest. These types of waves are found globally across the open ocean and along the coast¹;
- ocean internal waves are waves in the interior of the ocean which are generated when the interface between layers of different water densities, temperature, salinity is disturbed, usually caused by tidal flow over shallow bathymetry².

¹NOAA. Why does the ocean have waves? National Ocean Service website, <https://oceanservice.noaa.gov/facts/wavesinocean.html>, 25/06/18.

²Alpers, W. (2014). Ocean Internal Waves. Encyclopedia of Remote Sensing, pages 433-437.

There are several theories which describes the wave profile, but they are all approximations of the real phenomenon. All these have in common the search of a velocity potential that satisfies the Laplace Equation under the assumption of incompressible fluid. There can be distinguished the Linear, Non-linear and Other wave theories. A widely used wave theory is the Airy wave theory, see Krogstad and Arntsen [21], commonly referred to as linear or first order wave theory because of the simplifying assumptions. This theory is applicable when the wave height is small compared to the wavelength and the water depth. In particular, basic assumptions are:

- homogeneous and incompressible fluid;
- wavelength bigger than 3m, so that allows to neglect capillary waves;
- irrotational flow, so no shear forces are present.

Under this assumption the fluid potential Φ must satisfy the Laplace Equation. By applying the boundary conditions of impermeability at the seabed and constant pressure at the sea surface, it can be derived the general expression for the sea surface elevation:

$$\eta(x, t) = a \cos(kx - \omega t). \quad (2.6)$$

where

$$\begin{aligned} a[m] & \text{ is the wave amplitude} \\ k = \frac{2\pi}{\lambda} [\frac{rad}{m}] & \text{ is the angular wavenumber} \\ \omega = \frac{2\pi}{T} = 2\pi f [\frac{rad}{s}] & \text{ is the angular frequency} \end{aligned}$$

Non-linear waves are characterised by larger amplitude, sharper crests and flatter and larger troughs compared to the sinusoidal wave. The most adopted non-linear wave theory is the Stokes waves theory, which finds its start point in the Taylor expansion around the mean water elevation of the potential flow, the so-called perturbation procedure. When using a lower order of the perturbation expansion, e.g. second to fifth order, Stokes' wave theory gives accurate results when the wave steepness is moderate and water depth is from intermediate to deep. Hence, the wave height-to-wavelength ratio needs to be well under one, $\frac{H_w}{\lambda} \ll 1$ and the wavelength less than eight times the water depth, $\lambda < 8.15 d$ Laitone [23].

To obtain the accuracy in the results in case of shallow waters, the theory to be used is the Cnoidal wave theory. As shown in Figure 2.1, the wave profile that can be described is characterised by steep crests and flat troughs. Through this theory is also possible to describe the limit case of the Solitary wave, which has an infinite wavelength³.

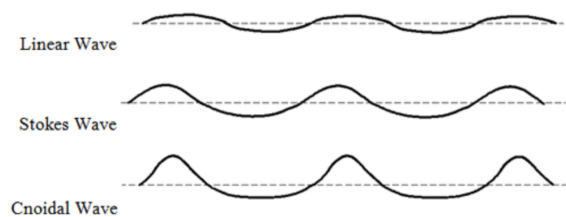


Figure 2.1: Wave profile for different theories. Figure taken from³.

However, in actual sea states the water surface appears to be irregular and hence, it can be described as a superposition of an infinite number of regular sinusoidal waves. An analytical expression to evaluate the sea surface elevation η_w for an unidirectional sea state can be formulated as done in Martire [28]:

$$\eta_w(x, t) = \int_0^\infty \frac{dH_w(\omega)}{2} \cos(kx - \omega t + \epsilon) d\omega \quad (2.7)$$

where

³Waves, <https://www.flow3d.com/modeling-capabilities/waves/>

$\omega = \frac{2\pi}{T_w} [\frac{rad}{s}]$	is the angular frequency of the regular wave
$k = \frac{2\pi}{\lambda_w} [\frac{rad}{m}]$	is the angular wavenumber related to the wave period T_w through the dispersion relation
$dH_w [m]$	is the regular wave height
ϵ	is the phase which is generally assumed to be a random variable uniformly distributed in $[0, 2\pi]$

The water surface elevation is often assumed to be an ergodic Gaussian random process, which is characterised by the stationarity of its mean value and variance. The ergodicity property allows to define the sea state via the temporal recording, when this is sufficiently long. The power spectral density $S_\eta(\omega)$ can be defined and it describes the irregular sea state. Several models of energy spectrum, which illustrates unidirectional waves conditions, can be found in literature. Among these, the most commonly used are the Pierson-Moskowitz and JONSWAP Spectra and the analytical formulations can be found in DNV [7]. The Pierson-Moskowitz spectrum $S_{PM}(\omega)$ is given by:

$$S_{PM}(\omega) = \frac{5}{16} H_S^2 \omega_p^4 \omega^{-5} \exp\left(-\frac{5}{4} \left(\frac{\omega}{\omega_p}\right)^{-4}\right) \quad (2.8)$$

where $\omega_p = \frac{2\pi}{T_p}$ is the angular spectral peak frequency.

The JONSWAP spectrum $S_J(\omega)$ is formulated as:

$$S_J(\omega) = A_\gamma S_{PM}(\omega) \gamma^{\exp\left(-0.5\left(\frac{\omega-\omega_p}{\sigma\omega_p}\right)^2\right)} \quad (2.9)$$

where

$A_\gamma = 1 - 0.287 \ln(\gamma)$	is a normalizing factor
$S_{PM}(\omega)$	is the Pierson-Moskowitz spectrum
ω_p	is the angular spectral peak frequency
γ	non-dimensional peak shape parameter, generally fixed to 3.3
σ	spectral width parameter
	$\sigma = \sigma_a = 0.07$ for $\omega \leq \omega_p$
	$\sigma = \sigma_b = 0.09$ for $\omega > \omega_p$

2.4.4. Hydrodynamic Forces

When computing the forces acting on the structure, one has to take into account the relative motion between the fluid and the structure. The most widely used expression to describe the fluid-structure interaction, in hydraulic and offshore engineering applications, is by means of the Morison's formula. For flexible structure the Morison's equation is in the form:

$$\vec{F} = \rho_w \frac{\pi D^2}{4} \left[(C_I - C_M) (\vec{V} - \ddot{w}(x, t)) + C_M \vec{V} \right] + \frac{1}{2} \rho_w C_D D (\vec{V} - \dot{w}(x, t)) |\vec{V} - \dot{w}(x, t)| \quad (2.10)$$

where

ρ_w	is the water density
D_{ext}	is the external diameter of the analysed structure, i.e. tunnel or cable
C_I, C_M, C_D	are the inertia, added mass and drag coefficient respectively
$\vec{V}, \ddot{w}(x, t)$	are the fluid and structure accelerations respectively
$V, \dot{w}(x, t)$	are the fluid and structure velocities respectively

The expression is composed by three addends, of which the first one is commonly referred to as the added mass produced by the presence of the structure in the cross-flow and it is an extra force needed to accelerate a body immersed in a fluid.

The second addend is the so called Froude-Krylov force, a force generated by the undisturbed waves. For a cylinder $C_I = 1 + C_M$, where C_M is the added mass coefficient which depends on the geometry of the cylinder. For a circular cylinder, $C_M = 1.0$ and hence, $C_I = 2.0^4$.

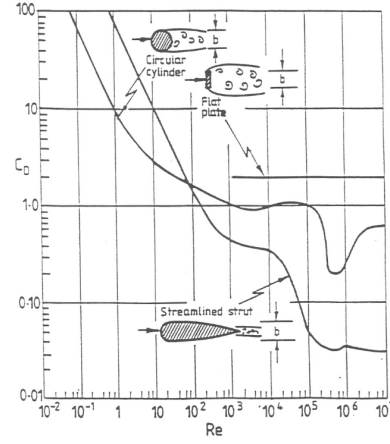
The last addend of the Morison's formula is the drag force, which arises due to the difference in pressure between upstream and downstream. It is important to study the flow characteristic and the possible turbulence to determine the pressure distribution at the contact between fluid and structure. The factor that

⁴E. Konstantinidis, A. Dedes, D. Bouris, (2012). Drag and inertia coefficients for a circular cylinder in a steady plus low-amplitude oscillatory flow.

drives the flow characterisation is the Reynolds number (Re), which is defined as the ratio between the product of the fluid velocity V and the structure dimension D . Sarpkaya, (Sarpkaya and Isaacson [35]), proposed a four main classes into which divide the flow, based on several laboratory test on cylinders in cross-flows, Figure 2.2.

	A	B	C	D
	Subcritical	Critical	Supercritical	Post-Supercritical
Boundary Layer	Laminar	Transition	Turbulent	Turbulent
Separation	About 82 deg	Transition	120 + 130 deg	About 120 deg
Shear Layer near separation	Laminar		Laminar Separation, Bubble	Turbulent
Strouhal Number	$S=0.212-2.7/Re$	Transition	$0.35 + 0.45$	About 0.29
Wake	$Re < 60$ Laminar $60 < Re < 5000$ Vortex Street $Re > 5000$ Turbulent	Not Periodic		
Approximate Re range	$< 2 \times 10^5$	$2 \times 10^5 \div 5 \times 10^5$	$5 \times 10^5 \div 3 \times 10^6$	$> 3 \times 10^6$

(a)



(b)

Figure 2.2: (a) Incompressible flow regimes and their consequences. Figure taken from (Sarpkaya and Isaacson [35], pag. 50). (b) Drag coefficient function of the Re .

Other studies have pointed out that both C_D and C_I not only depend on the Re , as shown in Figure 2.2b, but also on the Keulegan-Carpenter number (KC), defined as $KC = \frac{V_{max} T_w}{D}$, on the ratio between the roughness and the diameter D and on the time. However, the author continues that the time dependence has to be assigned completely to the force formulation, because it is not possible to derive a time-dependent formulation for the coefficients not even for a very regular flow. The aforementioned KC is a direct parameter for the categorisation of the forcing regime acting on the submerged structure, hence, the relative importance of drag and inertia forces. To distinguish these regimes one may work out the ratio of the amplitudes of the drag and inertia forces, neglecting also the $\frac{\pi}{2}$ phase shift between the force components, as presented in Journée and Massie [18].

$$\begin{aligned} \frac{F_{drag}}{F_{inertia}} &= \frac{\frac{1}{2} \rho C_D D V |V|}{\frac{\pi D^2}{4} \rho C_M \omega V} \\ &= \frac{2 C_D |V|}{\pi C_M D \omega}. \end{aligned} \quad (2.11)$$

The expression can be manipulated a bit more, noting that the wave-frequency can be expressed as a function of the wave-period $\omega = \frac{2\pi}{T}$

$$\begin{aligned} \frac{F_{drag}}{F_{inertia}} &= \frac{1}{\pi^2} \frac{C_D}{C_M} \frac{V T}{D} \\ &= \frac{1}{\pi^2} \frac{C_D}{C_M} KC \end{aligned} \quad (2.12)$$

Based on the expression in Equation 2.9 there have been proposed ranges of the KC which differentiate the force regimes:

- For low values of KC , e.g. $KC < 3$, the inertia force is dominant, the potential flow theory is applicable and the drag can be neglected.
- For KC ranging between $3 < KC < 15$, one may linearise the drag.
- For KC ranging between $15 < KC < 45$, one may not avoid using the full Morison equation with the nonlinear drag.

- For higher values of KC , e.g. $KC > 45$, the drag force is dominant, the vortex shedding frequency becomes bigger than the wave frequency hence the flow tends to a uniform flow and inertia can be neglected.

Making use of the aforementioned linear wave theory, it is possible to determine a linear dependence of the KC on the wave height H_w and tunnel diameter D . From Figure 2.3 it can be noticed that for value of the ratio between wave-height and tunnel diameter smaller than around 10, mass forces, i.e. inertia forces, are more relevant.

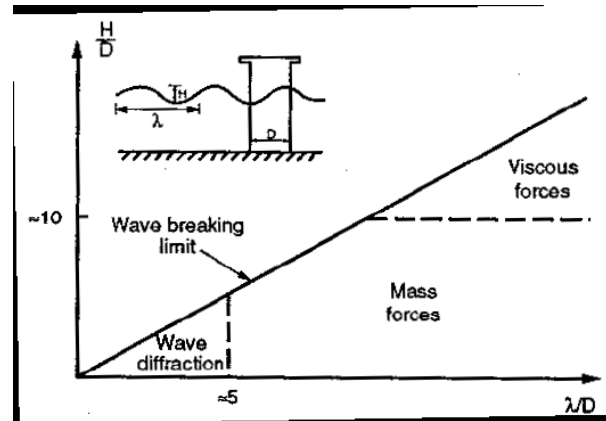


Figure 2.3: Wave loading regimes. Figure taken from (FEHRL [11]).

The environmental conditions allows the use of the Morison expression for the external forces assuming that the flow does not change the wave attack direction. This assumption results to be applicable for value of the ratio between the wave-length and the tunnel diameter smaller than 0.2 (DNV [7], MacCamy and Fuchs [27]). The SFT is in most of the cases a slender structure, being the ratio between its main cross-section dimension and its length commonly small. However, when looking at serviceability limit state or fatigue, hence, the wavelength of sea waves is small, e.g. 50-100 m, the ratio $\frac{D}{L_w}$ may exceed 0.2. This means that the FSI can not be studied with the Morison equation, but the diffraction theory needs to be applied. The account of waves diffraction makes the problem more difficult but it has a favourable aspect as the load applied by the waves on the structure is reduced.

2.4.5. Accidental Load

Among these, one has to mention:

- Earthquakes;
- Tsunami;
- Collision with submarines;
- Internal explosion.

Extensive literature is available regarding seismic loads. (Brancaleoni et al. [2]) analysed and discussed different tunnel type under the seismic and wave excitation. (Martire [28]) investigated the seismic behaviour of the Messina Strait Crossing SFT for different cable system configuration, concluding that the SFT solution presents great potential when large spans needs to be crossed. The same authors studied also the propagation of vertical ground motion, created by fault breaking, in the upper water. It has been observed that the water and ground move synchronously in the central part of the crossing, while a phase shifted can be noticed to happen close to the shores (Martire et al. [29]). (Su and Sun [39]) focused on the study of the seismic behaviour of the tether support when also parametric excitation is involved. They concluded that when parametric resonance is met, the tether's transient maximum midspan displacement may be influenced by the topology of the seismic wave while the steady-state displacement is kept constant to a precise value.

The tsunami loading scenario has been addressed in (Perotti et al. [34]) noting that the propagation of a tsunami wave through a sea strait may involve important amplifications of the forces acting on the SFT.

The event of a collision with submarines has been treated in (Søreide and Haugerud [38]), where it has been proposed a detailed analysis of this load case with the control of the critical sections for bending moments and punching shear, concluding that the most critical scenario is when the structure is hit eccentrically, Figure 2.4.

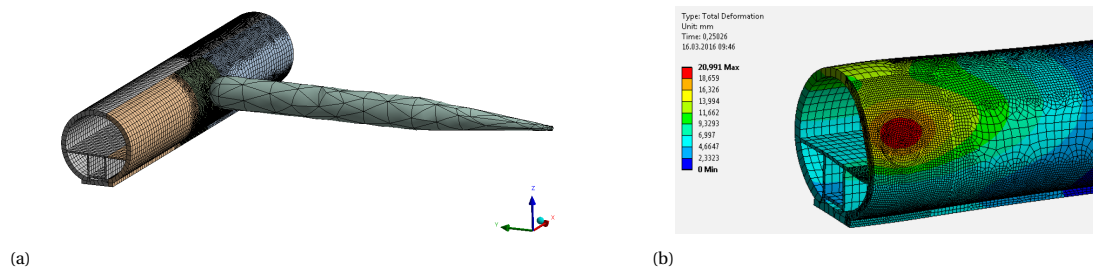


Figure 2.4: (a) FEM model of SFT collision with a submarine. (b) Configurations of SFT. Figures taken from (Søreide and Haugerud [38])

Lastly, the study of an internal explosion matters in case of an evacuation for a better planning of escape routes.

3

Ride Comfort

3.1. Introduction

This chapter summarises the definition of ride comfort and ride quality and presents the evaluation standards for the railway applications.

Comfort is generally defined as a subjective situation in which one is relaxed and does not have any physically unpleasant feelings ¹. In infrastructure and transportation applications there are several terms associated with the sense of well-being: passenger comfort, ride quality, ride comfort, ride index. The sections below will shortly describe the difference within these terms.

3.2. Ride Quality

Ride quality differs from individual to individual, being it dependent on a person's physical conditions in the vehicle environment, under different variables. Among these one has to mention the dynamic variables, consisting of accelerations in both lateral, longitudinal and vertical directions; the ambient variables which refer to temperature, pressure, noise and high frequency vibrations; while the spatial variables may refer to leg space and other seating variables.

The ride quality is generally quantified via the Sperling ride quality index, which measures the stability of vehicle in motion. The car-body acceleration time-history needs to be analysed and transported to the frequency domain prior to calculate the Sperling ride quality index. If n frequency components of the car-body acceleration spectrum in vertical direction are considered, the resultant Sperling ride quality index is:

$$W = \sqrt[10]{\sum_{i=1}^{n_f} W_{Z_i}^{10}} \quad (3.1)$$

where each contribution to the sum is defined as follow:

$$W_{Z_i} = \sqrt[10]{a(f_i)^3 B(f_i)^3} \quad (3.2)$$

where:

$a(f)$ denotes the amplitude of the acceleration response in $\left[\frac{m}{s^2}\right]$ of the i^{th} frequency identified by the Fast Fourier Transform (FFT)

$B(f)$ is the weighting factor which reflects the extent to which vibration causes the undesired effect at each frequency and for the case of the ride quality index it can be quantified with the following expression:

$$B(f) = 1.14 \sqrt{\frac{[(1 - 0.056 f^2)^2 + (0.645 f)^2] 3.55 f^2}{[(1 - 0.252 f^2)^2 + (1.547 f - 0.00444 f^3)^2](1 + 3.55 f^2)}} \quad (3.3)$$

A classification has been proposed, which relates the index with a corresponding feeling of ride quality. In this scale the higher is the value of the index W_Z , the lower is the ride quality:

¹Merriam-Webster dictionary, © 2019 Merriam-Webster, Incorporated

Index W_Z	Ride Quality
1.0	Very good
2.0	Good
3.0	Satisfactory
4.0	Acceptable for running
4.5	Not acceptable for running
5.0	Dangerous

Table 3.1: Ride Quality Scale

3.3. Ride Comfort

Track geometry, i.e. rail alignment, track irregularities, vehicle characteristics and speed generate motions that are felt by passengers and affect their sense of ride comfort. When studying the ride comfort one has to look at the frequency of the vibrations because different ranges of frequency correspond to different effect on the human body. There can be distinguished three categories:

- whole-body vibration
- hand-transmitted vibration
- motion sickness vibration

The whole-body vibrations generally range from 0.5 to 80 Hz. The hand-transmitted vibrations cause harmful effects when their frequency content is greater than 1000 Hz. The motion sickness can be induced by prolonged low-frequency, e.g. $f < 0.5$ Hz, translational and/or angular motions.

The Sperling index can be addressed also to the ride comfort when a different weighting factor $B(f)$ is applied:

$$B(f) = k \sqrt{\frac{1.911 f^2 + (0.25 f^2)^2}{(1 - 0.277 f^2)^2 + (1.563 f - 0.0368 f^3)^2}} \quad (3.4)$$

where $k = 0.588$ for the car-body vertical vibrations and $k = 0.737$ for the horizontal vibrations. Figure 3.1

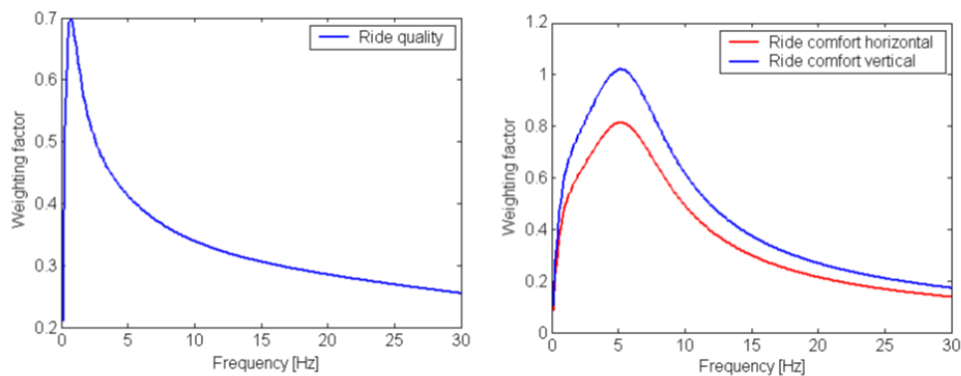


Figure 3.1: Weighting Factors. Picture taken from Dumitriu M. et al. (2015)

presents the trend of the weighting factor for both ride comfort and ride quality indices as a function of the frequency f . It can be noticed that when evaluating the ride comfort more weight is given to frequencies associated with the human response, i.e. $f > 0.5$ Hz.

As for the ride quality index, it is proposed a classification describing the relation between the ride comfort index and the responsiveness to the stimuli due to vertical and horizontal vibrations:

Index W_Z	Ride comfort
1.0	Just noticeable
2.0	Clearly noticeable
2.5	More pronounced but not unpleasant
3.0	Strong, irregular, but still tolerable
3.5	Very irregular
3.5	Extremely irregular, unpleasant, annoying; prolonged exposure intolerable
4.0	Extremely unpleasant; prolonged exposure harmful

Table 3.2: Ride Comfort Scale

Yang et al. [42] studied the response of train to track irregularity and riding comfort of train varying using the track classes 4, 5 and 6 designated by the Federal Railroad Administration (FRA), being class 6 the best quality track. they compared the outcoming accelerations with the limitations suggested by France-SNCF and Eurocode (1995), $a = 0.49m/s^2$ and $a = 1m/s^2$ respectively.

Dumitriu and Gheti [9] focused on the evaluation of the ride quality and comfort indexes for the vertical vibrations in railway vehicles generated by the track irregularities, i.e. longitudinal defect. The evaluation followed the Sperling W_Z method. The results showed that the variation of the damping of the secondary suspension affects the dynamic behaviour of the vehicle and hence, an appropriate selection of it may increase the ride quality and comfort.

Long et al. [25] in the final part of their feasibility study for the SFT prototype in Qiandao Lake in China addressed the problem of the human sense of security inside such submerged structure. They quantified the Sperling comfort index, which could have been used also for a further optimisation of the BWR in the structural design of the prototype, see Figure 3.2.

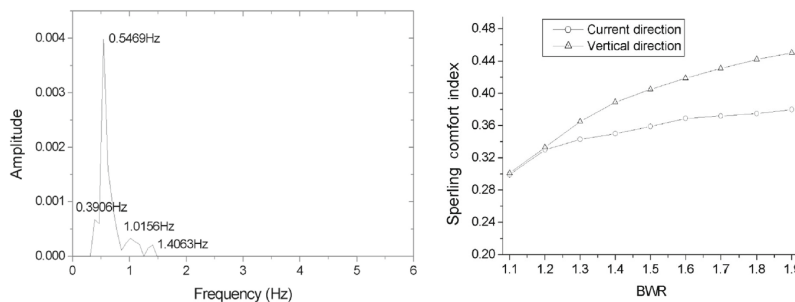


Figure 3.2: Excited frequencies and Sperling comfort index at the mid-span of a SFTP with different BWRs. Picture taken from Long et al. [25]

Choi et al. [4] studied the interaction between vehicle and structure by use of a full tridimensional train car system. In their analysis they included also all types of irregularities: longitudinal level Figure 3.3b, alignment Figure 3.3c and cross level Figure 3.3d. They performed simulations on the effects of derailment coefficients, lateral loads, bogie acceleration and body acceleration created by track irregularities to evaluate how the track irregularities affect the safety and ride comfort of Korean KTX high speed train. The results of these simulations indicated that track alignment had a significant impact on running safety while defects at longitudinal level did not.

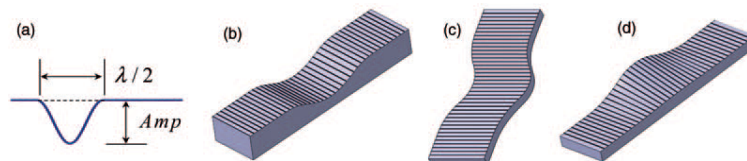


Figure 3.3: Type of irregularity. Picture taken from Choi et al. [4]

4

Methodology

4.1. Introduction

The methods to simulate the FSVI will be discussed in this chapter. Different vehicle models will be used in the analyses depending on the output quantity one is interested to investigate.

4.2. Vehicle Model

4.2.1. Moving Load

The moving load model, Figure 4.1 is the most common model used by researchers when studying the vehicle-induced structural vibrations. This model allows to describe the main dynamic characteristics of the tunnel due to the load passage with a good grade of accuracy, but it neglects the Vehicle-Structure Interaction (VSI). Hence, the moving load model is valid as long as the mass of the vehicle is small compared to that of the tunnel, and the research does not require a specific vehicle response.



Figure 4.1: Moving load model

Tariverdilo et al. [40], Yuan et al. [44] and Kwark et al. [22] applied this model, being their study aimed to give insight into the structural response of the SFT due to traffic load.

4.2.2. Moving Mass

Given that the mass of the vehicle is not negligible compared to the mass of the tunnel, a moving mass model, Figure 4.2, should be adopted instead. However, the linear moving mass model does not consider the contact loss between the moving mass and the structure. This phenomenon may be significant under the assumption that the rail presents longitudinal irregularities or when the design speed for the crossing is high.

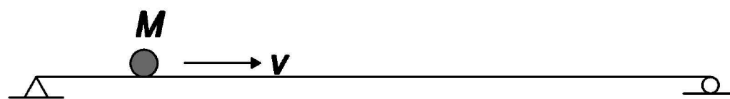


Figure 4.2: Moving mass model

4.2.3. Moving Sprung Mass

The vehicle model can be improved considering the elastic and damping effects of the suspension systems to be able to have information about the dynamic response of the mass. The simplest model of this kind is the 1DOF mass-spring-dashpot system, the so-called sprung mass model, Figure 4.3.

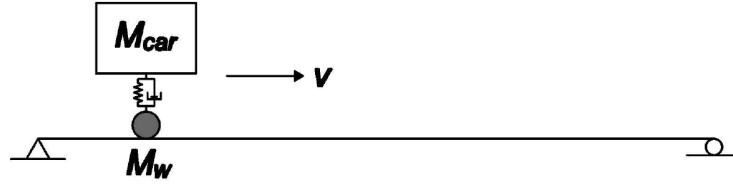


Figure 4.3: Moving sprung mass model

These three cases are studied in Fryba [13], where the structural dynamic response due to vehicle passage is mainly addressed, through both analytical and numerical solutions.

4.2.4. Moving Train Car

To account for the various dynamic properties of train cars, detailed vehicle models, i.e. 6 DOFs car-boogie model, have been developed and used by Youcef et al. [43] and Dumitriu [8], Dumitriu and Gheti [9], Dumitriu and Leu [10], Figure 4.4. All the locomotive components, the car body and the two bogies, were considered to have 2DOFs to account for the vertical and pitching motions. Different characteristics of suspension systems are adopted to describe the contact forces between the masses. The primary suspensions, whose constitutive parameters are k_{S1} and c_{S1} , act between the wheels and the bogies, while the secondary suspensions, whose constitutive parameters are k_{S2} and c_{S2} , act between the bogies and the train car. The use of simplified models can overcome convergence problems and may be used to understand the influence of specific parameters which are driving the dynamic response of the vehicle.

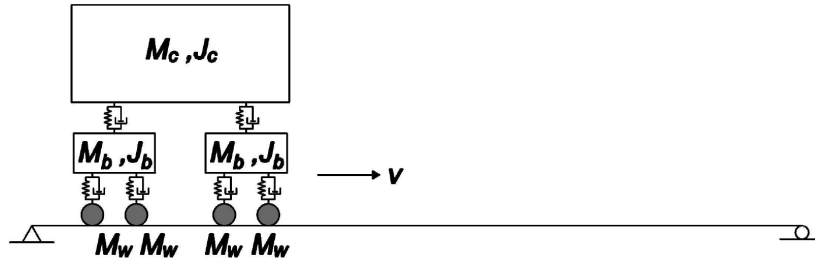


Figure 4.4: Moving train car model

4.2.5. Moving Train Car with Rail Irregularities

Irregularities in railway tracks may play a significant role in the behaviour of passing trains and large defects may result in insufficient ride quality and comfort and in special cases derailment. Hence, it seems worth including the track irregularities in the model developed in subsection 4.2.4, Figure 4.5. The irregularities are accounted for in the model as part of the vertical displacement, velocity and acceleration of the wheels, as done in Youcef et al. [43]:

$$\begin{aligned} z_{w_k} &= w_k(x_k, t) + r(x_k) & k = 1 : 4 \\ \dot{z}_{w_k} &= \dot{w}_k(x_k, t) + V(w'_k(x_k, t) + r'(x_k)) & k = 1 : 4 \\ \ddot{z}_{w_k} &= \ddot{w}_k(x_k, t) + 2V\dot{w}'_k(x_k, t) + V^2(w''_k(x_k, t) + r''(x_k)) & k = 1 : 4 \end{aligned}$$

where k is the number of wheel, $w_k(x_k, t)$ is the deflection of the tunnel at the position of the wheel and V is the vehicle velocity. The dot and prime in the expressions above refer to the time and spatial derivatives respectively.

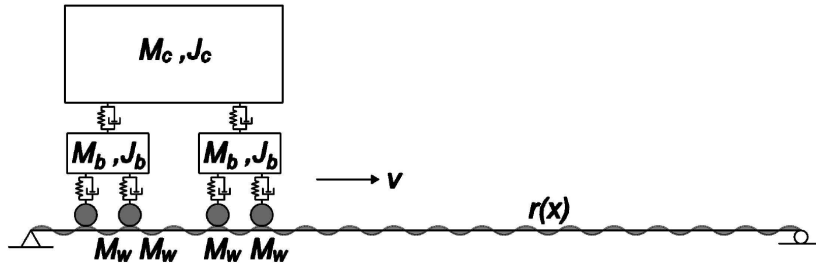


Figure 4.5: Moving train car model with rail irregularities

4.3. Tunnel Model

4.3.1. Simply Supported SFT

One of the possible configuration of a SFT is a free straight tunnel, connected only at the shores, Figure 1.7d. For this configuration the structure behaves as a simply supported beam and can be modelled as Euler-Bernoulli beam, being the cross-section much smaller than the span of tunnel. However, this model will be used as a benchmark while building the actual SFT model, but all subsequent models will use the same modal shapes as the simply-supported case, as the boundary conditions will not change. The Partial Differential Equation (PDE) that governs the dynamic bending vibrations of the tunnel can be expressed as in Clough and Penzien [5]:

$$m \frac{\partial^2 w(x, t)}{\partial t^2} + EI \frac{\partial^4 w(x, t)}{\partial x^4} = f(x, t) \tag{4.1}$$

where: $w(x, t)$ is the deflection that may be in the horizontal and vertical direction; m is the mass per unit length which includes the added mass given by the displaced water; EI is the bending stiffness; $f(x, t)$ is the generalised force acting on the tunnel which comprises the environmental forces and the passage of the vehicle.

Since the structural response is driven by the forced vibration, it is required to estimate the natural frequencies of the structure to be able to predict amplification or resonance phenomena, as the structure intends to vibrate in the mode whose frequency is equal or close to the forcing frequency. This PDE can be solved using the separation of variables method with modal superposition, see Appendix A, giving the resulting expression:

$$\omega_n = \sqrt{\left(\frac{n\pi}{L}\right)^4 \frac{EI}{m}} \tag{4.2}$$

4.3.2. Cable Supported SFT

The formulation of the dynamic behaviour of the tunnel showed in subsection 4.3.1 is valid when the SFT has a net buoyancy equal to zero. When this equality is not met, but there is an upward residual buoyancy RB , the structure can be balanced by providing tensile cables as shown below in Figure 4.6.

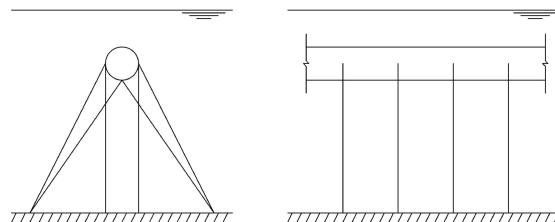


Figure 4.6: SFT with tensile cable

The pretension in the cables depends on the amount of residual upwards force, while their disposition can be vertical, inclined or a combination of the two, Figure 1.8, according to the required stiffness in the two motion planes. This last characteristic is a function of several parameters among which one can highlight: angle of inclination θ of the cable with respect to the vertical axis; pretension T_0 , cable diameter d_c , Young's

Modulus E of the cable material, cable length l_c . Starting from the aforementioned parameters and following the derivation in Appendix B, it is possible to formulate analytical expressions for the stiffnesses for sway and heave motions.

For vertical cables in sway motion

$$K_y = \frac{2 T_0}{l_c} \quad (4.3)$$

For vertical cables in heave motion

$$K_z = \frac{2 EA}{l_c} \quad (4.4)$$

For inclined cables in sway motion

$$K_y = \frac{2 EA}{l_c} \sin^2 \theta \quad (4.5)$$

For inclined cables in heave motion

$$K_z = \frac{2 EA}{l_c} \cos^2 \theta \quad (4.6)$$

These analytical expressions can be used to model the SFT as a simply supported beam on elastic supports BOES. However, no closed-form analytical solution exists for natural frequencies of such model. Sato et al. [36] studied the mathematical analogy between a BOES and a beam on elastic foundation BOEF. They concluded that the natural frequencies and vibration modes of a BOES and a BOEF are equivalent for K_v being lower than 0.05 and are still approaching for K_v lower than 0.5, Figure 4.7, where K_v is the so-called "relative stiffness of the supports" and is defined as:

$$K_v = \frac{k_v h^3}{24 EI} \quad (4.7)$$

where h is the cable spacing.

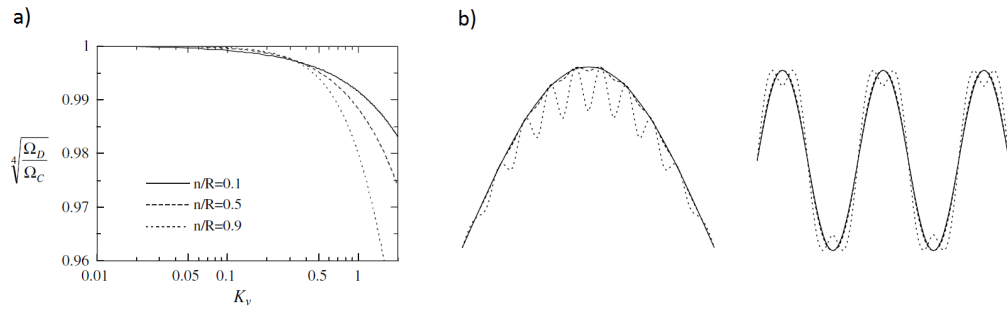


Figure 4.7: Comparison of natural frequencies (a) and modal shapes (b) of a BOES and a BOEF. Figures taken from Sato et al. [36].

The governing PDE for the dynamic analysis of a cable-stayed SFT is:

$$m \frac{\partial^2 w(x, t)}{\partial t^2} + EI \frac{\partial^4 w(x, t)}{\partial x^4} + k_f w(x, t) = f(x, t) \quad (4.8)$$

where $k_f = \frac{k_v}{h}$.

Following the derivation in Appendix C, the angular frequencies of free vibrations of a simply supported BOEF are as follow:

$$\omega_n = \sqrt{\left(\frac{n\pi}{L}\right)^4 \frac{EI}{m} + \frac{k_f}{m}} \quad (4.9)$$

(4.9) shows that the presence of the elastic foundation increases the natural frequencies of the system. Comparing (4.9) with (4.2), the only difference lies in the presence of the second addend under the square root, which represents the squared angular frequency of free vibration of a string with null bending stiffness.

When the parameter K_v is larger than 0.05 the governing PDE for the dynamic analysis of a cable-stayed SFT may be rewritten in the form:

$$m \frac{\partial^2 w(x, t)}{\partial t^2} + EI \frac{\partial^4 w(x, t)}{\partial x^4} + \sum_{N=1}^{n_c} k_v w(x_N, t) \delta(x - x_N) = f(x, t) \quad (4.10)$$

The substitution of $w(x, t) = \sum_{n=1}^{\infty} \Phi_n(x) \Psi_n(t)$, with $\Phi_n(x) = \sin \frac{n\pi}{L} x$ in (4.14) gives:

$$m \sum_{n=1}^{\infty} \Phi_n(x) \ddot{\Psi}_n(t) + c \sum_{n=1}^{\infty} \Phi_n(x) \dot{\Psi}_n(t) + EI \sum_{n=1}^{\infty} \Phi_n''''(x) \Psi_n(t) + k_f \sum_{n=1}^{\infty} \Phi_n(x) \Psi_n(t) = f(x, t) \quad (4.14)$$

The pre-multiplication in both sides of (4.15) by $\Psi_r(x)$ and the integration over the tunnel length gives, thanks to the orthogonality of the modes:

$$M_r \ddot{\Psi}_r(t) + C_r \dot{\Psi}_r(t) + K_r \Psi_r(t) = F_r(t) \quad (4.15)$$

where

$$\begin{aligned} M_r &= \int_0^L \Phi_r(x) m \Phi_n(x) dx \\ C_r &= \int_0^L \Phi_r(x) c \Phi_n(x) dx \\ K_r &= \int_0^L \Phi_r(x) EI \Phi_n''''(x) + \Phi_r(x) k_f \Phi_n(x) dx \\ F_r &= \int_0^L \Phi_r(x) f(x, t) dx \end{aligned}$$

Hence, M_r , C_r , K_r , F_r represents mass, damping and stiffness and load referred to the r^{th} vibration mode. This procedure allows to transform (4.14) into a set of infinite Ordinary Differential Equation (ODE) in the unknowns $\Phi_n(t)$. Each equation in (??) can be solved separately and the total deflection $w(x, t)$ and bending moment $M(x, t)$ can be obtained as the superposition of each modal contribution:

$$w(x, t) = \sum_{n=1}^{\infty} \Phi_n(x) \Psi_n(t) \quad (4.16a)$$

$$M(x, t) = -EI \sum_{n=1}^{\infty} \Phi_n''(x) \Psi_n(t) \quad (4.16b)$$

The modal analysis can be performed to approximate the natural frequencies of the structure. The presented model of BOEF is adopted in this calculation and all motions are considered, namely horizontal, vertical and rotational. The sinusoidal function can still be used as a modal shape for the BOEF since the boundary condition are not varied:

$$B.C. = \begin{cases} w(x, t)|_{x=0} = 0 \\ M(x, t)|_{x=0} = 0 \\ w(x, t)|_{x=L} = 0 \\ M(x, t)|_{x=L} = 0 \end{cases} \quad (4.17)$$

Hence, the mode shape can be expressed as:

$$\Phi(x) = \sin \frac{n\pi}{L} x \quad (4.18)$$

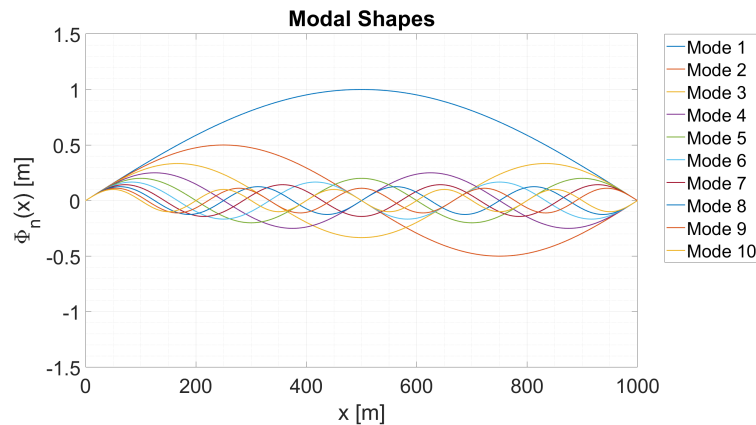


Figure 4.8: First 10 Mode Shapes

Using the same method as in (??) a model can be built which takes into account sway and heave motions as well as the rotation around the tunnel axis, which induced by the eccentrically passing train and by the

external supporting system, see Figure 5.2.

$$\begin{cases} m \ddot{w}_y + c_y \dot{w}_y + k_y w_y + EI w_y'''' - \frac{k_\varphi}{R} \varphi_x = 0 \\ m \ddot{w}_z + c_z \dot{w}_z + k_z w_z + EI w_z'''' = 0 \\ m a^2 \ddot{\varphi}_x + c_\varphi \dot{\varphi}_x + k_\varphi \varphi_x + GI_\varphi \varphi_x'' - k_y R w_y = 0 \end{cases} \quad (4.19)$$

In (4.19) the $\dot{}$ represents the time derivative, while the $'$ the spatial derivative. A system of ODEs, which can be grouped in matrix form, can be built using the modal expansion.

4.6. Simulation Method

The models were implemented in the MATLAB[®] environment. The single-step solver ode45 has been utilised, giving in output a sampling time of $dt = 0.01$. Dynamic analyses were carried out considering the variation of different parameters to provide insights regarding their influence in the ride comfort assessment.

The parameters that have been modified in the different analyses are

- Cable inclination: (15°, 30°, 45°, 60°)
- Vehicle velocity: ($50 \frac{m}{s}$, $100 \frac{m}{s}$)
- Damping c_{S1} and c_{S2} of primary and secondary car suspension systems
- Load Cases: two waves and two currents scenarios for a total of possible combinations of eight load cases
- Amplitude r_0 of the longitudinal irregularity
- Wavelength γ_0 of the longitudinal irregularity

To compute the Sperling Ride Quality and Comfort indexes the FFT of the acceleration is executed and the spectrum plot is generated for a frequency interval up to $f = 80Hz$ as previously discussed in section 3.3.

To obtain a solution for the problem, whose results are presented in chapter 6, some simplification are applied.

- One train running inside the tunnel
- Rail track positioned at a distance λ from the middle of the tunnel
- Constant velocity of the train
- Seabed has constant depth of 150m along the tunnel length

5

Case Study

5.1. Introduction

In this section the structural parameters of the SFT will be determined by means of a static analysis. These parameters are the external diameter D_e , the internal diameter D_i , the thickness of the wall of the tunnel t and the consequent bending stiffness EI . The analysis will be carried out separately for the vertical and horizontal direction and all static loads will have an equilibrium configuration.

The cables are the only stabilising system and they will affect both the vertical and horizontal force equilibrium. The vertical component and the gravity should counteract the buoyancy, while the horizontal component should balance the current's force acting on the tunnel. The internal diameter needs to be predetermined in order to be able to accommodate two railway tracks, lateral maintenance corridors and ballast chambers, Figure 5.1¹. Using characteristic dimensions of twin-track single-bore tunnels an internal diameter $D_i = 15m$ seems to be big enough to accommodate the aforementioned systems.

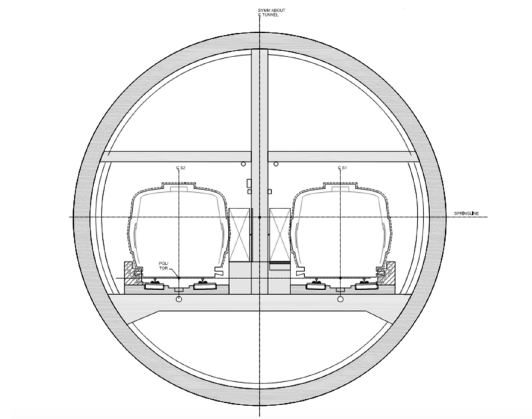


Figure 5.1: Twin-Track Bore Tunnel. Picture taken from ¹

5.2. Cross-Section Geometry and Dimension

The adopted shape for the cross-section is circular. The diameters D_e and D_i and the thickness t of the tunnel section are obtained via a iteration process. The properties of materials used for the analyses have been summarised in the table below:

¹BART Silicon Valley, Phase II Single Bore Tunnel Technical Studies: Executive Summary Report Final April 10, 2017

Material	E (GPa)	ν	G (GPa)	R_{ck} (MPa)
Concrete	30	0.15	13	50
Steel	210	0.3	81	235
Steel	210	0.3	81	540

Table 5.1: Material Properties

A lower boundary to the BWR is set as a target at which the iterations can be stopped. The results of the process and hence, the cross-sectional dimensions are reported in the table below:

D_i (m)	t_c (m)	t_s (m)	D_e (m)	A_c (m^2)	A_s (m^2)
15.5	1.2	0.05	18	2.82	62.96

Table 5.2: Cross-Section Dimensions

where t_c and t_s are the thickness of the concrete tunnel and of the external steel tube respectively. With the given dimensions it is possible to compute the bending and torsional stiffnesses of the tunnel section and the permanent forces acting on it:

EI (Nm^2)	GJ (Nm^2)	Weight G_1 (N/m)	Buoyancy G_3 (N/m)	BWR
$9 \cdot 10^{13}$	$7.6 \cdot 10^{13}$	$1.69 \cdot 10^6$	$2.5 \cdot 10^6$	1.48

Table 5.3: Cross-Section Stiffness and Permanent Loads

5.3. Tunnel Arrangement

The general line arrangement, shown in Figure 5.2, features a straight tube with an alternating cable configuration. Despite the Hainan Strait crossing is 10km long, the total length adopted in the current study is fixed to $L = 1 km$ to limit the computational time. The cables are evenly spaced along the length of the tunnel. Both vertical and inclined cables feature spacing $s = 100m$ hence, a support is provided every 50m.

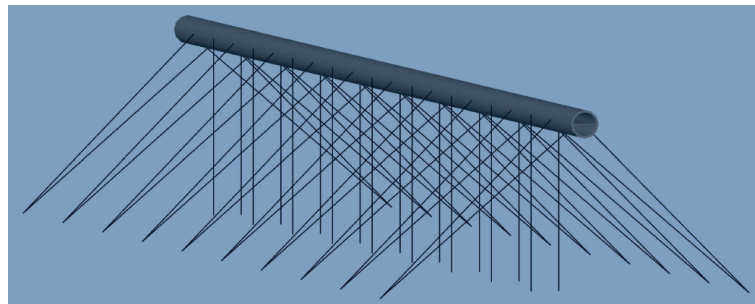


Figure 5.2: Tunnel Arrangement

From the forces equilibrium it is found that a diameter of $d_c = 250mm$ is required to counteract the residual buoyancy. Using the expressions derived in Appendix B the value of the stiffness can be computed as a function of the inclination θ , Figure 5.3.

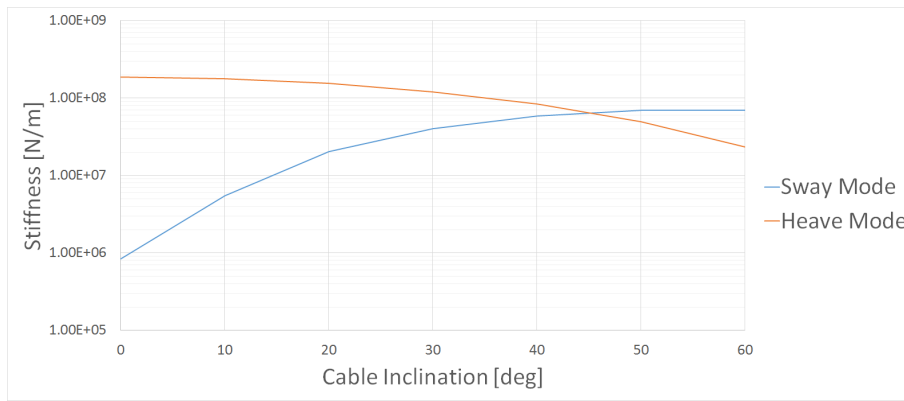


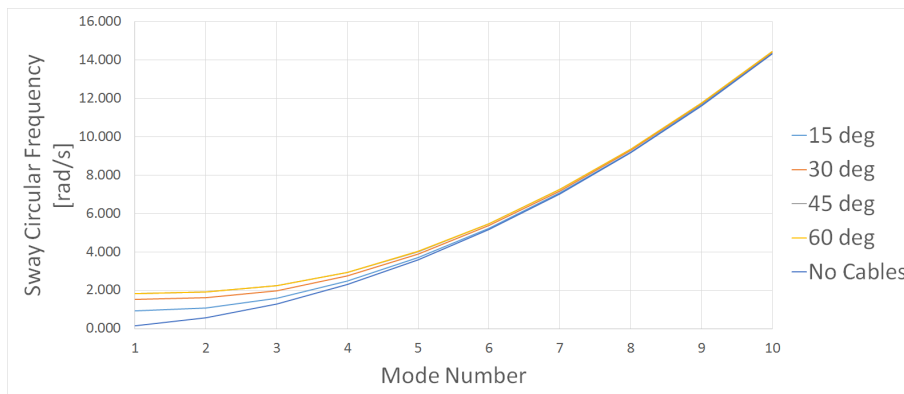
Figure 5.3: Cable Stiffness vs. Inclination θ

Being the difference in the vertical and horizontal components in the interval $30^\circ < \theta < 60^\circ$ limited, an optimal selection may be $\theta = 45^\circ$ when referring to the inclined cables. The corresponding value of the stiffness is:

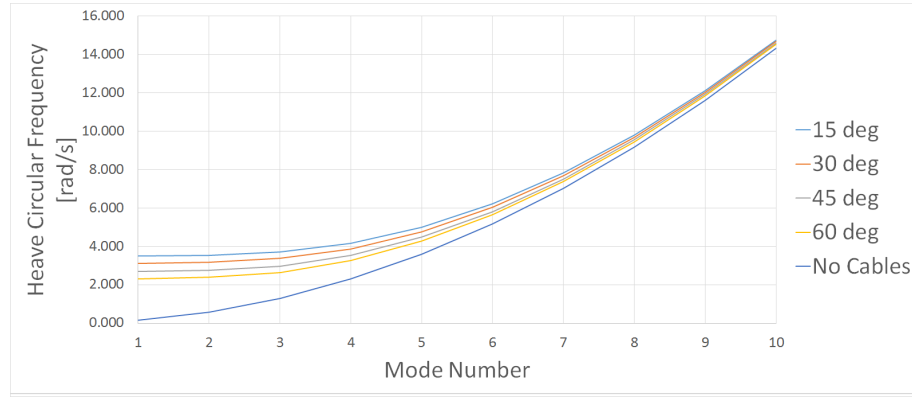
θ (deg)	L_c (m)	k_y (N/m)	k_z (N/m)
0	111	$8.38 \cdot 10^5$	$3.71 \cdot 10^8$
45	156.98	$1.31 \cdot 10^8$	$1.31 \cdot 10^8$
50	157.49	$1.52 \cdot 10^8$	$1.01 \cdot 10^8$

Table 5.4: Cable Inclination and Stiffness

Along with the variation of the stiffness, the natural frequencies of the structure shift too. The natural frequency for heave modes appears to reduce as the inclination increases and vice versa the natural frequency for sway modes increase, being the supports stiffer. It is expected that for the chosen inclination $\theta = 45^\circ$, the natural frequency for both heave and sway modes are equal, being the stiffness in horizontal and vertical direction equals. This is not the case when vertical cables are also present in the model. Using the expression given in (4.9) the natural frequencies of the structure may be approximated and the results are plotted below in Figure 5.4.



(a)



(b)

Figure 5.4: (a) Horizontal Natural Frequency. (b) Vertical Natural Frequency.

It can be noticed that the presence of the supported system increases the natural frequencies, but this change is relevant for the first modes only. For higher order modes the first addend of (4.9), i.e. the natural frequency of a simply supported beam, becomes much bigger than the contribution of the external support and hence, the natural frequency is not much affected by the difference of the inclination θ .

5.3.1. Modal Analysis

Using the procedure presented in section 4.5 it is possible to approximate the natural frequencies of the structure. Neglecting the damping, the natural frequencies may be evaluated and are presented in Table 5.5 and Table 5.6 below.

Mode Number	1	2	3	4	5
Mode Shape	H	H	H	V	V
Natural Frequency [Hz]	0.292	0.305	0.356	0.427	0.436
Mode Number	6	7	8	9	10
Mode Shape	H	V	V	H	V
Natural Frequency [Hz]	0.467	0.473	0.561	0.640	0.712
Mode Number	11	12	13	14	15
Mode Shape	H	V	H	V	H
Natural Frequency [Hz]	0.871	0.925	1.155	1.197	1.489
Mode Number	16	17	18	19	20
Mode Shape	V	H	V	T	H
Natural Frequency [Hz]	1.521	1.871	1.897	2.313	2.312
Mode Number	21	22	23	24	25
Mode Shape	V	T	T	T	T
Natural Frequency [Hz]	2.318	3.602	5.347	7.104	8.865
Mode Number	26	27	28	29	30
Mode Shape	T	T	T	T	T
Natural Frequency [Hz]	10.628	12.392	14.157	15.923	17.699

Table 5.5: Wet Natural Frequencies. Where H, V, T stand for horizontal, vertical and torsional mode shape respectively.

Mode Number	1	2	3	4	5
Mode Shape	H	H	H	V	V
Natural Frequency [Hz]	0.459	0.480	0.560	0.672	0.686

Mode Number	6	7	8	9	10
Mode Shape	H	V	V	H	V
Natural Frequency [Hz]	0.735	0.745	0.884	1.008	1.121
Mode Number	11	12	13	14	15
Mode Shape	H	V	H	V	T
Natural Frequency [Hz]	1.371	1.457	1.818	1.883	1.898
Mode Number	16	17	18	19	20
Mode Shape	H	V	H	V	T
Natural Frequency [Hz]	2.343	2.394	2.945	2.985	3.602
Mode Number	21	22	23	24	25
Mode Shape	H	V	T	T	T
Natural Frequency [Hz]	3.640	3.649	5.347	7.104	8.865
Mode Number	26	27	28	29	30
Mode Shape	T	T	T	T	T
Natural Frequency [Hz]	10.628	12.392	14.157	15.923	17.699

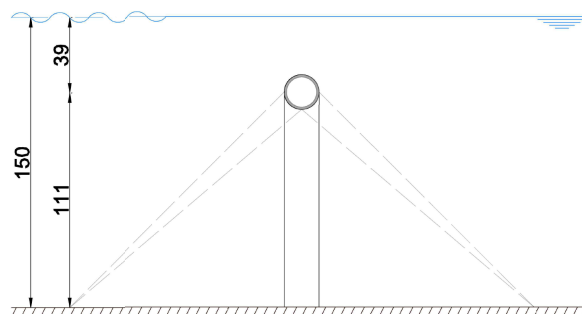
Table 5.6: Dry Natural Frequencies

5.4. Cable Properties

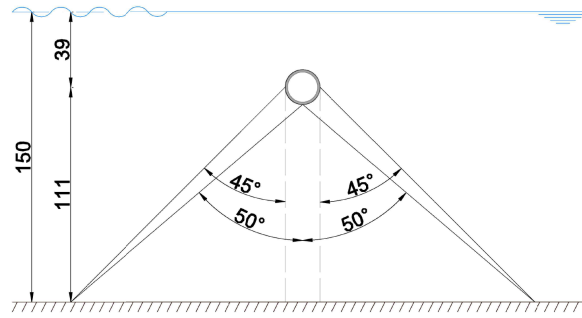
As it has been shown in subsection 4.3.2 the cable system can be modelled as a series of linear springs, with stiffness that depends on the inclination θ . A picture of the characteristic sections of the cable configurations can be seen in Figure 5.5. The mechanical properties of the material of the cables are summarised in Table 5.7 below.

Material	Density (kg/m^3)	E (GPa)	f_{ck} (MPa)
Steel	7500	210	540
High Strength Carbon Fibre	1440	237	3300

Table 5.7: Cable Material Properties



(a)



(b)

Figure 5.5: (a) Characteristic Section Vertical Cables. (b) Characteristic Section Inclined Cables.

5.5. Sea Loading

As mentioned in section 4.6 four sea states are considered for the simulations. Rather than the sea surface condition, one is interested in the calculation of the kinematic quantities, e.g. velocity and acceleration of the fluid particles, at the depth where the tunnel is located. The two wave states are characterised by different wave steepness S , which is defined as the ratio between the wave height H_W to the wavelength $\lambda_{w,p}$, but it should not be confused for the slope between a wave crest and the near trough, Figure 5.7. Table 5.8 offers a summary of these wave input parameters and Figure 5.6 presents the wave spectra of the two wave loading conditions.

From the spectrum analysis in Figure 5.6 it can be observed that the energy is concentrated in the frequency range up to 0.3 Hz . From the modal analysis, presented in subsection 5.3.1, the natural frequencies of the tunnel have been approximated and when comparing these with the excitation frequency interval, it can be highlighted that the energy exerted by the waves on the structure is very small, as the structural natural frequencies are larger.

$H_{W,S}$ (m)	T_P (s)	$\lambda_{w,p}$ (m)	$\omega_{w,p}$ (rad/s)	$k_{w,p}$ (rad/m)	S	$d/\lambda_{w,p}$
5	8	100	0.785	0.063	0.05	1.5
4.5	12	225	0.524	0.028	0.02	0.7

Table 5.8: Wave Parameters

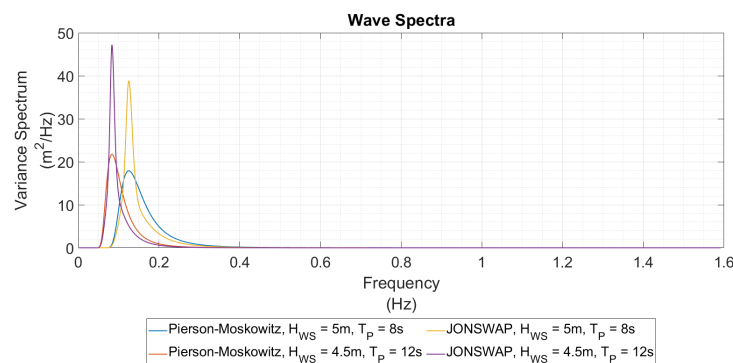


Figure 5.6: Pierson-Moskowitz and JONSWAP Spectra for the two significant wave heights considered

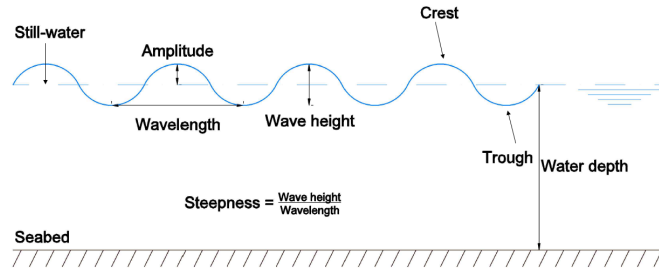


Figure 5.7: Wave Parameters

Waves can be classified via the water depth-to-wavelength ratio as deep water, transitional water and shallow water waves, where each interval corresponds to a particular shape of the orbit of the water particles, circular, oval and elliptical respectively. The numerical boundaries for each interval are:

$$\begin{aligned}
 0 < \frac{d}{\lambda} < \frac{1}{20} & \text{ Shallow Water} \\
 \frac{1}{2} < \frac{d}{\lambda} < \frac{1}{20} & \text{ Transitional Water} \\
 \frac{d}{\lambda} > \frac{1}{2} & \text{ Deep Water}
 \end{aligned}$$

According to this classification the presented study deals with deep water waves. Hence, to compute the kinematic quantities the simplified Airy's formulas may be used.

$$\begin{aligned}
 \text{Horizontal Particle Velocity} & \quad V_y = \omega a e^{k_{w,p}z} \sin \omega t \\
 \text{Vertical Particle Velocity} & \quad V_z = \omega a e^{k_{w,p}z} \cos \omega t \\
 \text{Horizontal Particle Acceleration} & \quad \dot{V}_y = \omega^2 a e^{k_{w,p}z} \cos \omega t \\
 \text{Vertical Particle Acceleration} & \quad \dot{V}_z = -\omega^2 a e^{k_{w,p}z} \sin \omega t
 \end{aligned} \tag{5.1}$$

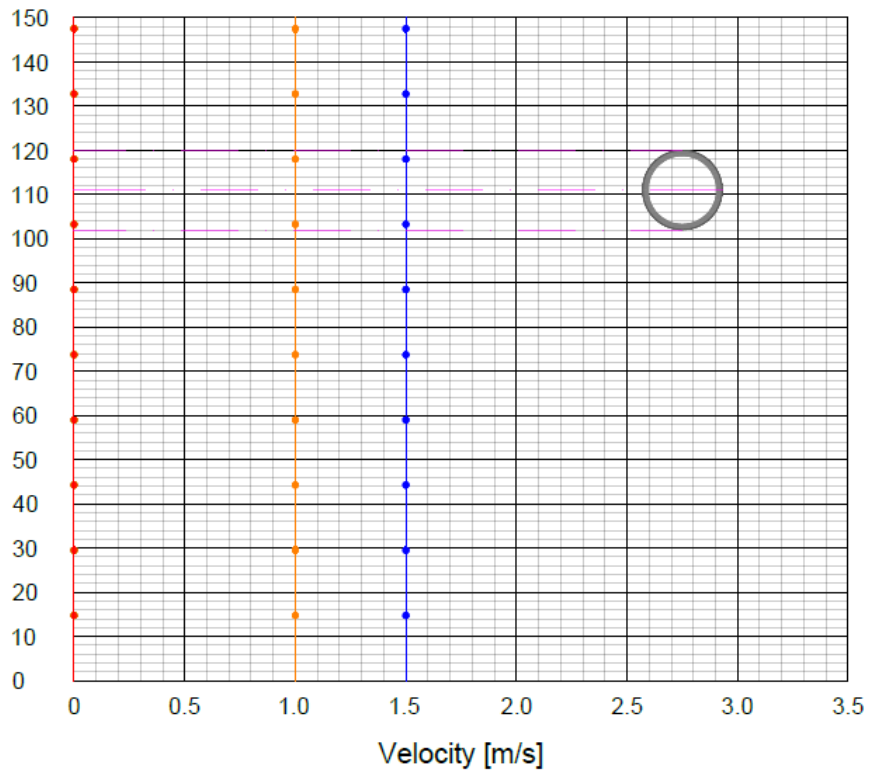
where a is the wave amplitude equal to half of the wave height. In (Martire [28]) it is also discussed, according to DNV [7], MacCamy and Fuchs [27], the limit of applicability of Morison's formulation for describing the FSI as a function of the diameter to wavelength ratio. The author concluded that the formulation can be assumed to be valid when $\frac{D_{ext}}{\lambda_{w,p}} \leq 0.2$. Regarding this criterion the two analysed scenarios fall within this limit of applicability, being the ratio respectively:

$H_{W,S}$ (m)	$D/\lambda_{w,p}$
5	0.18
4.5	0.08

Table 5.9: Applicability of Morison's Formulation

Analysing the load case of current flow, it is assumed that the value at sea surface level remains constant along the depth. Figure 5.8a and Figure 5.8b present the particle velocity for the different separate cases and Figure 5.8c their possible combinations.

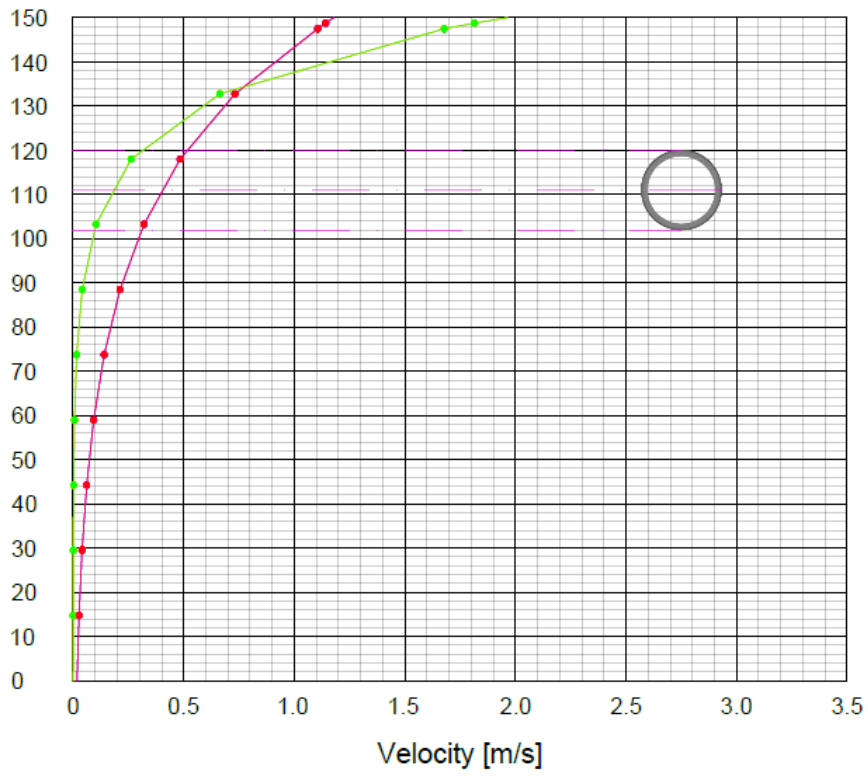
Current



—●— Horizontal Orbital Velocity, $v_c=1\text{m/s}$
—●— Vertical Orbital Velocity, $v_c=1\text{m/s}$
—●— Horizontal Orbital Velocity, $v_c=1.5\text{m/s}$
—●— Vertical Orbital Velocity, $v_c=1.5\text{m/s}$

(a) Current Profile

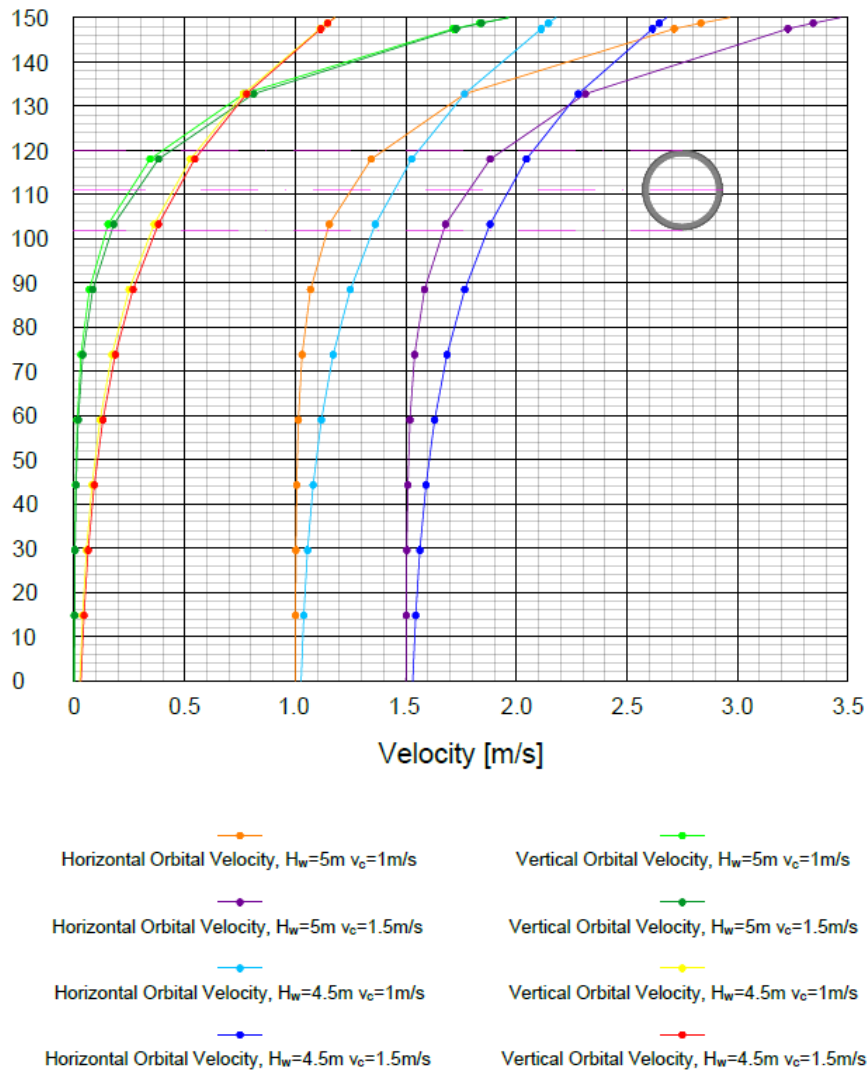
Wave



—●— Horizontal Orbital Velocity, $H_w=5\text{m}$ —●— Vertical Orbital Velocity, $H_w=5\text{m}$
—●— Horizontal Orbital Velocity, $H_w=4.5\text{m}$ —●— Vertical Orbital Velocity, $H_w=4.5\text{m}$

(b) Wave Profile

Wave and Current



(c) Wave and Current Profile

Figure 5.8: Particle velocity at tunnel location

From Figure 5.8c it can be seen how important is the current flow influence on the horizontal particle velocity. The reason for that lies in the composition of the flow itself, which is assumed to be purely horizontal, being the vector of the flow velocity:

$$\vec{V} = \begin{bmatrix} v_y \\ 0 \end{bmatrix} \quad (5.2)$$

5.6. Train Car Parameters

The vehicle model used in the analyses is a 6DOFs as it can be seen from Figure 5.9. The degrees of freedom that are considered are the vertical motion and the pitching of the train car and the bogies. These DOFs can be decomposed in just vertical movements at each suspension system, which characterise the contact forces between all the different components and can be later combined to show the vertical motion and pitching of

the single masses. Here in Table 5.10 are reported the parameters of each component of the vehicle:

Car-body Mass	m_c	(kg)	$3.4 \cdot 10^4$
Bogie Suspended Mass	m_b	(kg)	$3.2 \cdot 10^3$
Wheel Mass	m_w	(kg)	$1.5 \cdot 10^3$
Car body pitch inertia moment	J_c	($kg\ m^2$)	$2.31 \cdot 10^6$
Bogie body pitch inertia moment	J_b	($kg\ m^2$)	$3.12 \cdot 10^3$
Stiffness Secondary Suspension	k_{S2}	($\frac{N}{m}$)	$1.72 \cdot 10^6$
Damping Secondary Suspension	c_{S2}	($\frac{N\ s}{m}$)	$8.82 \cdot 10^4$
Stiffness Primary Suspension	k_{S1}	($\frac{N}{m}$)	$1.87 \cdot 10^6$
Damping Primary Suspension	c_{S1}	($\frac{N\ s}{m}$)	$1.05 \cdot 10^4$
Fixed Wheelbase	L_b	(m)	2.5
Distance between Bogie Pivot Centres	L_c	(m)	18.0
Wheel Radius	r_w	(m)	0.4575
Car-body Length	L_{car}	(m)	24.9
Static Load at each Wheel	P_0	(N)	$1.6 \cdot 10^5$

Table 5.10: Train Car Parameters

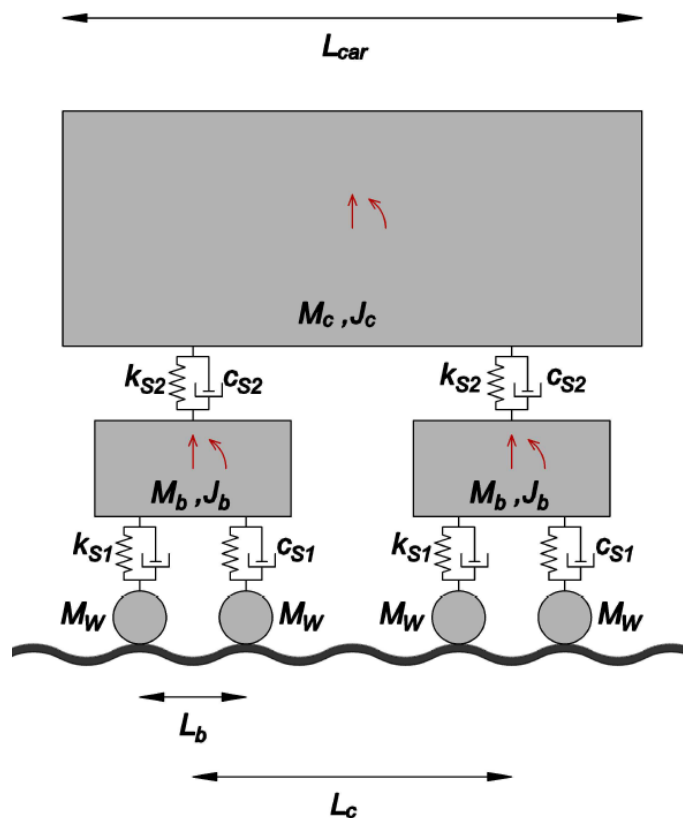


Figure 5.9: Train Car

The value of damping of the suspension systems c_{S1} and c_{S2} will be varied in section 6.7 to address the

importance of it for the level of comfort in the train car. The analysis of the train car natural frequencies needs to be addressed to be able to understand the FSVI. Mass, Damping and Stiffness matrices can be assembled for the 6DOFs system and the eigenvalue problem can be solved assuming the ground motion equal to zero, see Appendix F. The natural frequencies of the train vertical and pitching movements are obtained and are reported here below:

Mode Number	1	2	3	4	5	6
Mode Shape	V	P	V	V	P	P
Circular Frequency $\left[\frac{rad}{s}\right]$	6.69	8.98	41.56	41.56	43.28	43.28
Natural Frequency [Hz]	1.065	1.43	6.62	6.62	6.89	6.89
Vibration Period [s]	0.94	0.70	0.15	0.15	0.145	0.145

Table 5.11: Train Car Natural Frequencies, where V and P refer to the vertical and pitch motions respectively.

5.7. Longitudinal Rail Defect

The adopted vehicle and tunnel models allow to implement the longitudinal defect only. In the current study it is chosen an harmonic shape of the irregularity. Several simulations are run for values of amplitude r_0 and wavelength γ_0 of the irregularity. A characteristic expression of the longitudinal defect at the location of the load is:

$$r(x) = -r_0 \sin \frac{2\pi}{\gamma_0} V t \quad (5.3)$$

Choi et al. [4] is used as reference for what regards the values to be adopted for the different classes of irregularity and these are:

r_0 (m)	γ_0 (m)	f_0 (Hz)
$7 \cdot 10^{-3}$	5	10
$8 \cdot 10^{-3}$	10	5
$9 \cdot 10^{-3}$	30	$\frac{10}{6}$
$1 \cdot 10^{-2}$	50	1
$1.2 \cdot 10^{-2}$	100	0.5
$1.5 \cdot 10^{-2}$		1

Table 5.12: Amplitude and Wavelength of the Defect as in Choi et al. [4]

where the frequency is computed as the ratio between the velocity of the vehicle V and the wavelength γ_0 and the two columns refer to the two design velocity of $50 \frac{m}{s}$ and $100 \frac{m}{s}$ respectively.

6

Results

6.1. Introduction

The results of the simulations, in which one at a time the parameters are varied, as mentioned in section 4.6, will be presented in this chapter. In section 6.2, section 6.3 and section 6.4 the focus will be fixed to the structural response, while in section 6.5, section 6.6, section 6.7 and section 6.8 the attention is moved to the vehicle response and the comfort evaluation.

6.2. Influence of the Vehicle Model

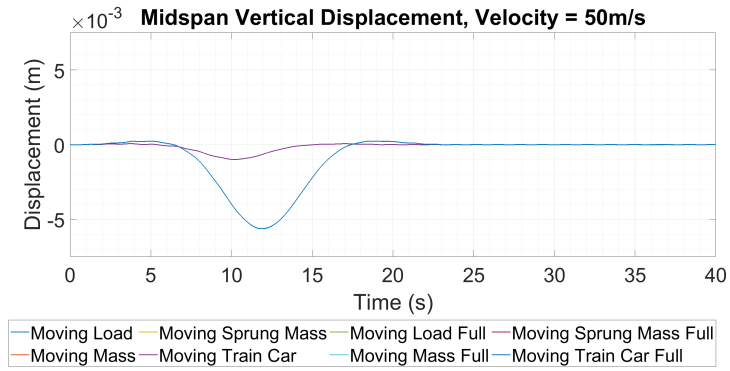
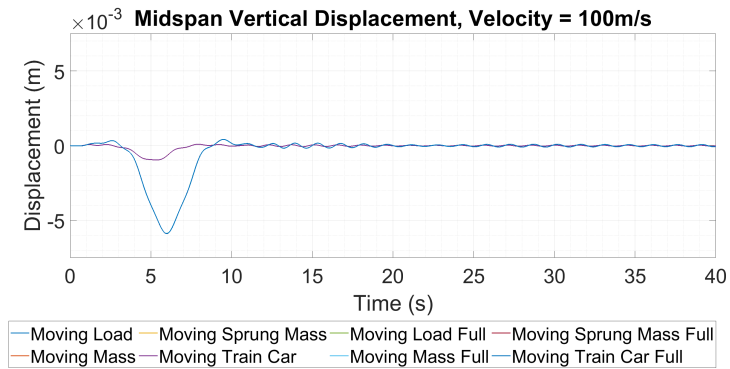
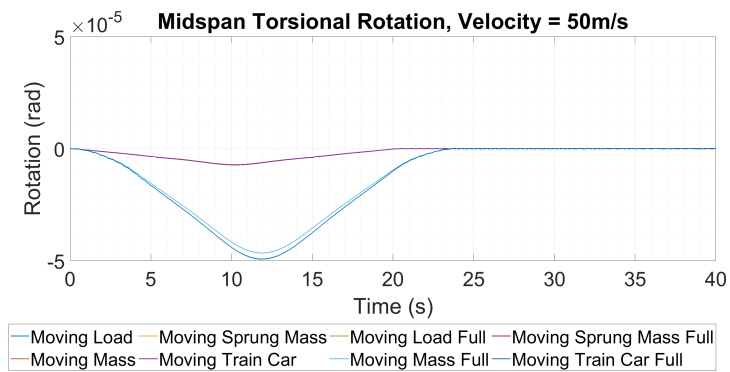
As it has been presented in chapter 4, several vehicle models have been built in order to study the FSVI at different levels. A comparison between the vehicle models is presented here in this section. To address possible differences in the response the focus will be set to the structural response. To better understand this difference between the models, the environmental load case is taken out of the simulation and the dynamic midspan vibration are used as output. Figure 6.1 shows the midspan responses in terms of vertical displacement and rotation around the tunnel axis. The latter is caused by the eccentricity of the load application, being the railway at a distance $\lambda = 4m$ from the vertical symmetry axis. Two main scenarios are presented in the plots: the passage of one single train car and the passage of the whole train, composed by eight cars. The first thing that can be observed is that the time that the vehicle takes to cross the tunnel depends on the velocity of the vehicle. In the current simulation, being the velocity $V = 50 \frac{m}{s}$ and $V = 100 \frac{m}{s}$, the passage time is:

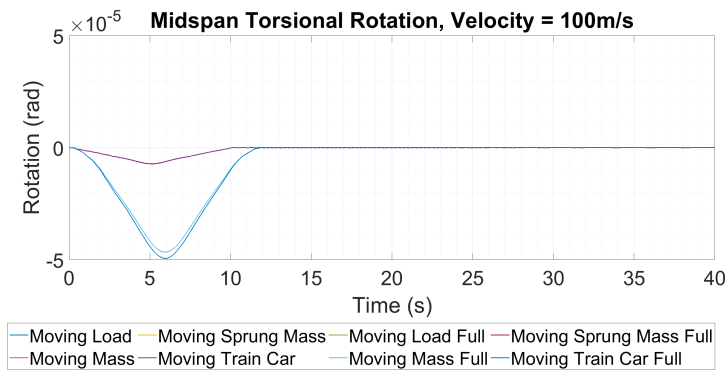
$$t_{LV} = \frac{L}{V} = \frac{1000}{50} = 20s \quad (6.1a)$$

$$t_{LV} = \frac{L}{V} = \frac{1000}{100} = 10s \quad (6.1b)$$

where L is the span of the crossing. A small difference in the magnitude of the response can be found for the cases where the vehicle is modelled as shown in Figure 4.3 and Figure 4.4. This difference, which appears to be more visible for the rotation $\varphi_x(\frac{L}{2}, t)$ of the cross-section, is quantified to reach a maximum value of 5% compared to the moving load vehicle model. When looking at the midspan vertical displacement in Figure 6.1a and Figure 6.1b, just two lines are visible. These two lines comprises all four vehicle models respectively, as the vehicle-structure interaction is negligible.

Starting from the rotation, the additional contribution to the vertical displacement can be computed and it is found to amount for 10% of the vertical deflection, as the order of magnitude for the rotation is $10^{-5} rad$ and $R_{ext} = 9m$.

(a) Vertical Displacement at midspan for $V = 50 \frac{m}{s}$ (b) Vertical Displacement at midspan for $V = 100 \frac{m}{s}$ (c) Torsional Rotation at midspan for $V = 50 \frac{m}{s}$



(d) Torsional Rotation at midspan for $V = 100 \frac{m}{s}$

Figure 6.1: Midspan Response for Different Vehicle Models, where Full means the entire vehicle composed by eight cars.

Resonance phenomena in the structure can occur for specific values of the vehicle velocity. A pragmatic estimation of the critical velocities can be evaluated imposing the equality of the forcing frequency $\Omega_n = \frac{n\pi V}{L}$ to the natural frequencies of the structure, presented in (4.9). Such velocity values cannot be accepted as they are because the adopted modal shapes are taken from the case of a simply-supported beam, but they can orientate the choice of a design speed. An expression for V_{cr} can then be found as a function of the modal shape as:

$$V_{cr} = \frac{\sqrt{\left(\frac{n\pi}{L}\right)^4 \frac{EI}{m} + \frac{k_f}{m}}}{\frac{n\pi}{L}} \tag{6.2}$$

Figure 6.2 shows that the critical velocity is always bigger than the design velocity of the crossing, so no resonance phenomena are expected to occur.

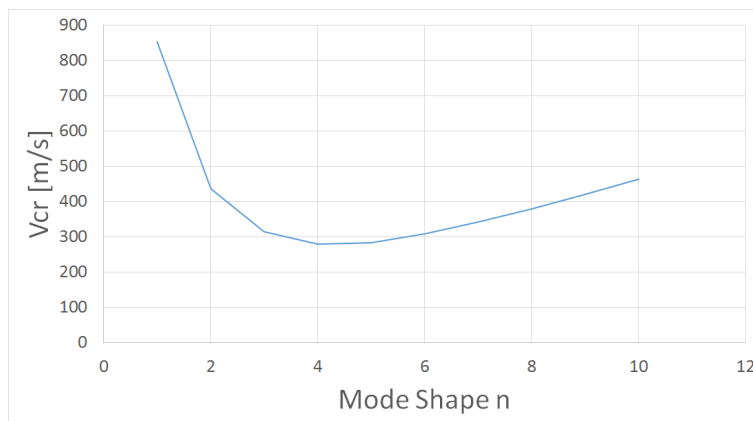


Figure 6.2: Vehicle Critical Velocity at each mode

Figure 6.3 shows the absolute maximum displacement for the midspan time-history against the velocity of the train. The train in this case has been modelled as moving load, as the focus is set on the structural response. Moreover, it has been decided to study the problem avoiding the environmental loading from wave action, as they are driving the global FSVI, see section 6.4. When excluding the presence of wave action, it has been also chosen to do not account for the presence of currents flows as well because a flow in just the horizontal direction does not generate noticeable coupling between the sway and heave motion, see Figure 6.9b. Hence, it is adopted a condition of steady-still fluid around the tunnel to evaluate the critical value of the running train. From Figure 6.3 it is visible that the critical velocity V_{cr} for the structural response is around $V = 300 \frac{m}{s}$ and this value is also in line with the lowest value of critical velocity that has been found with regard to the equality of the forcing frequency and the natural frequency in (6.2)

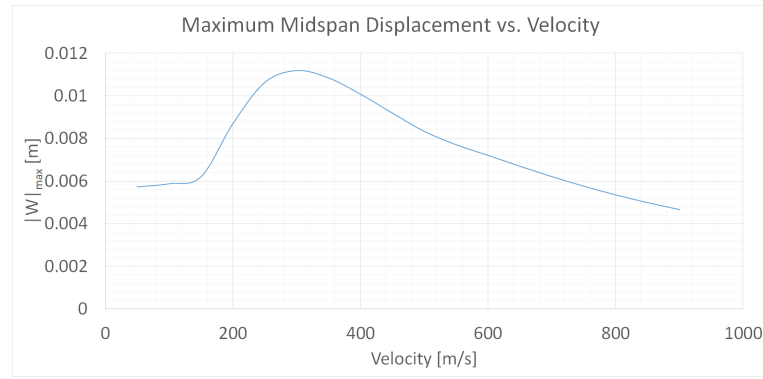


Figure 6.3: Maximum Displacement vs. Velocity at midspan

In Graff [14] the author finds an expression of the critical velocity applicable to beam on elastic foundation which is

$$V_{cr} = \left(\frac{4 k EI}{\rho^2 A^2} \right)^{\frac{1}{4}} \quad (6.3)$$

where k represents the stiffness of the foundation, EI the bending stiffness and ρ and A the mass per unit length and the cross-sectional area respectively. From Figure 6.4 it is shown that when studying the change of the critical velocity with the variation of the cable spacing, this follows the behaviour described by Graff with the expression (6.3). It is found that the critical velocity decrease at the increase of the cable spacing. The reason is because an increase in the cable spacing cause a reduction in the foundation stiffness, while all other parameters are not changing, as they are referred to the cross-section of the beam. The two models of BOES and BOEF show the same behaviour, i.e. the lines find almost perfect overlap, because for each of the described cable spacing the non-dimensional parameter K_v , defined as (4.7), is still smaller than the upper bound 0.05 as discussed in Sato et al. [36]. Hence, the variation of the critical velocity is not due to a local effect at cable-span level.



Figure 6.4: Maximum Displacement vs. Velocity for a BOES and a BOEF

The critical velocity appears also not to be affected by a global effect such as the change of the length of

the crossing, see Figure 6.5. In fact, it can be observed that the maximum displacement occurs always for a velocity of $V = 300 \frac{m}{s}$, as the cable spacing is kept constant when varying the length.

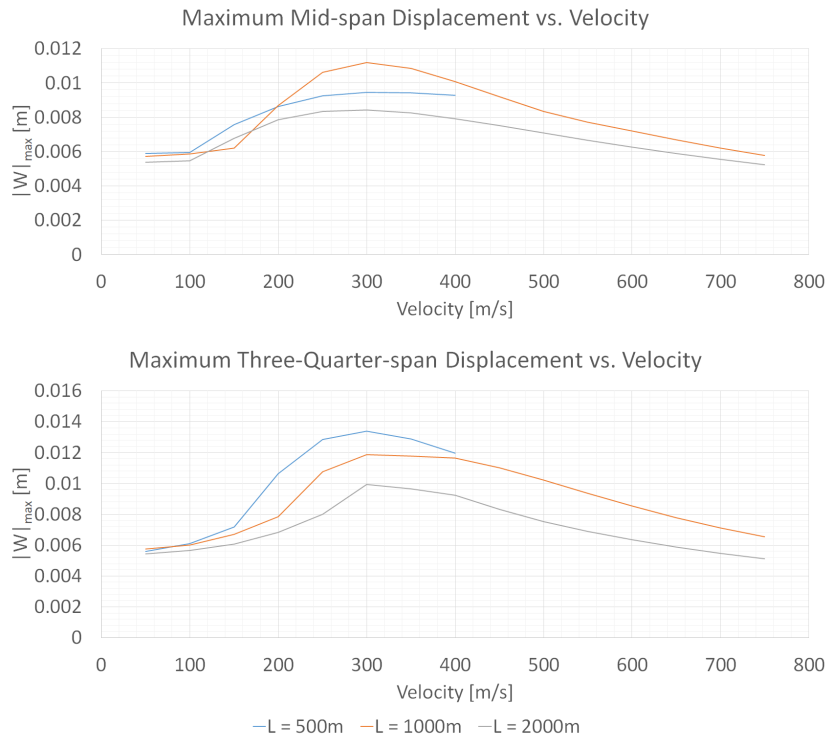


Figure 6.5: Maximum Displacement vs. Velocity for different tunnel length with cable spacing 100m

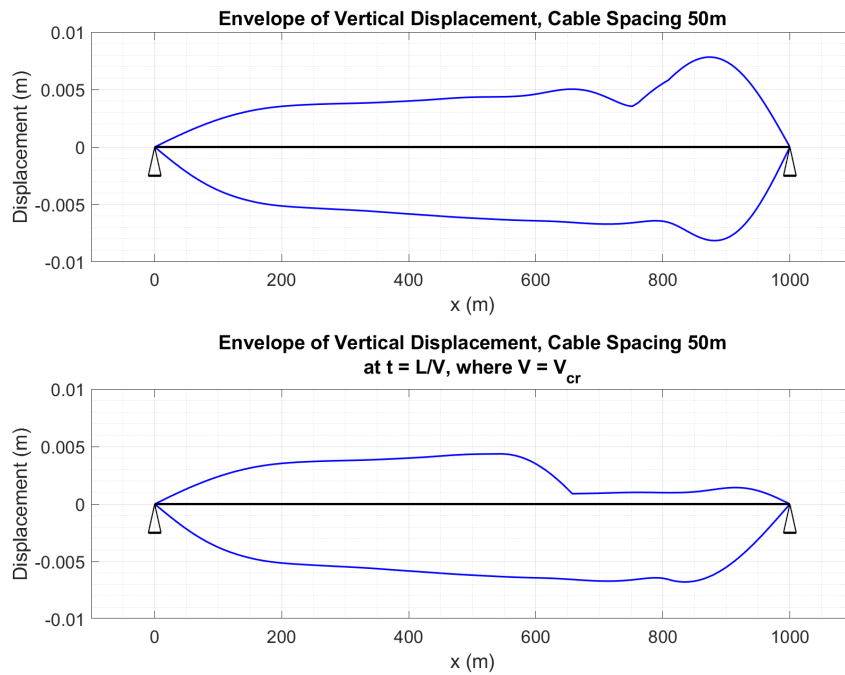
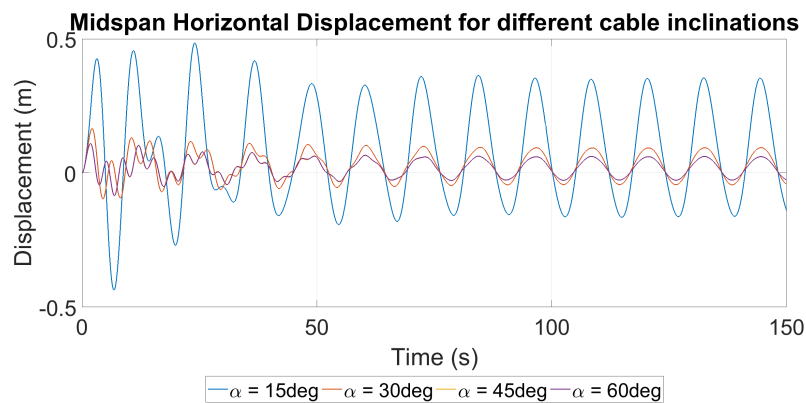


Figure 6.6: Displacement Envelope for $V = V_{cr}$

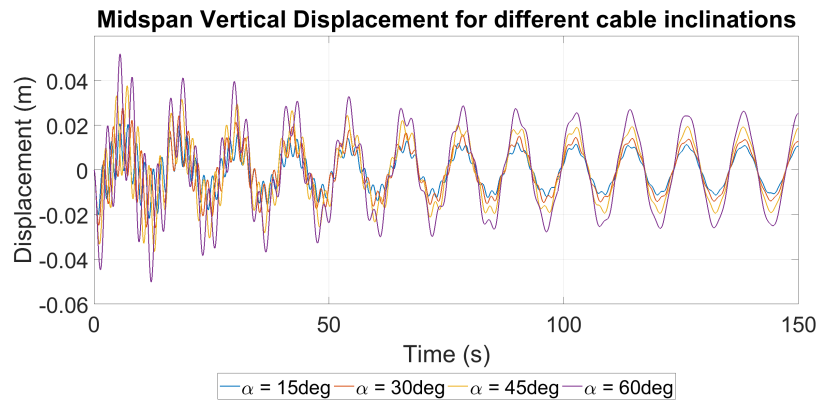
However, the obtained results are in contrast with the findings in Dimitrovová and Rodrigues [6], where the author states that the critical velocity obtained on a finite beam is an upper bound of the critical velocity of the corresponding infinite beam. In the current study it has been found that the expression (6.3) predicts a velocity which is 30% higher than the corresponding simulation. It has also been observed that the maximum displacement occurs close to the right support and develops after the vehicle leaves the structure, see Figure 6.6. The presence of the support alters the deformed configuration of the beam under the vehicle passage and causes reflecting waves that interact with the propagating waves. This possible wave-propagation interaction is addressed as the reason for the difference in the critical velocity.

6.3. Influence of the Cable Inclination

The study of the influence of the cable inclination is crucial when selecting the most preferable supporting system. Among the loads acting on such structure, waves and currents may dominate the scene. The current study investigates a single configuration of supporting system for the SFT excited by the environmental load and traffic load.



(a) Horizontal Displacement at midspan



(b) Vertical and Displacement at midspan

Figure 6.7: Midspan Response for Different Cable Inclination

Looking at Figure 6.7 it can be first noted the initial transient response of the structure that vanishes after a period of 80s. Focusing on Figure 6.7b, it is noticeable that the inclination of the cables does not affect the vertical response heavily, being the supporting system made of alternating vertical and inclined cables, Figure 5.2. However, Figure 6.7a shows a great dependence of the response on the inclination α , as the environmental loading is composed by waves and currents. For the inclinations of 45° and 60° the

horizontal midspan time-history results to be almost exactly superimposed as the horizontal stiffness gained a really small increase, from $6.57 \times 10^7 \frac{N}{m}$ to $6.97 \times 10^7 \frac{N}{m}$, see Figure 5.3. The current, which is flowing just in the horizontal direction, as already discussed in section 5.5, gives an offset in the global response of the structure due to the constant flow, while the wave gives the oscillatory part of it. It is clear that the horizontal response decreases dramatically, about 75%, from $\alpha = 15^\circ$ to $\alpha = 30^\circ$, Figure 6.8. This drop then stops and the steady-state maximum response stays almost constant for $\alpha = 45^\circ$ and $\alpha = 60^\circ$. The reason for this reduction is to be found in the increased stiffness in the horizontal direction which also cause a shift of the fundamental horizontal natural frequency out of the range of the sea wave frequency, as the latter ones are of the order $0.08Hz - 0.1Hz$, see Table 5.8 and the structural natural frequencies are of the order of $0.3Hz - 2.3Hz$.

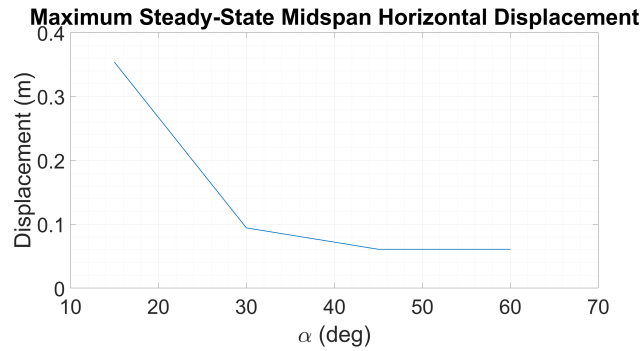


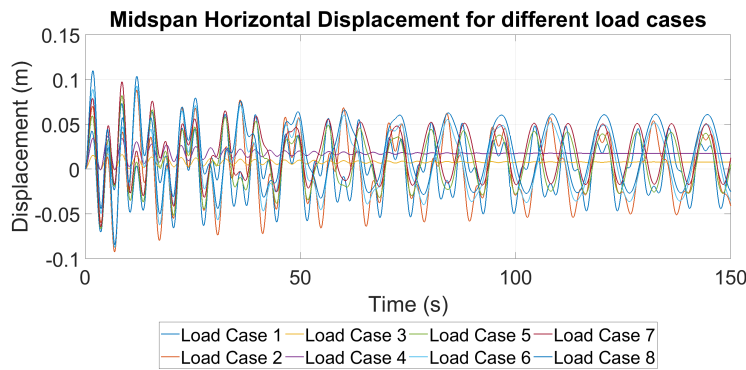
Figure 6.8: Maximum Horizontal Displacement at midspan

6.4. Influence of the Load Case

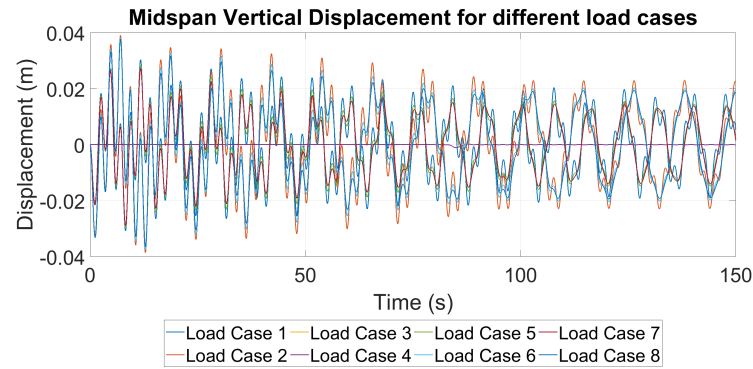
The study of the influence of the environmental load case is important when dealing with the structural integrity as waves and currents appears to dominate the global dynamic response even though the run simulations include both the environmental load and the vehicle passage. The load cases numbered from 1 to 8 represents the combination among the four sea state scenarios and these are:

- Load Case 1 $H_{W,S} = 5m + \text{Train Car}$
- Load Case 2 $H_{W,S} = 4.5m + \text{Train Car}$
- Load Case 3 $V_C = 1 \frac{m}{s} + \text{Train Car}$
- Load Case 4 $V_C = 1.5 \frac{m}{s} + \text{Train Car}$
- Load Case 5 $H_{W,S} = 5m + V_C = 1 \frac{m}{s} + \text{Train Car}$
- Load Case 6 $H_{W,S} = 4.5m + V_C = 1 \frac{m}{s} + \text{Train Car}$
- Load Case 7 $H_{W,S} = 5m + V_C = 1.5 \frac{m}{s} + \text{Train Car}$
- Load Case 8 $H_{W,S} = 4.5m + V_C = 1.5 \frac{m}{s} + \text{Train Car}$

Table 6.1: Environmental Load Case Specification



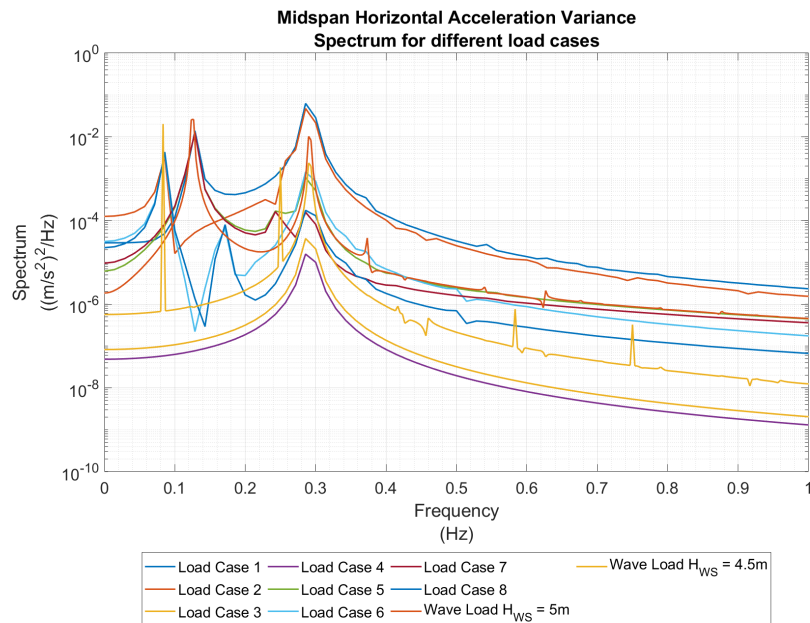
(a) Horizontal Displacement at midspan



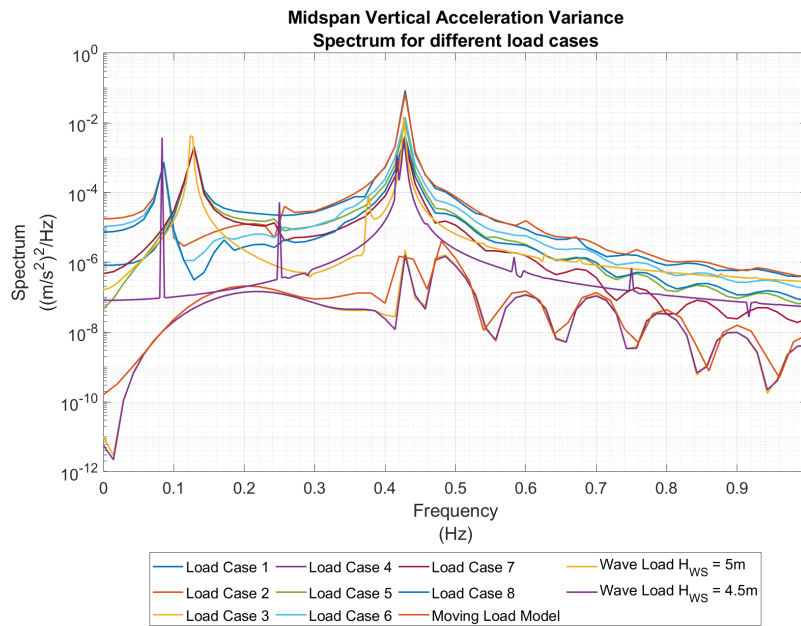
(b) Vertical Displacement at midspan

Figure 6.9: Midspan Response for Different Load Cases

From Figure 6.9b it can be noticed that for load cases 3 and 4, which are the ones associated to the current flow only, the vertical displacement is zero but it becomes non-zero when the vehicle enters the crossing, e.g. $t = 80s$. The global response in the vertical direction appears to be less smooth at steady-state because of the different value of stiffness in the supporting system that alternates every 50m. The account of the combination of both waves and current increase the damping forces in the system as well as external forces. This is due to the non-linear drag force in the Morison's expression of the FSI which accounts for the differential displacement between the fluid and the structure. An analogous behaviour is observed also in the horizontal direction, see Figure 6.9a. For both degrees of freedom the response is dominated by the fundamental modal shape and this is confirmed by the variance spectra of the acceleration, see Figure 6.10, in which it is shown the frequency content of the energy once the structure has reached steady-state response, e.g. $t > 80s$. The moving train car also enters the crossing after the transient response has fade out. In particular, Figure 6.10a presents the variance spectrum of the horizontal accelerations at midspan cross-section for the eight load cases, as in Table 6.1, and also for the two wave conditions alone. Similarly, Figure 6.10b shows the vertical accelerations power spectrum but in this direction it is also included the load case when the vehicle is passing in steady-still water.



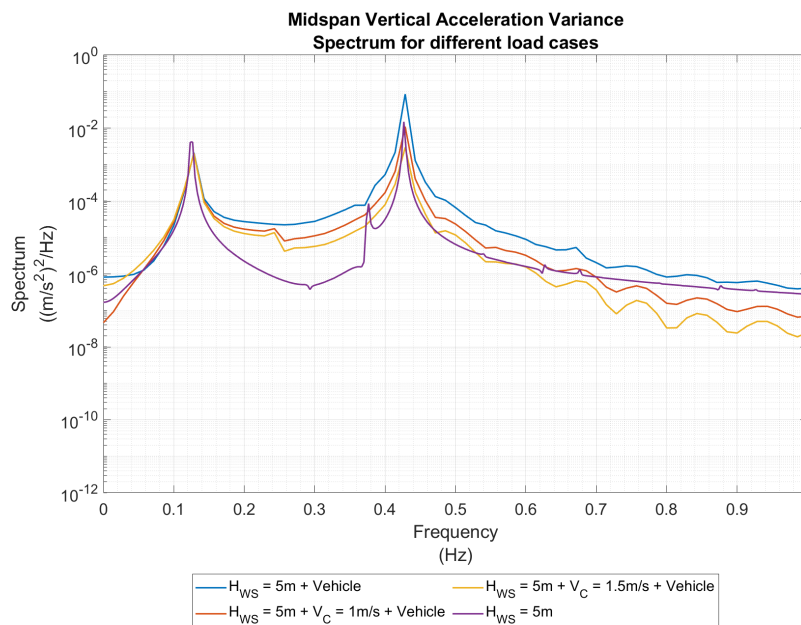
(a) Variance Spectrum Horizontal Acceleration at midspan



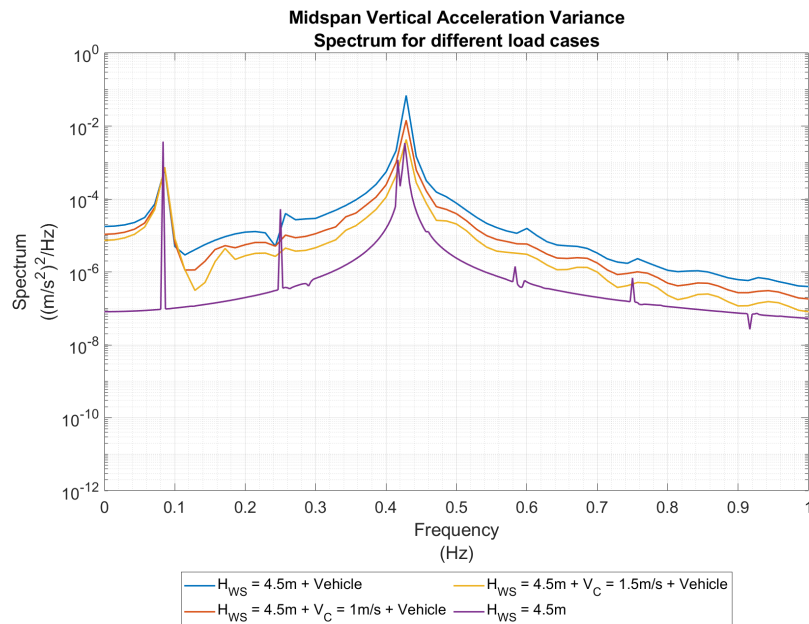
(b) Variance Spectrum Vertical Acceleration at midspan

Figure 6.10: Variance Spectrum of Acceleration at midspan for different load cases

When first looking at the graphs it can be noted that the response when just current flow is considered is dominated by the fundamental modal shape in the sway direction, while more modes are necessary for the heave motion, due to the passage of the vehicle. For a better understanding for the reader, it seems worth displaying the graph of vertical motion in two separate plots, each one regarding a specific wave height, see Figure 6.11.



(a) Midspan Vertical Acceleration Variance Spectrum for $H_{WS} = 5m$



(b) Midspan Vertical Acceleration Variance Spectrum for $H_{WS} = 4.5m$

Figure 6.11: Midspan Vertical Acceleration Variance Spectrum

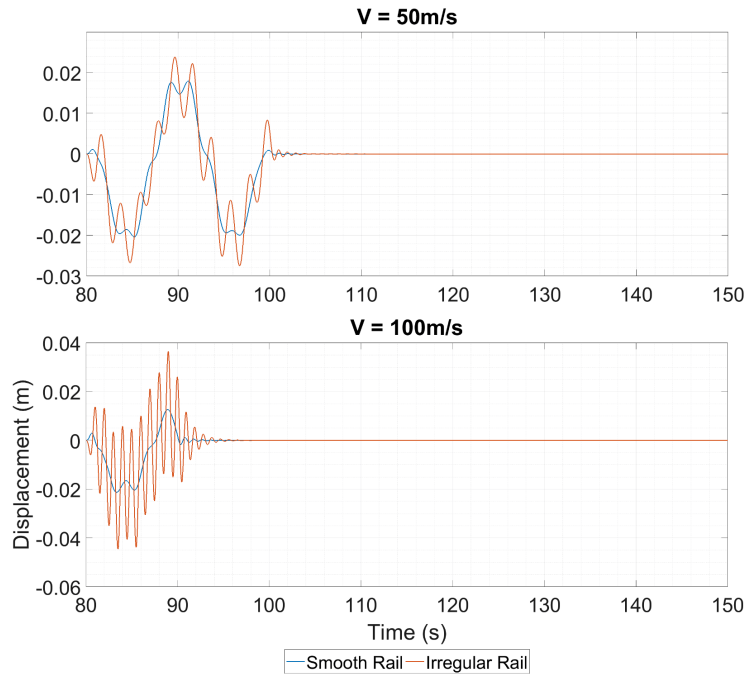
From the graphs in Figure 6.11 it is noted that for the cases of waves only, the system responds at few specific frequencies, i.e. sharper peaks are observed in correspondence of the exciting frequency and the structural natural frequency. When the passage of the vehicle is added to the wave action, the response is very similar for both wave heights in terms of magnitude of the response, but the highest peaks occur in different places, e.g. at the fundamental vertical natural frequency of the tunnel and at the wave frequency, which is different for the two scenarios. Another observation regards the role of the current flow, which induce a bigger reduction of the vibrations for the case of $H_{WS} = 5m$ due to the non-linear damping in the Morison drag force.

6.5. Influence of the Rail Irregularity together with Load Case

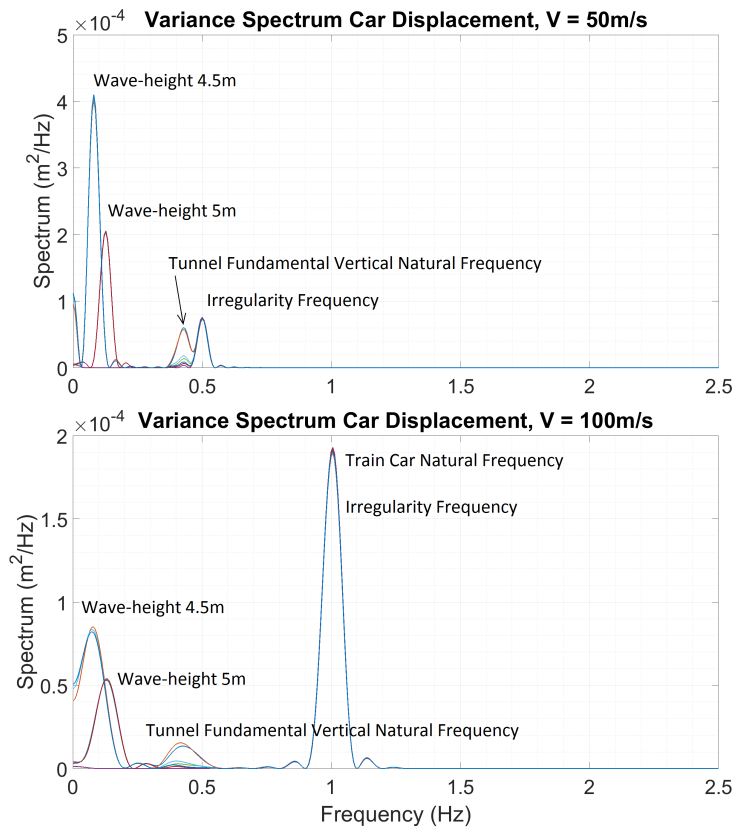
In this section it is proposed the result of the FSVI for an assigned environmental load case for smooth and irregular rail. The aim is to try to determine how track irregularities affect the vehicle response and from that, applying the criteria presented in chapter 3, quantify the Sperling's ride quality and comfort indices. Later it will be varied the wavelength and amplitude of the longitudinal defect of the rail to address also the influence of these two important parameters of the irregularity. For this analysis the adopted values for the amplitude r_0 and wavelength γ_0 of the longitudinal irregularity are:

r_0 (m)	γ_0 (m)
$7 \cdot 10^{-3}$	100

Table 6.2: Amplitude and Wavelength of the Defect



(a) Car Displacement for Smooth and Irregular Rail, Load Case 8



(b) Car Variance Spectrum of Displacement with Irregular Rail

Figure 6.12: Variance Spectrum of Displacement for Different Load Cases

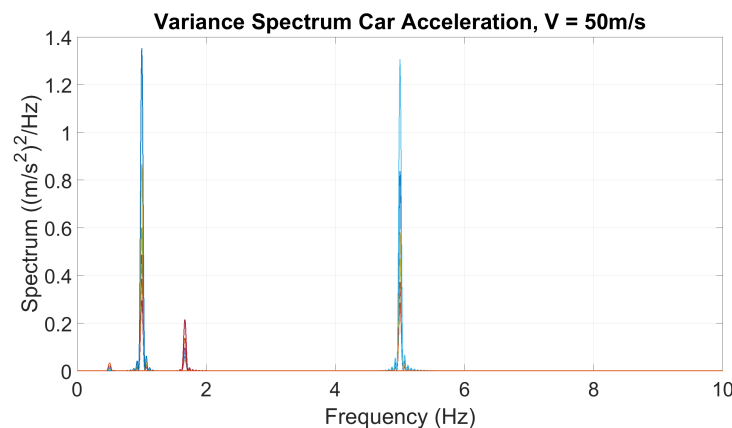
From Figure 6.12a it can be seen that in case the train speed is $50 \frac{m}{s}$ the response of the vehicle can be considered as superposition of the smooth rail plus the irregularity, being the difference between the two time-histories equal to the amplitude r_0 as in Table 6.2. It cannot be said the same when the velocity is higher, e.g. $V = 100 \frac{m}{s}$, for which the difference of the two time-histories appears to be bigger, around $0.02m$, and hence a small amplification is experienced. This argument can be clarified when looking at the displacement spectra, Figure 6.12b, from which is clearly visible that the energy lies in the range of $1Hz$. Figure 6.12b contains not only one specific environmental load case, but all of them. In fact there can be identified the natural frequencies of the two wave states, the tunnel vertical fundamental frequency and the frequency of the irregularity, that can be expressed as:

$$f_0 = \frac{V}{\gamma_0} \quad (6.4)$$

where V is the vehicle velocity. From Figure 6.12b it is also visible that for the train crossing at a constant speed of $50 \frac{m}{s}$ the response is driven by the wave scenarios as expected, meaning that the vehicle follows the low-frequency movements of the structure.

6.6. Influence of the Amplitude and Wavelength of the Rail Irregularity

As anticipated in section 6.5, in this section it will be presented the results of the simulations regarding the influence of the amplitude and wavelength of the rail longitudinal defect, using as input the quantities in Table 5.12. Looking at Table 5.12 it can be noted that in case of design speed of $50 \frac{m}{s}$ it is encountered again the phenomenon of resonance of the train car when the wavelength $\gamma_0 = 50m$, for which the forcing is $1Hz$. From Figure 6.13a it is confirmed that the biggest peak, and hence the majority of the energy, is in correspondence of $1Hz$. As the amplitude of the longitudinal defect increases, the response shows a second peak at a frequency of $5Hz$, which corresponds to a wavelength of the of the irregularity of $\gamma_0 = 10m$. The amplification in the response for this value of frequency can be addressed to the fact that the irregularity shape presents a maximum at the same location where the irregularity shape characterised by $\gamma_0 = 50m$ has a maximum. A similar behaviour is found for the design speed of $100 \frac{m}{s}$. In this case, the peak is smaller because the maximum in the irregularity shape is a little shifted from the maximum of $\gamma_0 = 100m$. For the design speed of $50 \frac{m}{s}$ the other relevant peaks are at $f = 0.5Hz$, $f = 1.67Hz$, which are also referring to longitudinal defect, but of different wavelength such that the forcing frequency results to be still close to the fundamental natural frequency of the train car, or the irregularity shape presents its maximum close to where also $\gamma_0 = 50m$ has a maximum. When the design speed is $100 \frac{m}{s}$ the increase of the irregularity amplitude has a uniform increase in the response along the frequency domain and the unique main peak in the response results to be $f = 1Hz$.



(a) $V = 50 \frac{m}{s}$

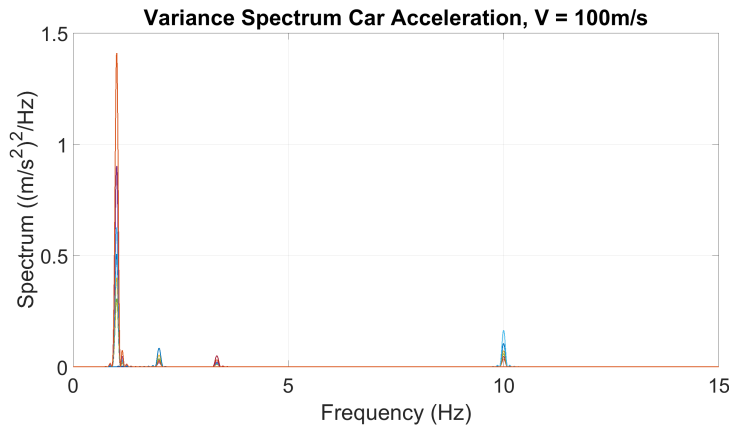
(b) $V = 100 \frac{m}{s}$

Figure 6.13: Variance Spectrum of Train Car Acceleration for Different Defect Amplitude and Wavelength

From Figure 6.14 it can be highlighted that the peaks in the response, located at $f = 1Hz$, correspond to a peak of the W_Z index for ride quality and comfort.

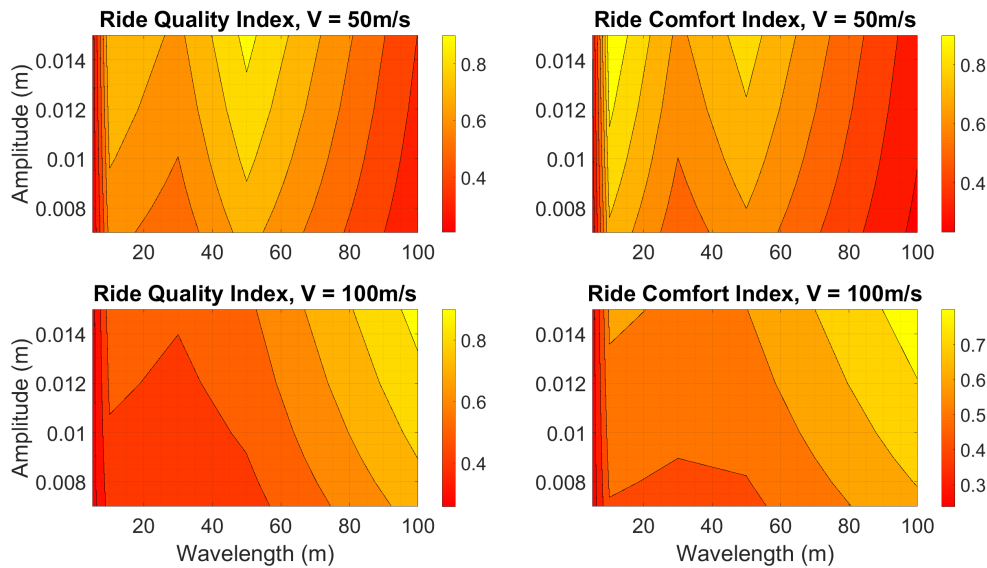


Figure 6.14: Ride Quality and Comfort Index vs. Irregularity Amplitude and Wavelength

6.7. Influence of the Damping of the Suspension Systems

In this section it is offered an insight into the influence of the suspension characteristics on the ride quality and comfort. This study is based on the variation of the damping ratios, which can be expressed as:

$$\zeta_{s1} = \frac{2c_{s1}}{2\sqrt{2k_{s1}m_b}} \quad (6.5a)$$

$$\zeta_{s2} = \frac{2c_{s2}}{2\sqrt{2k_{s2}m_c}} \quad (6.5b)$$

In the simulations, the SFT was subjected to both environmental loading condition and train car passage. The rail irregularity at longitudinal level is also considered, but two different values of the wavelength γ_0 have been used according to the design speed. In particular, these are:

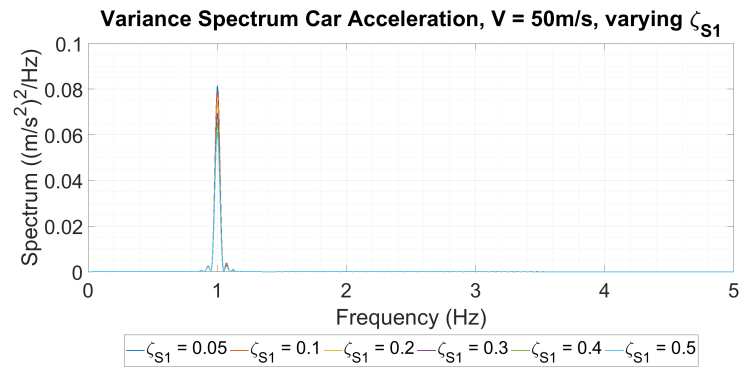
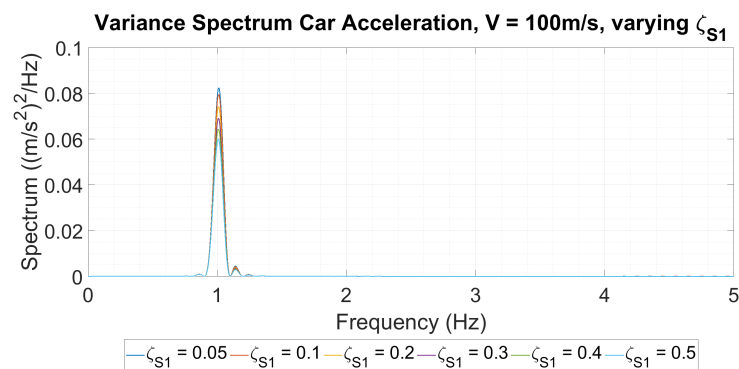
$$\begin{aligned} \gamma_0 &= 50m \quad \text{for } V = 50 \frac{m}{s} \\ \gamma_0 &= 100m \quad \text{for } V = 100 \frac{m}{s} \end{aligned}$$

The values of the damping ratios have been varied according to Table 6.3 below:

ζ_{s1}	ζ_{s2}
0.05	0
0.1	0.05
0.2	0.1
0.3	0.2
0.4	0.3
0.5	0.4
	0.5

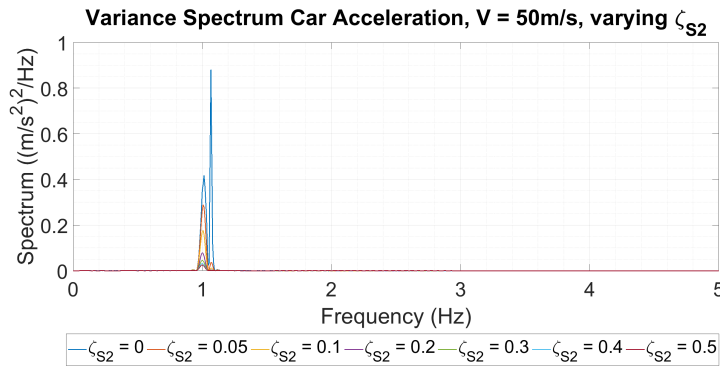
Table 6.3: Damping Ratios Input

In Figure 6.15 the different energy spectra are presented, where each subfigure corresponds to a design speed of the crossing and a specific suspension characteristic. As shown in section 6.6, the wavelength of the rail irregularity has been chosen such to generate amplification in the response due to the closeness of the fundamental natural frequency of the train car with the forcing frequency induced by the longitudinal defect. In case of the variation of the characteristic of the primary suspension system, e.g. the suspension system of the bogies, it is observed that the response of the above train car is not critically affected, thanks to the presence of the secondary suspension system which may dissipate the energy, see Figure 6.15a and Figure 6.15b.

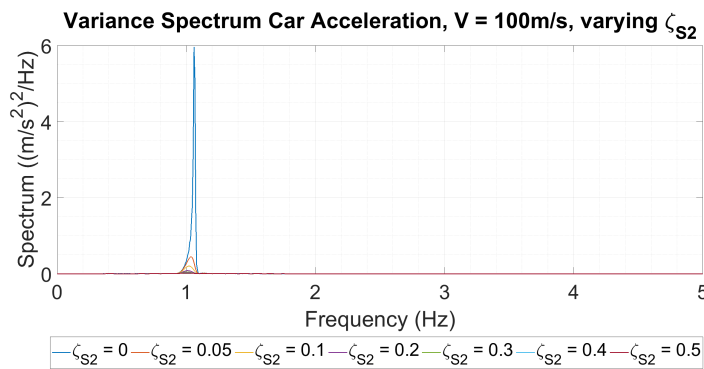
(a) $V = 50 \frac{\text{m}}{\text{s}}$, Variation of ζ_{s1} (b) $V = 100 \frac{\text{m}}{\text{s}}$, Variation of ζ_{s1}

This is not the case when the characteristic of the secondary suspension system are modified. In fact, it can be observed from Figure 6.15c and Figure 6.15d that for small values of damping ratios, the energy of the motion stays in the train car, especially at higher velocity. On the other hand, when the damping ratio is

bigger, the peak in the response shifts from the natural frequency of the train car to 1Hz, meaning that the energy is absorbed by the secondary suspension system.

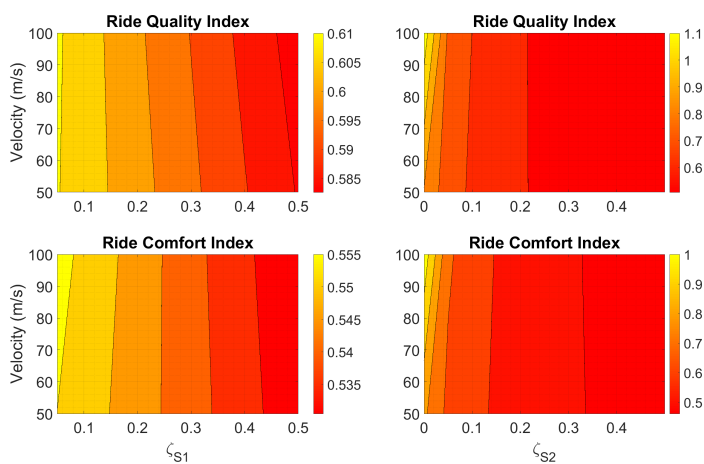


(c) $V = 50 \frac{m}{s}$, Variation of ζ_{s2}



(d) $V = 100 \frac{m}{s}$, Variation of ζ_{s2}

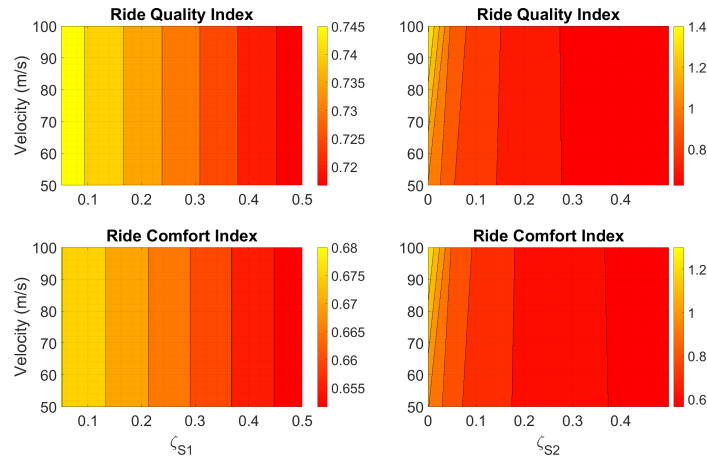
Figure 6.15: Variance Spectrum of Train Car Acceleration for Different Suspension Characteristics



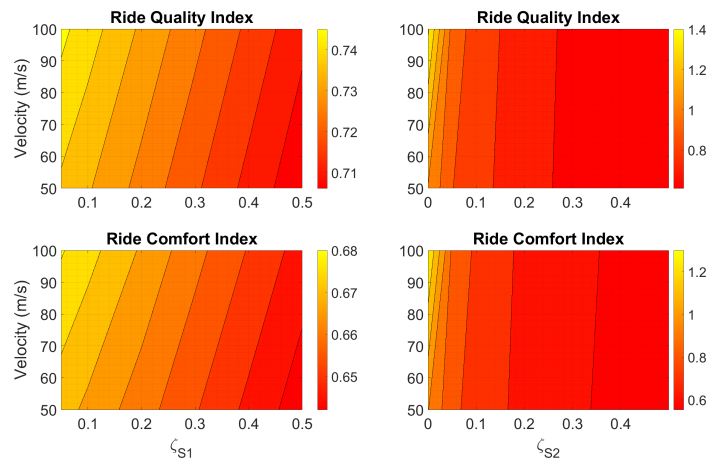
(a) Carbody Centre

When evaluating the ride quality and ride comfort indices it might be interesting focusing not only at the response at the centre of the train car but also at the two extremes of it, i.e. above the front and rear

bogies. The influence of the primary and secondary suspension damping on the ride quality and comfort indices is depicted in Figure 6.16, considering ζ_{s1} ranging between 0.05 and 0.5, while ζ_{s2} from 0 upto 0.5. A regular reduction of the ride quality index, associated with an overall higher comfort class, is observed with the increase of the primary suspension damping. Although, it is not a substantial decrease and a reason for that can be found in bogie mass whose inertia reduces the damping capacity of the suspension, as it has already been observed in Dumitriu M. et al (2015). The influence of the increase of the secondary suspension damping is worth mentioning since an increase of 10 times the damping from 0.05 to 0.5 generates a reduction of the ride quality and ride comfort indices of around 50%.



(b) Above Front Bogie



(c) Above Rear Bogie

Figure 6.16: Influence of the primary and secondary suspension damping

6.8. Influence of the Whole Train

A conclusive comparison is made between the whole train model that, in the current study, is composed of eight cars for a total length of 200m, and a single wagon train. The choice of the number of cars in the train has been driven by real train used in the industry, such as the Korean KTX and the Italian ETR1000 high speed trains, which both are made of 8 train cars. With this model the aim is to understand if different level of comfort/discomfort is experienced by the passengers inside the different train cars. To study the FSVI it is again proposed the power spectrum of the acceleration of the centre of the train car.

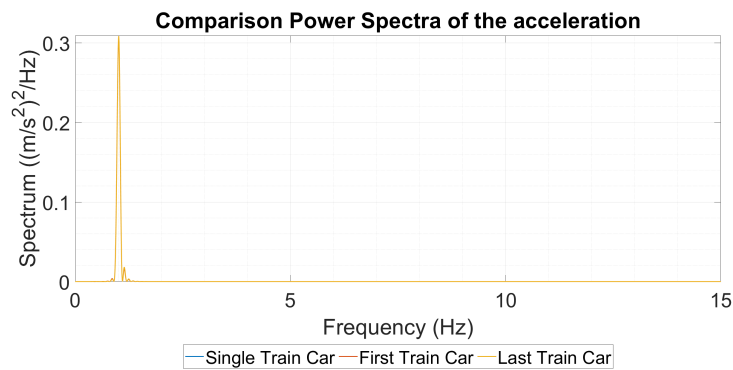


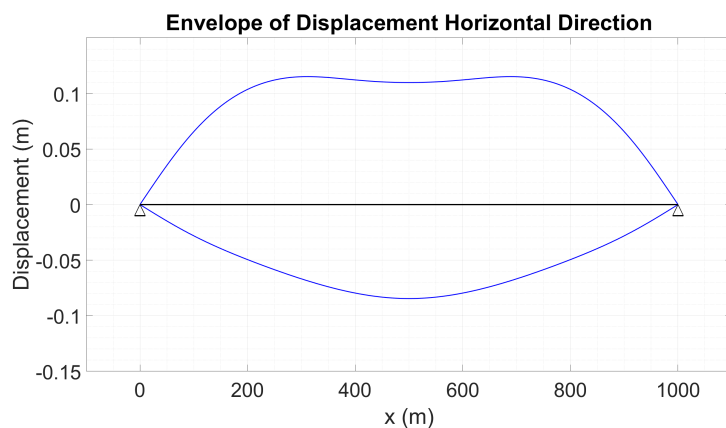
Figure 6.17: Comparison Power Spectra of the Acceleration between Single and Full Train

Figure 6.17 shows the power spectrum of the carbody's centre acceleration of a single train car passing the tunnel and the first and last train cars respectively for the model with the full vehicle. From the amplitude spectra of the acceleration it is possible then to quantify the Sperling's ride quality and comfort indices. Table 6.4 summarise the values of the indices for the different models:

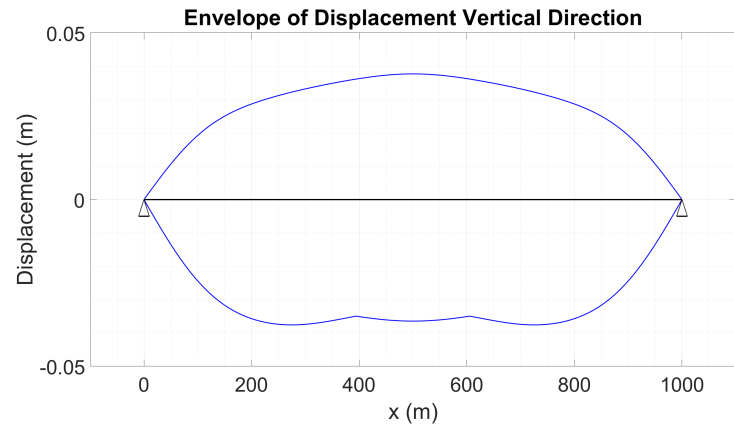
Model	Ride Quality Index	Ride Comfort Index
Single Train Car	0.7436	0.6780
First Train Car	0.7435	0.6779
Last Train Car	0.7445	0.6789

Table 6.4: Sperling's Ride Quality and Comfort Indices

The envelopes of the dynamic displacement and the bending moment in both sway and heave direction is chosen as a method of comparison between the global structural response of the two simulated models and these are reported below. From Figure 6.18 it is possible to see that the envelope of the two simulations are perfectly overlapped. This shows that the structural dynamic response is not much affected by the vehicle passage, as the driving force for the steady-state response of the structure is the wave.



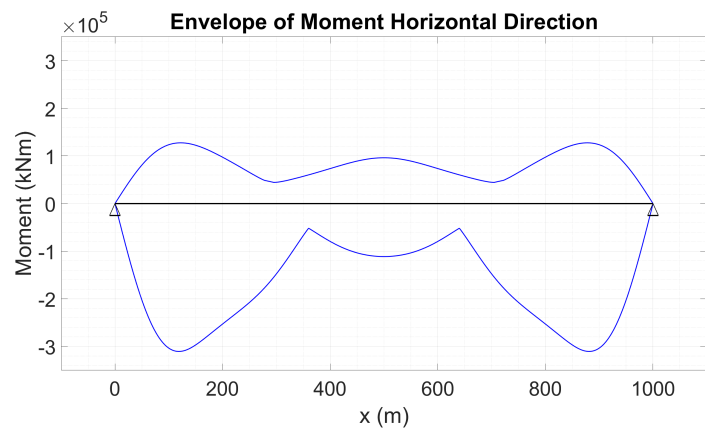
(a) Sway Direction. Single train car model in red line, whole train model in blue line.



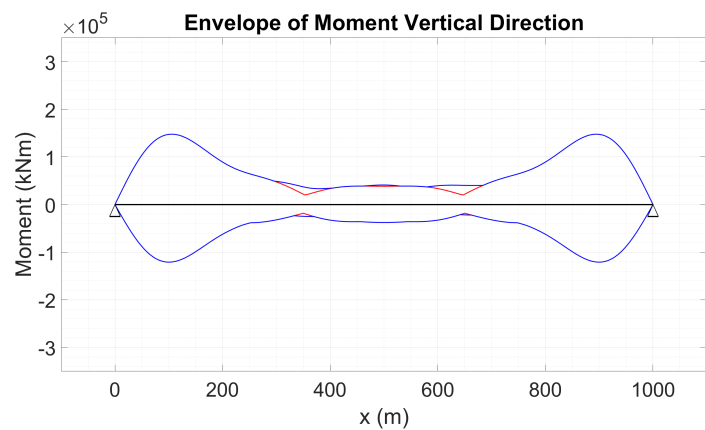
(b) Heave Direction. Single train car model in red line, whole train model in blue line.

Figure 6.18: Displacement Envelope

The envelope of the bending moments in the vertical direction, see Figure 6.19b, shows that in the central part of the crossing the model with the whole train has higher moment. Figure 6.18b shows that the negative displacements are almost constant along the central part of the tunnel, meaning that the curvature in that region is small. The difference in the inertial load between the two vehicle models, then appears to play an important role in the definition of the local stresses in the structure, as a small increase in the curvature due to increased mass of the whole train causes higher moments.



(a) Sway Direction. Single train car model in red line, whole train model in blue line.



(b) Heave Direction. Single train car model in red line, whole train model in blue line.

Figure 6.19: Moment Envelope

6.9. Concluding remarks

Some concluding observation can be done after the presentation of the run simulations. The dynamic structural behaviour is governed by the waves scenarios, as the traffic loading contributes for a very small percentage to the total response and it is also a transient loading, while the waves define the steady-state response of the structure. The presence of a longitudinal defect in the railway causes amplification in the vehicle response. The biggest amplification occurs when the wavelength of the unevenness has the same magnitude as the design speed of the train. The damping characteristics of the suspension systems also influence the amount of vibration transmitted to the train car. For standard values of damping, as shown in Table 5.10, the system can absorb the majority of the energy and the comfort in the train car is ensured.

7

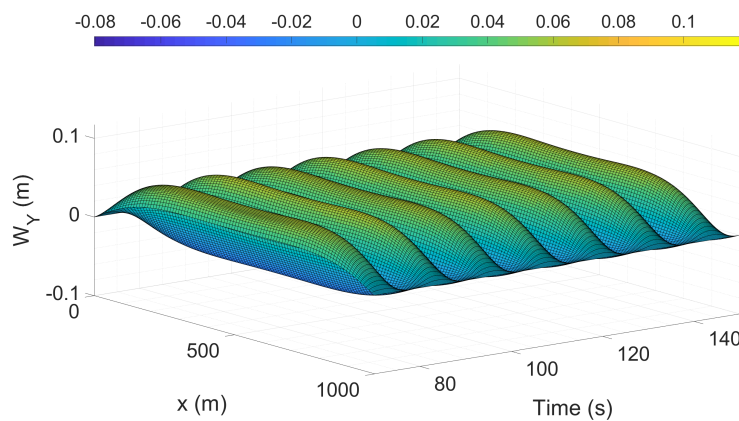
Discussion of Results

7.1. Introduction

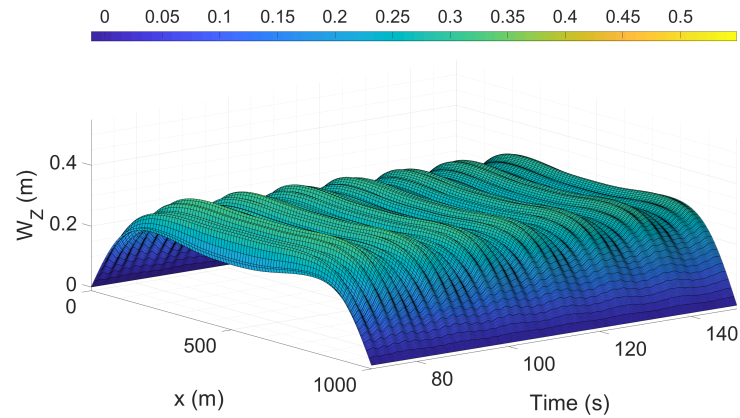
In this chapter it is proposed the discussion of the results presented in chapter 6 with the evaluation of serviceability limit state of the structure and the motion sickness, the comfort/discomfort does not appears to be governing.

7.2. Structural Behaviour

The SFT supported by tensile cables in configuration as shown in Figure 5.2 is used for the analysis. The structure is loaded by time-dependent forces and hence a time-history of the global response seems the best mean for understanding the structural behaviour. In Figure 7.1 and Figure 7.2 the development of the displacement and bending moment along the tunnel length in the time are showed.

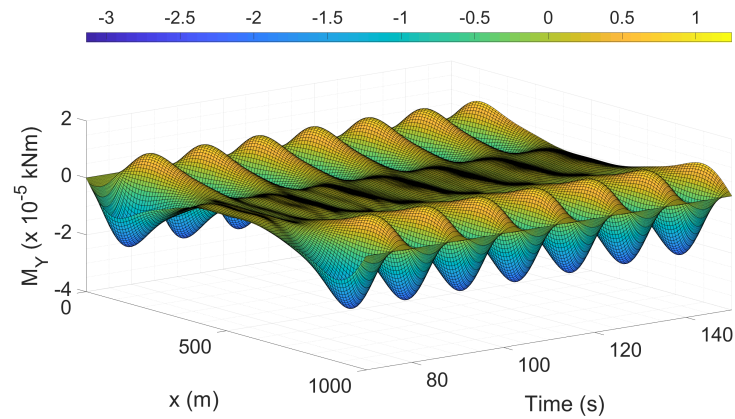


(a) Horizontal Displacement, Load Case 8

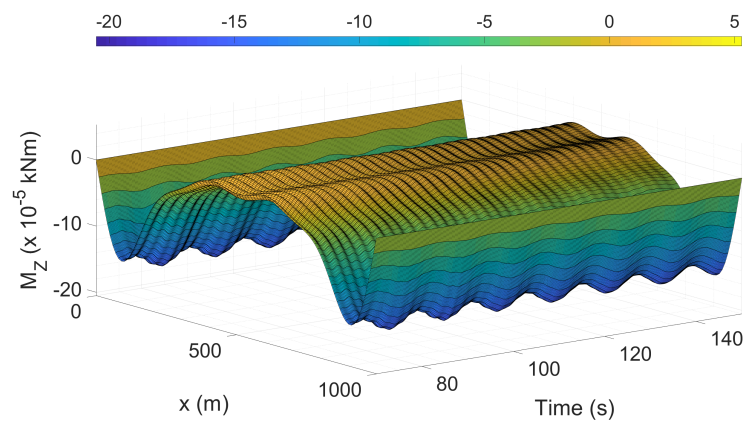


(b) Vertical Displacement, Load Case 8

Figure 7.1: Hydrodynamic displacements along the length of the SFT with time



(a) Horizontal Moment, Load Case 8



(b) Vertical Moment, Load Case 8

Figure 7.2: Hydrodynamic bending moments along the length of the SFT with time, Load Case 8

Figure 7.1 depicts the displacement, in both horizontal and vertical planes, along the whole crossing distance against the time. Figure 7.1a shows that the response is driven by the harmonic regular wave loading and the SFT oscillates in both positive and negative direction. Figure 7.1b presents the equivalent harmonic motion of the tunnel, due to the kinematic of the water particles, but only on one side of the vertical axis, as the structure is loaded by the permanent upwards residual buoyancy. This reflects the condition of the cable

being in constant tension avoiding the occurrence of slacking. Together with the small oscillations, which are caused by the initial transient response due to the sudden application of the buoyancy force, it is possible to see the slower vibration due to the wave force, which in this specific case has a period of $T_W = 12s$. The configuration adopted for the supporting system cannot be clearly distinguished when looking at Figure 7.2, as the non-dimensional parameter K_v , as defined in (4.7), results to be smaller than 0.05 making the elastic supports equivalent to an elastic foundation. Although, the overall shape of the moment distribution in the horizontal and vertical planes are equivalent, where the main difference lies in the oscillating change of sign of the moment close to the supports in the horizontal plane due to the vibrations. Regarding the ride safety and comfort during the storm conditions, deflection and vibration control criteria need to be used to guarantee the serviceability. As presented in subsection 1.2.4 the Norwegian government has advised the limiting values reported in Table 1.1. With a spacing of 50m of the vertical supporting system the maximum allowable displacement is 0.14m. Looking at Figure 7.1b it can be noticed that with the current design choices this criteria might not be met at sections close to the supports, while the differential displacement in the central part of the crossing does not vary much, meaning that the criteria is met.

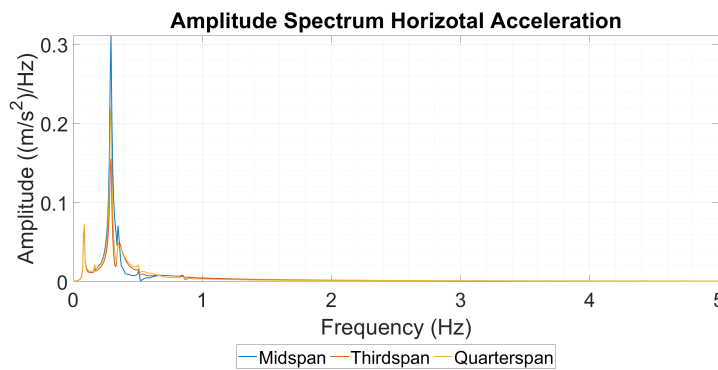
Regarding the displacement in the horizontal plane, it is relevant to mention that the dimension of the structural elements provide the required stiffness. In fact the requirement is always met, as the maximum displacement is around 0.1m, while the maximum allowable displacement is fixed to an amount of 0.5m, as the inter-axis between the inclined cable which provide the main external stiffness is 100m. Lwin [26] treated the deflection and motion problem with the regard of the floating bridges. The author proposed some boundary values for deflection and motion for normal storm (1-year storm) conditions which may be used as guidelines. In the presented work the environmental conditions refer to a 100-year storm condition, so possible failures in meeting the imposed limits are not so reliable. The limit values are reported here below:

Loading Condition	Type of Deflection or Motion	Maximum Deflection	Maximum Motion
Vehicular Load	Vertical	$\frac{L}{800}$	
	Vertical (heave)	$\pm 0.3m$	$0.5 \frac{m}{s^2}$
Wave	Lateral (sway)	$\pm 0.3m$	$0.5 \frac{m}{s^2}$
	Rotation (roll)	$\pm 0.5^\circ$	$0.05 \frac{rad}{s^2}$

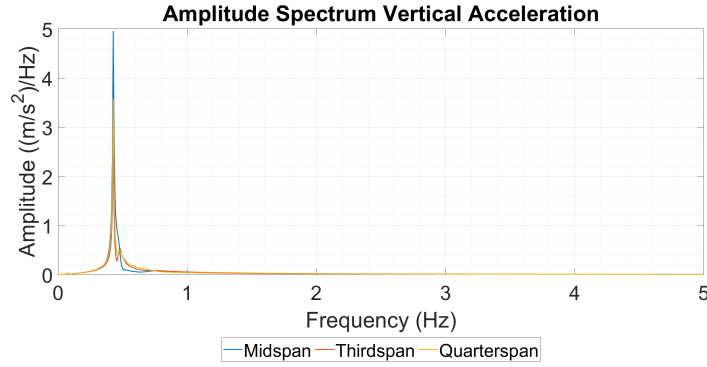
Table 7.1: Deflection and Motion Limits. Table taken from Lwin [26]

where L represents the bridge span.

The maximum deflection allowed presented in Lwin M.M. (2000), which is fixed to $\pm 0.3m$ is verified for the presented case study, for which sway vibrations oscillate around $\pm 0.1m$, while heave vibrations around $0.1m - 0.3m$



(a) Steady-State Horizontal Acceleration Amplitude Spectrum



(b) Steady-State Vertical Acceleration Amplitude Spectrum

Figure 7.3: Comparison Steady-State Acceleration Amplitude Spectra at different locations

When looking at the structural acceleration responses in Figure 7.3 it can be noticed that the amplitude of the sway motion is smaller than the suggested value in Table 7.1. For heave motion the amplitude appears to be ten times bigger than the boundary value in Table 7.1, but the reason for that lies in the numerical solution as the buoyancy force is applied as a step-load, which generates big amplitude noise that slowly fades away and lead the the structure to the static deflection due to residual buoyancy. A second consideration that needs to be addressed is valid for both sway and heave motions. The amplitude spectra in Figure 7.3 have been evaluated at three specific location, which corresponds to the maximum in the first three mode shapes, see Figure 4.8. Despite this, it is noticed that the fundamental mode shape is driving the deformed shape of the SFT not matter the location of the focus.

7.3. Motion Sickness

When looking at the structural response, one might recognize that the excited frequency range lies outside the interval of interest regarding the human whole body vibration, but falls in the interval characterised by the motion sickness. Lawther A. and Griffin M.J. studied deeply this topic and are reference when discussing this topic. Aykent et al. [1] evaluated the motion sickness through the Motion Sickness Dose Value (MSDV), which can be defined as:

$$MSDV_Z = \left[\int_0^t a_{zRMS}^2(t) dt \right]^{0.5} \quad (7.1)$$

where a_{zRMS} is the Root Mean Square (RMS) of the vertical acceleration and it can be obtained with:

$$a_{zRMS} = \sqrt{(k_z w_d a_z(t))^2} \quad (7.2)$$

and where $k_z = 1$ and $w_d = 0.067$ are the weighting coefficients to obtain the frequency-weighted RMS acceleration. Based on the MSDV, two parameters can be defined: the Vomiting Incidence (VI) and the Illness Rating (IR), which are expressed as a percentage of the MSDV through the formulas:

$$VI = \frac{1}{3} MSDV_Z \quad (7.3a)$$

$$IR = \frac{1}{50} MSDV_Z \quad (7.3b)$$

The resulting value of IR is then compared to a rank which is divided in four main intervals:

IR	Corresponding Feeling
0	I felt all right
1	I felt slightly unwell
2	I felt quite ill
3	I felt absolutely dreadful

Table 7.2: Illness Rating Rank. Table taken from Aykent et al. (2014)

Such method has been applied to all the different loading scenarios and the results are summarised here below:

Load Case	IR
$H_w = 5m + \text{Vehicle}$	0.014
$H_w = 4.5 + \text{Vehicle}$	0.013
$V_c = 1 \frac{m}{s} + \text{Vehicle}$	0.012
$V_c = 1.5 \frac{m}{s} + \text{Vehicle}$	0.010
$H_w = 5m + V_c = 1 \frac{m}{s} + \text{Vehicle}$	0.011
$H_w = 5m + V_c = 1.5 \frac{m}{s} + \text{Vehicle}$	0.010
$H_w = 4.5m + V_c = 1 \frac{m}{s} + \text{Vehicle}$	0.010
$H_w = 4.5m + V_c = 1.5 \frac{m}{s} + \text{Vehicle}$	0.010

Table 7.3: Illness Rating Results

Looking at the results it can be noticed that the expected feeling of passengers, while passing through the crossing in any of the considered sea states, is a non-disturbing condition.

7.4. Comfort and Exposure Limit

It also has to be mentioned that the amount of time required to cross the SFT is between 10s – 20s depending on the design speed. The Standard ISO 2631 (1980) covers the effect of vibrations in the range of 1Hz – 80Hz providing the exposure limit at the acceleration magnitudes, see Figure 7.4.

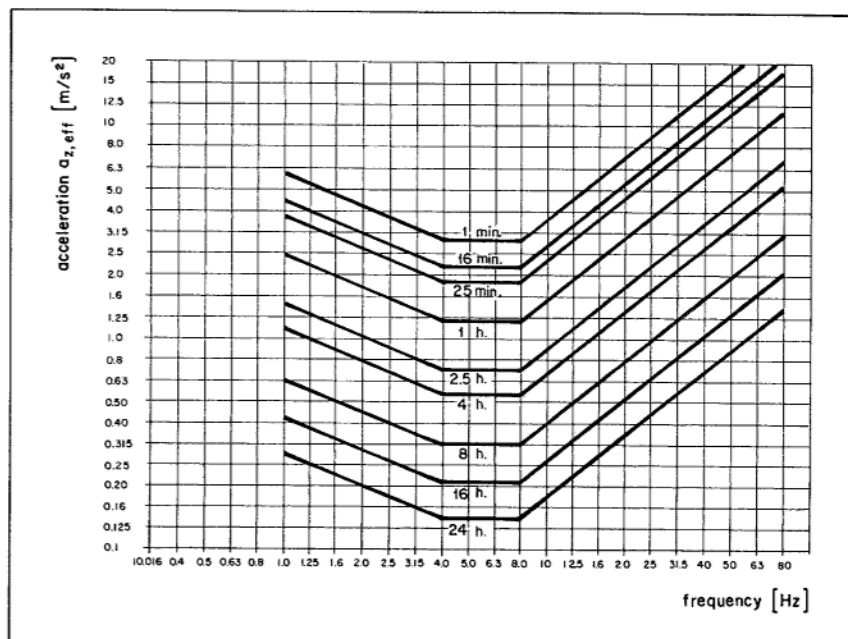


Figure 7.4: Standard ISO 2631 (1980) Bounds Vertical Acceleration

When relating the results of section 6.7 with the Standard ISO 2631 (1980) it is found that the exposure limit is minimum 1hr as the maximum amplitude, which correspond to a frequency of 1Hz, reaches the value of $2.5 \frac{m}{s}$. Comparing this exposure limit with the aforementioned time of load passage, it is observed that can be provided comfort to passengers. In the different simulations that have been performed in the current study it is found that the presence of the rail irregularity affect the response of the vehicle and the passengers inside it, see Figure 6.13. Both the wavelength γ_0 and the amplitude r_0 of the longitudinal defect play a relevant role in it: the first parameters influence the excitation frequency and hence, the possibility of resonance when approaching one of the frequencies of the vehicle masses; the latter one generating higher forces contact forces and acceleration in the vehicle components. The highest peak of the amplitude reaches the value of

$1.2 \frac{m}{s}$ and the resulting ride quality and comfort indices are pretty low, i.e. lower than one, meaning that the passengers don't feel discomfort while crossing the SFT. In fact, as described in chapter 3, the lower the Sperling's index W_Z is, the better conditions it represents.

A second key parameter for addressing the comfort level in the train carbody is represented by the mechanical characteristic of the suspension system. In section 6.7 it has been studied the influence of different damping of the suspension systems and it has been observed that the carbody response is strongly affected when the secondary suspension damping is varied. When the primary suspension is varied, most of the energy of the system is stored in the contact forces between the wheel and the bogies, as the excited frequency is $f = 1 Hz$, which corresponds to the forcing frequency. In the other case, when the secondary suspensions damping is modified, it can be noticed that for low value of the damping ratio, e.g. $\zeta_{s2} \in [0 - 0.05]$, the energy is stored in the carbody mass, see Figure 6.15, as the excited frequency it appears to be the natural frequency of the train car, $f = 1.065 Hz$.

8

Conclusions and Recommendations

8.1. Conclusions

The current study has presented the dynamic FSVI as part of the 4-year research plan that has been signed by the China Communications Construction Co., Ltd. (CCCC), the Dutch Tunnel Engineering Consultants (TEC) and the Delft University of Technology. The scope is to study the feasibility of a SFT to connect the Leizhou Peninsula, south China, to Hainan Island. The Hainan Strait is characterised by an average width of 30km and a maximum depth of 120m . The tunnel is assumed to be designed of prefabricated cylindrical tunnel segment connected in-situ by watertight joints and placed at a depth of 30m below sea surface.

An internal diameter of $D_i = 15.5\text{m}$ is chosen in order to be able to accommodate two railway tracks. The supporting system is chosen to be made of alternating vertical and inclined pretensioned cables, where the latter are attached to the tunnel under a 45° angle. The centre-to-centre distance between the two respective cable sets is 100m and hence, a support is provided every 50m .

The residual upwards buoyancy causes a global vertical displacement which reaches a maximum of 0.26m and the orbital movement of the water particles due to wave let this deflection oscillate of $\pm 0.05\text{m}$ around this static displacement. The horizontal direction is affected by the sea currents, which assume value of $V_C = 1.0\frac{\text{m}}{\text{s}} - 1.5\frac{\text{m}}{\text{s}}$, and by the horizontal component of the orbital velocity of the water particles. The deflection for sway motion appears to oscillate in the interval $\pm 0.1\text{m}$.

Based on these environmental conditions, a dynamic interaction analysis with different train models is carried out to determine the influence of the several input parameters to the ride quality and comfort. The tunnel is modelled as a Euler-Bernoulli beam with hinged boundary conditions at both ends. The presence of the water is accounted for by defining the added mass and the relative motion between fluid and structure in the Morison's expression. The cables are modelled as linear springs and these can be inclined of 45° or vertical. The train is assumed to run at a constant velocity of $50\frac{\text{m}}{\text{s}}$ or $100\frac{\text{m}}{\text{s}}$ and it is modelled in different ways, i.e. moving load, moving mass and train car, depending on the purpose of the simulation.

The dynamic FSVI problem is addressed with the PDE regarding the dynamic bending vibration of the beam, the definition of contact forces and the dynamic equations of the vehicle masses. By performing the modal expansion on the tunnel vibrations, a system of ODEs in the modal coordinates and mass displacements can be obtained. This global system of equations can be solved in the time domain using the solver ode45 already present in the MATLAB[®] suite, which can handle non-linear problems.

For both design speeds, the global structural response is not affected by the different vehicle models used to describe the traffic loading. Moreover, when it is account for the actual presence of the water around the tunnel, the influence of the train passage becomes negligible, as the design speeds appears to be lower than the critical velocity, $V = 300\frac{\text{m}}{\text{s}}$, that may cause higher displacement of the structure. The inclination of the cables appears to affect especially the sway motion, as the heave motion can count on the presence of the additional alternating vertical cables, whose horizontal restraining capacity is really small compared to the inclined ones. Hence, the 45° inclination is adopted because no remarkable improvements in the structural horizontal response are observed for higher inclinations.

The presence of the longitudinal unevenness of the railway plays a role only in the vehicle response, as it generate an additional force to the vehicle. The resonance can be reached for particular values of the irregularity wavelength, $\gamma_0 = 50, 100\text{m}$, being the fundamental natural frequency of the train car of the same order,

$f_0 = 1Hz$. Despite the occurrence of resonance, a good level of comfort is predicted while crossing the tunnel since the simulated sea states exert really low energy on the frequencies that characterise the system as it has been presented through the wave spectrum analysis. Both the waves and the lowest order modal shapes, which govern the structural response, are characterised by low frequencies which are lower than the limit of human perception, i.e. $f < 0.5Hz$. The obtained small vehicle-structure-interaction is valid also when the entire train made of eight cars is implemented. In fact, the difference between the ride quality and comfort indices of the single car and the multiple cars models is negligible, i.e. ride quality index 0.7436 against 0.7445 and ride comfort index 0.6780 against 0.6789.

The low-frequency dominated response may be the cause of motion sickness rather than discomfort. Despite this, the limited amplitude of the structural and vehicle accelerations does not raise warnings of illness while crossing the SFT.

8.2. Recommendations

There are several points that may be analysed in further work and these can be distinguished in two main categories. The first category covers improvement applied to the structural model to make it more realistic. The second category may include the same model of the current work, but applying different load conditions.

Structural model improvements:

- Actual length of the crossing: the tunnel has been modelled with a reduced length to make the computational time in line with the complexity of the problem. Improvements in the code may help in speeding up the computational time allowing for the analysis with the actual crossing length. The natural frequencies of the structure will reduce with the increase of the length of the system and so, the environmental conditions might be characterised by the same range of frequencies.
- Boundary conditions and modal shapes: as most of the deflection appears to occur at the edge of the tunnel giving free rotation, the use of fixed boundary conditions may control the rotation at the supports, but increase the stresses at boundary cross-sections. Also the use of different modal shapes is required when changing boundary conditions.
- Use of 3D finite element modelling to account for more complex analyses as well as for three-dimensional vehicle modelling to study the horizontal vibrations inside the train car, which was not possible to be accounted for with the 6DOFs systems.

Following Analyses:

- Irregular wave analysis: it would be interesting to have a complete irregular wave analysis to compare with the results obtained with the regular wave model implemented, which is based on the significant wave height and peak period.
- More train passing: it would be interesting to model more trains crossing the tunnel not only one after the other, but also in the two different travelling directions. This may cause higher deflections of the structure as well as higher accelerations due to the arriving and leaving of several vehicles, which may cause discomfort increments.
- Higher frequency waves: it seems interesting to investigate those sea states characterised by a higher frequency content in order to fall in the same range of the system natural frequencies. The use of the diffraction hydrodynamic theory will be then necessary as the structure will become a large structure with respect to the wavelength of the sea state.

Bibliography

- B. Aykent, F. Merienne, C. Guillet, D. Paillot, and A. Kemeny. Motion sickness evaluation and comparison for a static driving simulator and a dynamic driving simulator. *Proceedings of the Institution of Mechanical Engineers, Part D: Journal of Automobile Engineering*, 228(7):818–829, 2014. doi: 10.1177/0954407013516101.
- F. Brancaleoni, A. Castellani, and P. d’Asdia. The response of submerged tunnels to their environment. *Engineering Structures*, 11(1):47–56, 1989. doi: [https://doi.org/10.1016/0141-0296\(89\)90032-1](https://doi.org/10.1016/0141-0296(89)90032-1).
- R. Bruschi, G. Chiesa, and M. R. Olocco. Reliability analysis for submerged buoyant anchored tunnels: applications to the feasibility study for the fixed link across the strait of messina. *Strait Crossings*, 1990.
- I. I-Yoon Choi, Ju-Hwan Um, Jun S. Lee, and Hyun-Ho Choi. The influence of track irregularities on the running behavior of high-speed trains. *Proceedings of the Institution of Mechanical Engineers, Part F: Journal of rail and rapid transit*, 227(1):94–102, 2013. doi: 10.1177/0954409712455146.
- R. W. Clough and J. Penzien. *Dynamics of structures*. Computers & Structures, Inc, third edition, 2003.
- Z. Dimitrovová and A. F. S. Rodrigues. Critical velocity of a uniformly moving load. *Advances in Engineering Software*, 50:44–56, 2012.
- DNV. *Modelling and analysis of marine operations*. Det Norske Veritas, 2014.
- M. Dumitriu. Evaluation of the comfort index in railway vehicles depending on the vertical suspension features. *Annals of the Faculty of Engineering Hunedoara*, 11(4):23, 2013. ISSN 1584-2673.
- M. Dumitriu and M. A. Gheti. Evaluation of the ride quality and ride comfort in railway vehicles based on the index wz. *Annals of the Faculty of Engineering Hunedoara-International Journal of Engineering*, 13(3), 2015. ISSN 1584-2673.
- M. Dumitriu and M. Leu. Correlation between ride comfort index and sperling’s index for evaluation ride comfort in railway vehicles. 880:201–206, 2018. doi: <https://doi.org/10.4028/www.scientific.net/AMM.880.201>.
- FEHRL. Analysis of the submerged floating tunnel concept. Technical report, FEHRL (Forum of European National Highway Research Laboratories), 1996.
- A. Fjeld, T. H. Søreide, and S. A. Haugerud. Feasibility study for crossing the sognefjord submerged floating tunnel. Technical report, 2012.
- L. Fryba. *Vibration of solids and structures under moving loads*, volume 1. Springer Science & Business Media, 1972. doi: 10.1007/978-94-011-9685-7.
- K. F. Graff. *Wave motion in elastic solids*. Courier Corporation, 1975.
- W. C. Grantz. Steel-shell immersed tunnels—forty years of experience. *Tunnelling and Underground Space Technology*, 12(1):23–31, 1997. doi: [https://doi.org/10.1016/S0886-7798\(96\)00063-6](https://doi.org/10.1016/S0886-7798(96)00063-6).
- B. Jiang and B. Liang. Study on the main influence factors of traffic loads in dynamic response of submerged floating tunnels. *Procedia engineering*, 166:171–179, 2016. doi: <https://doi.org/10.1016/j.proeng.2016.11.580>.
- C. Jin and M. Kim. Dynamic responses of a moored submerged floating tunnel under moving loads and wave excitations. June 2018.
- J. M. J. Journée and W. W. Massie. *Lecture notes*, chapter 12, pages 453–482. TU Delft.

- S. Kanie. Feasibility studies on various SFT in japan and their technological evaluation. *Procedia Engineering*, 4:13–20, 2010. doi: 10.1016/j.proeng.2010.08.004.
- M. H. Kolstein. CIE5128 fibre reinforced polymer (FRP) structures. 2008.
- H. E. Krogstad and Ø. A. Arntsen. Linear wave theory - part A, February 2000.
- J. W. Kwark, M. Y. Kim, D. J. Min, J. W. Lee, and E. S. Choi. Dynamic behaviour of submerged floating bridge due to moving high speed train. September 2013.
- E. V. Laitone. Limiting conditions for cnoidal and stokes waves. *Journal of Geophysical Research*, 67:1555–1564, 1962.
- H. K. Lee. Research center for smart submerged floating tunnel system. Trondheim Conference 2018, November 2018.
- X. Long, F. Ge, and Y. Hong. Feasibility study on buoyancy–weight ratios of a submerged floating tunnel prototype subjected to hydrodynamic loads. *Acta Mechanica Sinica*, 31(5):750–761, 2015. doi: 10.1007/s10409-015-0428-3.
- M. M. Lwin. Floating bridges. In *Bridge Engineering Handbook*, pages 564–587. CRC Press, 2014.
- R. C. MacCamy and R. A. Fuchs. Wave forces on piles: a diffraction theory. Technical report, Corps of Engineers Washington DC Beach Erosion Board, 1954.
- G. Martire. *The development of submerged floating tunnel as an innovative solution for waterway crossings*. PhD thesis, PhD Thesis in Construction Engineering, University of Naples “Federico II ...”, November 2010. URL <http://www.fedoa.unina.it/id/eprint/8407>.
- G. Martire, F. M. Mazzolani, B. Faggiano, and T. A. Stabile. On the behaviour of submerged floating tunnels during severe seismic events. In *ANIDIS 2011 - XIV convegno di Ingegneria Sismica*, 2011.
- F. M. Mazzolani, R. Landolfo, B. Faggiano, M. Esposto, G. Martire, F. Perotti, M. Di Pilato, G. Barbella, and A. Fiorentino. The archimede’s bridge prototype in qiandao lake (PR of china). Technical report, Sino-Italian Joint Laboratory of Archimedes Bridge (SIJLAB), 2007.
- F. M. Mazzolani, R. Landolfo, B. Faggiano, M. Esposto, F. Perotti, and G. Barbella. Structural analyses of the submerged floating tunnel prototype in qiandao lake (PR of china). *Advances in Structural Engineering*, 11(4):439–454, 2008. doi: <https://doi.org/10.1260/136943308785836862>.
- F. M. Mazzolani, B. Faggiano, and G. Martire. Design aspects of the AB prototype in the qiandao lake. *Procedia Engineering*, 4:21–33, 2010. doi: 10.1016/j.proeng.2010.08.005.
- A. Minoretti. A new possibility for crossing: the submerged floating tube bridge. Trondheim Conference 2018, November 2018.
- F. Perotti, G. Barbella, and M. Di Pilato. The dynamic behaviour of archimede’s bridges: numerical simulation and design implications. *Procedia Engineering*, 4:91 – 98, 2010. ISSN 1877-7058. doi: <https://doi.org/10.1016/j.proeng.2010.08.011>. URL <http://www.sciencedirect.com/science/article/pii/S1877705810005084>. ISAB-2010.
- T. Sarpkaya and M. Isaacson. *Mechanics of wave forces on offshore structures*. Van Nostrand Reinhold Co., 1981. ISBN 9780442254025. URL <https://books.google.nl/books?id=CVG6AAAAIAAJ>.
- M. Sato, S. Kanie, and T. Mikami. Mathematical analogy of a beam on elastic supports as a beam on elastic foundation. *Applied Mathematical Modelling*, 32(5):688–699, may 2008. doi: 10.1016/j.apm.2007.02.002.
- J. M. J. Spijkers, A. W. C. M. Vrouwenvelder, and E. C. Klaver. *Dynamics of structures part 1 vibration of structures*. Delft University of Technology, 2006.
- T. H. Søreide and S. A. Haugerud. Bjørnafjorden røyrbu (submerged floating tunnel) K3-K4 technical report. Technical report, May 2016.

- Z. Su and S. Sun. Seismic response of submerged floating tunnel tether. *China Ocean Engineering*, 27(1): 43–50, 2013. doi: <https://doi.org/10.1007/s13344-013-0004-1>.
- S. Tariverdilo, J. Mirzapour, M. Shahmardani, R. Shabani, and C. Gheyretmand. Vibration of submerged floating tunnels due to moving loads. *Applied Mathematical Modelling*, 35(11):5413–5425, nov 2011. doi: 10.1016/j.apm.2011.04.038.
- E. Wahyuni, E. Budiman, and I. G. Putu Raka. Dynamic behaviour of submerged floating tunnels under seismic loadings with different cable configurations. *IPTEK, The Journal for Technology and Science*, 23(2), 2012. doi: <http://dx.doi.org/10.12962/j20882033.v23i2.11>.
- Y. B. Yang, J. D. Yau, Z. Yao, and Y. S. Wu. *Vehicle-bridge interaction dynamics: with applications to high-speed railways*. World Scientific, 2004. ISBN 981-238-847-8.
- K. Youcef, T. Sabiha, D. El Mostafa, D. Ali, and M. Bachir. Dynamic analysis of train-bridge system and riding comfort of trains with rail irregularities. *Journal of Mechanical Science and Technology*, 27(4):951–962, 2013. doi: 10.1007/s12206-013-0206-8.
- Z. Yuan, D. Man-sheng, D. Hao, and Y. Long-chang. Displacement response of submerged floating tunnel tube due to single moving load. *Procedia Engineering*, 166:143–151, 2016. doi: <https://doi.org/10.1016/j.proeng.2016.11.577>.

A

Solution of Dynamic Bending Vibration of Euler-Bernoulli Beam

In this appendix it is offered the derivation of the natural frequencies and modal shapes for a simply-supported floating tunnel.

The governing partial differential equation for a simply-supported floating tunnel modelled as a Euler-Bernoulli beam is given in Spijkers et al. [37]:

$$m \frac{\partial^2 w(x, t)}{\partial t^2} + EI \frac{\partial^4 w(x, t)}{\partial x^4} = f(x, t) \quad (\text{A.1})$$

To study the dynamic response of the structure it is necessary to solve the carry out the modal analysis and determine the natural frequencies. When dealing with the free vibration analysis, the right side of (A.1) is set to zero. Using the method of separation of variables with the modal expansion, the PDE is reduced to a system of ODEs, whose only unknown variable is the time. The solution $w(x, t)$ can be assumed of the form

$$w(x, t) = \sum_{n=1}^{\infty} \Phi_n(x) \Psi_n(t) \quad (\text{A.2})$$

Substituting the solution into (A.1) one gets:

$$m \sum_{n=1}^{\infty} \Phi_n(x) \ddot{\Psi}_n(t) + EI \sum_{n=1}^{\infty} \Phi_n''''(x) \Psi_n(t) = 0 \quad (\text{A.3})$$

General solution for $\Phi_n(x)$ is:

$$\Phi_n(x) = A \cosh \beta x + B \sinh \beta x + C \cos \beta x + D \sin \beta x \quad (\text{A.4})$$

where

$$\beta = \sqrt[4]{\frac{m}{EI} \omega_n^2} \quad (\text{A.5})$$

Substituting of the displacement into the boundary conditions, which are:

$$\begin{cases} \Phi(0) = 0 \\ EI\Phi''(0) = 0 \\ \Phi(L) = 0 \\ EI\Phi''(L) = 0 \end{cases}$$

gives a system of 4 linear algebraic equations with respect to A, B, C, D. By setting the determinant of the coefficient matrix of the system of equations to zero, one can define the frequency equation. The solution of frequency equation provides a value for β which determines the natural frequencies.

$$\beta_n = \frac{n\pi}{L} \quad (\text{A.6a})$$

$$\omega_n = \left(\frac{n\pi}{L}\right)^2 \sqrt{\frac{EI}{m}} \quad (\text{A.6b})$$

Finding the ratios A/D, B/D, C/D and substituting the natural frequencies into (A.4) gives the normal modes, that for a simply-supported tunnel are:

$$\Phi_n(x) = \sin \frac{n\pi}{L} x \quad (\text{A.7})$$

B

Determination of cable stiffness

In this appendix it is offered the derivation of the stiffness of the supporting cable system, valid when small displacements, δy and/or δz , occur to the tunnel. Generalised geometrical and and mechanical properties will be adopted in the derivation, e.g. cable's length L , cross-sectional area A , Young's modulus E , inclination angle α and pretension T_0 .

B.1. Vertical Cables Stiffness in Sway Motion

The change in the tension force in the vertical cable due to a horizontal displacement, as shown in Figure B.1, can be expressed by:

$$\Delta T_y = \frac{EA}{L} \left(\sqrt{\delta y^2 + L^2} - L \right) \quad (\text{B.1})$$

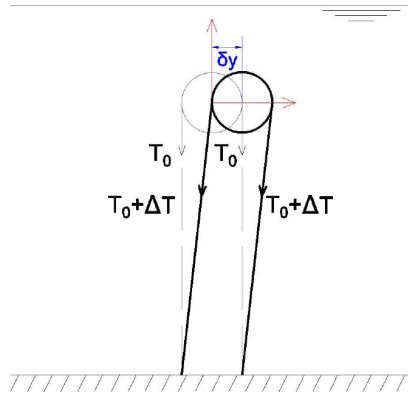


Figure B.1: Vertical Cable Sway Motion

The equilibrium of forces in the horizontal direction states:

$$k_y \delta y = 2(T_0 + \Delta T_y) \sin \beta \quad (\text{B.2})$$

where

$$\sin \beta = \frac{\delta y}{\sqrt{\delta y^2 + L^2}} \quad (\text{B.3})$$

Using (B.1) and (B.3), (B.2) can be rearranged to obtain the expression for the horizontal stiffness k_x :

$$k_y = \frac{2T_0}{\sqrt{\delta y^2 + L^2}} + \frac{2EA}{L} \left(1 - \frac{L}{\sqrt{\delta y^2 + L^2}} \right) \quad (\text{B.4})$$

For small values of δy the second term of the summation becomes negligible and the expression of the horizontal stiffness can be rewritten as:

$$k_y = \frac{2T_0}{L} \quad (\text{B.5})$$

B.2. Vertical Cables Stiffness in Heave Motion

The change in the tension force in the vertical cable due to a vertical displacement, as shown in Figure B.2, can be expressed by:

$$\Delta T_z = \frac{EA}{L} \delta z \quad (\text{B.6})$$

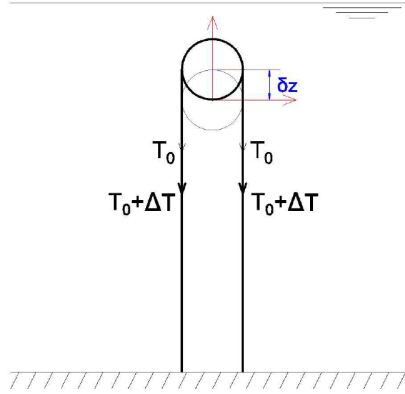


Figure B.2: Vertical Cable Heave Motion

The equilibrium of forces in the vertical direction states:

$$k_z \delta z = 2(T_0 + \Delta T_z) - 2T_0 \quad (\text{B.7})$$

Inserting the expression of (B.6) in (B.7) the expression for the vertical stiffness can be derived:

$$k_z = \frac{2EA}{L} \quad (\text{B.8})$$

B.3. Inclined Cables Stiffness in Sway Motion

The change in the tension force in the inclined cable due to a horizontal displacement, as shown in Figure B.3, can be expressed by:

$$\Delta T_y = \frac{AE}{L} \Delta L \quad (\text{B.9})$$

where

$$\Delta L = \delta y \sin \theta \quad (\text{B.10})$$

and θ is the increment in the inclination.

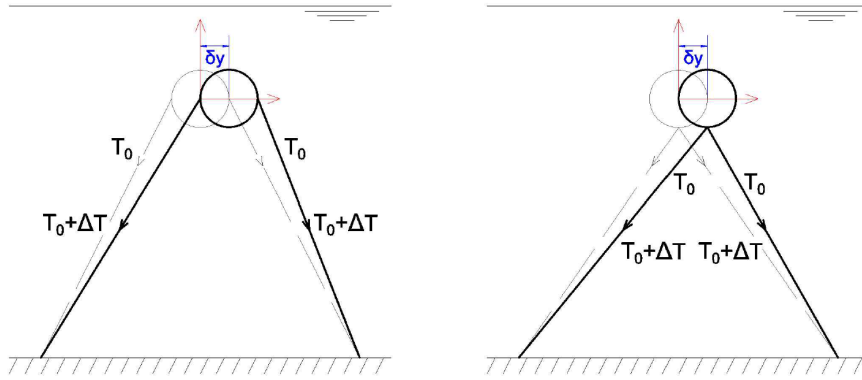


Figure B.3: Inclined Cable Sway Motion

The equilibrium of forces in the horizontal direction states:

$$k_y \delta y = (T_0 + \Delta T_y) \sin \theta - (T_0 - \Delta T_y) \sin \theta \tag{B.11}$$

Using (B.9) and (B.10), (B.11) can be rearranged to obtain the expression for the horizontal stiffness k_y :

$$k_y = \frac{2AE}{L} \sin^2 \theta \tag{B.12}$$

B.4. Inclined Cables Stiffness in Heave Motion

The change in the tension force in the inclined cable due to a vertical displacement, as shown in Figure B.4, can be expressed by:

$$\Delta T_z = \frac{EA}{L} \Delta L \tag{B.13}$$

where

$$\Delta L = \delta z \cos \theta \tag{B.14}$$

and θ is the reduction in the inclination.

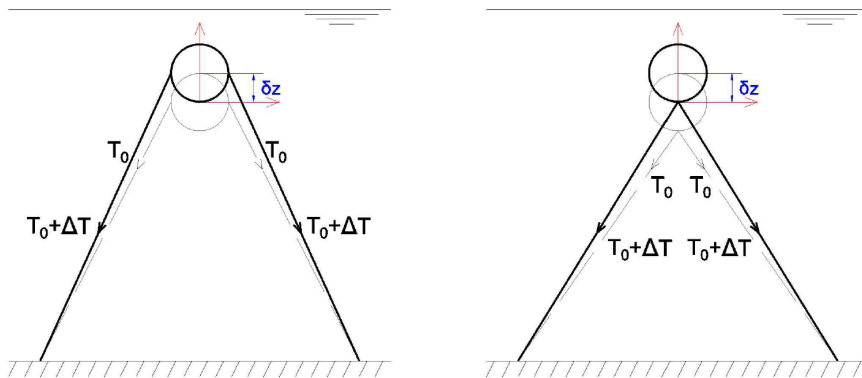


Figure B.4: Inclined Cable Heave Motion

The equilibrium of forces in the vertical direction states:

$$k_z \delta z = 2(T_0 + \Delta T_z) \cos \theta - 2T_0 \cos \theta \tag{B.15}$$

Using (B.13) and (B.14), (B.15) can be rearranged to obtain the expression for the vertical stiffness k_z :

$$k_z = \frac{2AE}{L} \cos^2 \theta \tag{B.16}$$

C

Solution of Dynamic Bending Vibration of BOEF

In this appendix it is offered the derivation of the natural frequencies of the SFT modelled as a BOEF. The modal expansion method is applied as it has been proved by Martire [28], Sato et al. [36] that is still valid.

The governing PDE for the dynamic analysis of a cable-stayed SFT modelled as a BOEF is:

$$m \frac{\partial^2 w(x, t)}{\partial t^2} + EI \frac{\partial^4 w(x, t)}{\partial x^4} + k_f w(x, t) = f(x, t) \quad (C.1)$$

where

m is the mass per unit length of the tunnel plus the added mass

EI is the bending stiffness of the tunnel

$k_f = \frac{k_v}{h}$ is the distributed support system.

As previously determined in Appendix A the adopted solution method is the modal expansion method with a modal shape that, again, is the sine function, as it still satisfies the boundary conditions. So, the displacement can be expressed as:

$$w(x, t) = \sum_{n=1}^{\infty} \Phi_n(x) \Psi_n(t) = \sum_{n=1}^{\infty} \sin \frac{n\pi}{L} x \Psi_n(t) \quad (C.2)$$

Substituting (C.2) into (C.1), one obtains:

$$m \sum_{n=1}^{\infty} \sin \frac{n\pi}{L} x \ddot{\Psi}_n(t) + EI \sum_{n=1}^{\infty} \left(\frac{n\pi}{L} \right)^4 \sin \frac{n\pi}{L} x \Psi_n(t) + k_f \sum_{n=1}^{\infty} \sin \frac{n\pi}{L} x \Psi_n(t) = f(x, t) \quad (C.3)$$

Premultiplying both sides of (C.3) by $\sin \frac{m\pi}{L} x$ and integrating over the tunnel length, thanks to the orthogonality of the modes, the terms of the equation gives:

$$\int_0^L \sin \frac{m\pi}{L} x m \sin \frac{n\pi}{L} x dx = m \frac{L}{2} \quad (C.4a)$$

$$\int_0^L \sin \frac{m\pi}{L} x EI \left(\frac{n\pi}{L} \right)^4 \sin \frac{n\pi}{L} x + \sin \frac{m\pi}{L} x k_f \sin \frac{n\pi}{L} x dx = \left(\left(\frac{n\pi}{L} \right)^4 EI + m \right) \frac{L}{2} \quad (C.4b)$$

$$\int_0^L \sin \frac{m\pi}{L} x f(x, t) dx \quad (C.4c)$$

The PDE has been transformed into a infinite system of ODEs, which are:

$$m \frac{L}{2} \ddot{\Psi}_n(t) + \left(\left(\frac{n\pi}{L} \right)^4 EI + m \right) \frac{L}{2} \Psi_n(t) = \int_0^L \sin \frac{n\pi}{L} x f(x, t) dx \quad (C.5)$$

The natural frequencies of the n^{th} mode can be evaluated dividing each term of (C.5) by $m \frac{L}{2}$:

$$\ddot{\Psi}_n(t) + \omega_n^2 \Psi_n(t) = \frac{2}{mL} \int_0^L \sin \frac{n\pi}{L} x f(x, t) dx \quad (C.6)$$

where

$$\omega_n = \sqrt{\left(\frac{n\pi}{L}\right)^4 \frac{EI}{m} + \frac{k_f}{m}} \quad (\text{C.7})$$

$$w_z(x, t) = \sum_{n=1}^{\infty} \Phi_n(x) q_{zb_n}(t) = \sum_{n=1}^{\infty} \sin \frac{n\pi}{L} q_{zb_n}(t) \quad (\text{D.4b})$$

$$\varphi_x(x, t) = \sum_{n=1}^{\infty} \Phi_n(x) q_{\varphi b_n}(t) = \sum_{n=1}^{\infty} \sin \frac{n\pi}{L} q_{\varphi b_n}(t) \quad (\text{D.4c})$$

The application of the orthogonality property to each equation composing the system to analyse the FSVI is reported in the sections below.

D.1. Orthogonality in y-direction

$$m \frac{\partial^2 w_y(x, t)}{\partial t^2} \rightarrow \int_0^L \Phi_m(x) m \sum_{n=1}^{\infty} \Phi_n(x) \ddot{q}_{yb_n}(t) dx = m \frac{L}{2} \ddot{q}_{yb_n}(t) \quad (\text{D.5a})$$

$$c_y \frac{\partial w_y(x, t)}{\partial t} \rightarrow \int_0^L \Phi_m(x) c_y \sum_{n=1}^{\infty} \Phi_n(x) \dot{q}_{yb_n}(t) dx = c_y \frac{L}{2} \dot{q}_{yb_n}(t) \quad (\text{D.5b})$$

$$EI \frac{\partial^4 w_y(x, t)}{\partial x^4} \rightarrow \int_0^L \Phi_m(x) EI \sum_{n=1}^{\infty} \Phi_n'''(x) q_{yb_n}(t) dx = \left(\frac{n\pi}{L}\right)^4 EI \frac{L}{2} q_{yb_n}(t) \quad (\text{D.5c})$$

$$\sum_{N=1}^{n_c} k_y w_y(x_N, t) \delta(x - x_N) \rightarrow \int_0^L \Phi_m(x) k_y \sum_{N=1}^{n_c} \sum_{n=1}^{\infty} \Phi_n(x_N) q_{yb_n}(t) \delta(x - x_N) dx = \quad (\text{D.5d})$$

$$k_y \sum_{N=1}^{n_c} \Phi_m(x_N) \sum_{n=1}^{\infty} \Phi_n(x_N) q_{yb_n}(t) \\ C_a \rho_f \pi \frac{D^2}{4} \dot{v}_y \rightarrow \int_0^L C_a \rho_f \pi \frac{D^2}{4} \dot{v}_y \Phi_n(x) dx \quad (\text{D.5e})$$

$$\frac{1}{2} \rho_f C_D D (v_y - \dot{w}_y(x, t)) |v_y - \dot{w}_y(x, t)| \rightarrow \int_0^L \frac{1}{2} C_D \rho_f D \Phi_m(x) \left(v_y - \sum_{n=1}^{\infty} \Phi_n(x) \dot{q}_{yb_n}(t) \right) \sqrt{\left(v_y - \sum_{n=1}^{\infty} \Phi_n(x) \dot{q}_{yb_n}(t) \right)^2 + \left(v_z - \sum_{n=1}^{\infty} \Phi_n(x) \dot{q}_{zb_n}(t) \right)^2} dx \quad (\text{D.5f})$$

$$\sum_{N=1}^{n_c} \frac{k_\varphi}{R} \varphi_x(x_N, t) \delta(x - x_N) \rightarrow \int_0^L \Phi_m(x) \frac{k_\varphi}{R} \sum_{N=1}^{n_c} \sum_{n=1}^{\infty} \Phi_n(x_N) q_{\varphi b_n}(t) \delta(x - x_N) dx = \quad (\text{D.5g}) \\ \frac{k_\varphi}{R} \sum_{N=1}^{n_c} \Phi_m(x_N) \sum_{n=1}^{\infty} \Phi_n(x_N) q_{\varphi b_n}(t)$$

D.2. Orthogonality in z-direction

$$m \frac{\partial^2 w_z(x, t)}{\partial t^2} \rightarrow \int_0^L \Phi_m(x) m \sum_{n=1}^{\infty} \Phi_n(x) \ddot{q}_{zb_n}(t) dx = m \frac{L}{2} \ddot{q}_{zb_n}(t) \quad (\text{D.6a})$$

$$c_z \frac{\partial w_z(x, t)}{\partial t} \rightarrow \int_0^L \Phi_m(x) c_z \sum_{n=1}^{\infty} \Phi_n(x) \dot{q}_{zb_n}(t) dx = c_z \frac{L}{2} \dot{q}_{zb_n}(t) \quad (\text{D.6b})$$

$$EI \frac{\partial^4 w_z(x, t)}{\partial x^4} \rightarrow \int_0^L \Phi_m(x) EI \sum_{n=1}^{\infty} \Phi_n'''(x) q_{zb_n}(t) dx = \left(\frac{n\pi}{L}\right)^4 EI \frac{L}{2} q_{zb_n}(t) \quad (\text{D.6c})$$

$$\sum_{N=1}^{n_c} k_z w_z(x_N, t) \delta(x - x_N) \rightarrow \int_0^L \Phi_m(x) k_z \sum_{N=1}^{n_c} \sum_{n=1}^{\infty} \Phi_n(x_N) q_{zb_n}(t) \delta(x - x_N) dx = \quad (\text{D.6d})$$

$$k_z \sum_{N=1}^{n_c} \Phi_m(x_N) \sum_{n=1}^{\infty} \Phi_n(x_N) q_{zb_n}(t)$$

$$C_a \rho_f \pi \frac{D^2}{4} \dot{v}_z \rightarrow \int_0^L C_a \rho_f \pi \frac{D^2}{4} \dot{v}_z \Phi_n(x) dx \quad (\text{D.6e})$$

$$\frac{1}{2} \rho_f C_D D (v_z - \dot{w}_z(x, t)) |v_z - \dot{w}_z(x, t)| \rightarrow \int_0^L \frac{1}{2} C_D \rho_f D \Phi_m(x) \left(v_z - \sum_{n=1}^{\infty} \Phi_n(x) \dot{q}_{zb_n}(t) \right) \sqrt{\left(v_y - \sum_{n=1}^{\infty} \Phi_n(x) \dot{q}_{yb_n}(t) \right)^2 + \left(v_z - \sum_{n=1}^{\infty} \Phi_n(x) \dot{q}_{zb_n}(t) \right)^2} dx \quad (\text{D.6f})$$

$$m_w \frac{\partial^2 w_z(Vt, t)}{\partial t^2} \delta(x - Vt) H_t \rightarrow \int_0^L \Phi_m(x) m_w \sum_{n=1}^{\infty} \Phi_n(Vt) \ddot{q}_{zb_n}(t) (x - Vt) H_t dx = m_w \Phi_m(Vt) \Phi_n(Vt) \ddot{q}_{zb_n}(t) H_t \quad (\text{D.6g})$$

$$m_w 2V \frac{\partial^2 w_z(Vt, t)}{\partial x \partial t} \delta(x - Vt) H_t \rightarrow \int_0^L \Phi_m(x) m_w 2V \sum_{n=1}^{\infty} \Phi_n'(Vt) \dot{q}_{zb_n}(t) (x - Vt) H_t dx = m_w 2V \Phi_m(Vt) \frac{n\pi}{L} \Phi_n'(Vt) \dot{q}_{zb_n}(t) H_t \quad (\text{D.6h})$$

$$m_w V^2 \frac{\partial^2 w_z(Vt, t)}{\partial x^2} \delta(x - Vt) H_t \rightarrow \int_0^L \Phi_m(x) m_w V^2 \sum_{n=1}^{\infty} \Phi_n''(Vt) q_{zb_n}(t) (x - Vt) H_t dx = m_w V^2 \Phi_m(Vt) \left(\frac{n\pi}{L} \right)^2 \Phi_n''(Vt) q_{zb_n}(t) H_t \quad (\text{D.6i})$$

$$c_{S1} \frac{\partial w_z(Vt, t)}{\partial t} \delta(x - Vt) H_t \rightarrow \int_0^L \Phi_m(x) c_{S1} \sum_{n=1}^{\infty} \Phi_n(Vt) \dot{q}_{zb_n}(t) (x - Vt) H_t dx = c_{S1} \Phi_m(Vt) \Phi_n(Vt) \dot{q}_{zb_n}(t) H_t \quad (\text{D.6j})$$

$$c_{S1} V \frac{\partial w_z(Vt, t)}{\partial x} \delta(x - Vt) H_t \rightarrow \int_0^L \Phi_m(x) c_{S1} V \sum_{n=1}^{\infty} \Phi_n'(Vt) q_{zb_n}(t) (x - Vt) H_t dx = c_{S1} V \Phi_m(Vt) \frac{n\pi}{L} \Phi_n'(Vt) q_{zb_n}(t) H_t \quad (\text{D.6k})$$

$$k_{S1} w_z(Vt, t) \delta(x - Vt) H_t \rightarrow \int_0^L \Phi_m(x) k_{S1} \sum_{n=1}^{\infty} \Phi_n(Vt) q_{zb_n}(t) (x - Vt) H_t dx = k_{S1} \Phi_m(Vt) \Phi_n(Vt) q_{zb_n}(t) H_t \quad (\text{D.6l})$$

D.3. Orthogonality in ϕ -direction

$$mR^2 \frac{\partial^2 \varphi_x(x, t)}{\partial t^2} \rightarrow \int_0^L \Phi_m(x) mR^2 \sum_{n=1}^{\infty} \Phi_n(x) \ddot{q}_{\phi b_n}(t) dx = mR^2 \frac{L}{2} \ddot{q}_{\phi b_n}(t) \quad (\text{D.7a})$$

$$c_\varphi \frac{\partial \varphi_x(x, t)}{\partial t} \rightarrow \int_0^L \Phi_m(x) c_\varphi \sum_{n=1}^{\infty} \Phi_n(x) \dot{q}_{\phi b_n}(t) dx = c_\varphi \frac{L}{2} \dot{q}_{\phi b_n}(t) \quad (\text{D.7b})$$

$$GJ \frac{\partial^2 \varphi_x(x, t)}{\partial x^2} \rightarrow \int_0^L \Phi_m(x) GJ \sum_{n=1}^{\infty} \Phi_n''(x) q_{\phi b_n}(t) dx = \left(\frac{n\pi}{L} \right)^2 GJ \frac{L}{2} q_{\phi b_n}(t) \quad (\text{D.7c})$$

$$\begin{aligned}
& \sum_{N=1}^{n_c} k_\varphi \varphi_x(x_N, t) \delta(x - x_N) \rightarrow \\
\int_0^L \Phi_m(x) k_\varphi \sum_{N=1}^{n_c} \sum_{n=1}^{\infty} \Phi_n(x_N) q_{\varphi b_n}(t) \delta(x - x_N) dx = & \quad (D.7d) \\
& k_\varphi \sum_{N=1}^{n_c} \Phi_m(x_N) \sum_{n=1}^{\infty} \Phi_n(x_N) q_{\varphi b_n}(t)
\end{aligned}$$

$$\begin{aligned}
& \sum_{N=1}^{n_c} k_y R w_y(x_N, t) \delta(x - x_N) \rightarrow \\
\int_0^L \Phi_m(x) k_y R \sum_{N=1}^{n_c} \sum_{n=1}^{\infty} \Phi_n(x_N) q_{y b_n}(t) \delta(x - x_N) dx = & \quad (D.7e) \\
& k_y R \sum_{N=1}^{n_c} \Phi_m(x_N) \sum_{n=1}^{\infty} \Phi_n(x_N) q_{y b_n}(t)
\end{aligned}$$

$$\begin{aligned}
& m_w \lambda^2 \frac{\partial^2 \varphi_x(Vt, t)}{\partial t^2} \delta(x - Vt) H_t \rightarrow \\
\int_0^L \Phi_m(x) m_w \lambda^2 \sum_{n=1}^{\infty} \Phi_n(Vt) \ddot{q}_{\varphi b_n}(t) (x - Vt) H_t dx = & \quad (D.7f) \\
& m_w \lambda^2 \Phi_m(Vt) \Phi_n(Vt) \ddot{q}_{\varphi b_n}(t) H_t
\end{aligned}$$

$$\begin{aligned}
& m_w \lambda^2 2V \frac{\partial^2 \varphi_x(Vt, t)}{\partial x \partial t} \delta(x - Vt) H_t \rightarrow \\
\int_0^L \Phi_m(x) m_w \lambda^2 2V \sum_{n=1}^{\infty} \Phi'_n(Vt) \dot{q}_{\varphi b_n}(t) (x - Vt) H_t dx = & \quad (D.7g) \\
& m_w \lambda^2 2V \Phi_m(Vt) \frac{n\pi}{L} \Phi'_n(Vt) \dot{q}_{\varphi b_n}(t) H_t
\end{aligned}$$

$$\begin{aligned}
& m_w \lambda^2 V^2 \frac{\partial^2 \varphi_x(Vt, t)}{\partial x^2} \delta(x - Vt) H_t \rightarrow \\
\int_0^L \Phi_m(x) m_w \lambda^2 V^2 \sum_{n=1}^{\infty} \Phi''_n(Vt) q_{\varphi b_n}(t) (x - Vt) H_t dx = & \quad (D.7h) \\
& m_w \lambda^2 V^2 \Phi_m(Vt) \left(\frac{n\pi}{L}\right)^2 \Phi''_n(Vt) q_{\varphi b_n}(t) H_t
\end{aligned}$$

$$\begin{aligned}
& c_{S1} \lambda^2 \frac{\partial \varphi_x(Vt, t)}{\partial t} \delta(x - Vt) H_t \rightarrow \\
\int_0^L \Phi_m(x) c_{S1} \lambda^2 \sum_{n=1}^{\infty} \Phi_n(Vt) \dot{q}_{\varphi b_n}(t) (x - Vt) H_t dx = & \quad (D.7i) \\
& c_{S1} \lambda^2 \Phi_m(Vt) \Phi_n(Vt) \dot{q}_{\varphi b_n}(t) H_t
\end{aligned}$$

$$\begin{aligned}
& c_{S1} \lambda^2 V \frac{\partial \varphi_x(Vt, t)}{\partial x} \delta(x - Vt) H_t \rightarrow \\
\int_0^L \Phi_m(x) c_{S1} \lambda^2 V \sum_{n=1}^{\infty} \Phi'_n(Vt) q_{\varphi b_n}(t) (x - Vt) H_t dx = & \quad (D.7j) \\
& c_{S1} \lambda^2 V \Phi_m(Vt) \frac{n\pi}{L} \Phi'_n(Vt) q_{\varphi b_n}(t) H_t
\end{aligned}$$

$$\begin{aligned}
& k_{S1} \lambda^2 \varphi_x(Vt, t) \delta(x - Vt) H_t \rightarrow \\
\int_0^L \Phi_m(x) k_{S1} \lambda^2 \sum_{n=1}^{\infty} \Phi_n(Vt) q_{\varphi b_n}(t) (x - Vt) H_t dx = & \quad (D.7k) \\
& k_{S1} \lambda^2 \Phi_m(Vt) \Phi_n(Vt) q_{\varphi b_n}(t) H_t
\end{aligned}$$

D.4. Matrix Assembling

The global mass, damping and stiffness matrices are described as:

$$M = \begin{bmatrix} M_y & 0 & 0 & 0 & 0 \\ 0 & M_z & 0 & 0 & 0 \\ 0 & 0 & M_\varphi & 0 & 0 \\ 0 & 0 & 0 & M_b & 0 \\ 0 & 0 & 0 & 0 & M_c \end{bmatrix}$$

$$C = \begin{bmatrix} C_y & 0 & 0 & 0 & 0 \\ 0 & C_z & C_{z\varphi} & C_{zb} & 0 \\ 0 & C_{\varphi z} & C_\varphi & C_{\varphi b} & 0 \\ 0 & C_{bz} & C_{b\varphi} & C_b & C_{bc} \\ 0 & 0 & 0 & C_{cb} & C_c \end{bmatrix}$$

$$K = \begin{bmatrix} K_y & 0 & K_{y\varphi} & 0 & 0 \\ 0 & K_z & K_{z\varphi} & K_{zb} & 0 \\ K_{\varphi y} & K_{\varphi z} & K_\varphi & K_{\varphi b} & 0 \\ 0 & K_{bz} & K_{b\varphi} & K_b & K_{bc} \\ 0 & 0 & 0 & K_{cb} & K_c \end{bmatrix}$$

where

$$M_y = \begin{bmatrix} m\frac{L}{2} & 0 & 0 \\ 0 & \ddots & 0 \\ 0 & 0 & m\frac{L}{2} \end{bmatrix}$$

$$M_z = \begin{bmatrix} m\frac{L}{2} + & \dots & m_w\Phi_n(Vt)\Phi_1(Vt)H_t \\ m_w\Phi_1(Vt)\Phi_1(Vt)H_t & \ddots & \vdots \\ \vdots & \ddots & m\frac{L}{2} + \\ m_w\Phi_1(Vt)\Phi_n(Vt)H_t & \dots & m_w\Phi_n(Vt)\Phi_n(Vt)H_t \end{bmatrix}$$

$$M_\varphi = \begin{bmatrix} mR^2\frac{L}{2} + & \dots & m_w\lambda^2\Phi_n(Vt)\Phi_1(Vt)H_t \\ m_w\lambda^2\Phi_1(Vt)\Phi_1(Vt)H_t & \ddots & \vdots \\ \vdots & \ddots & mR^2\frac{L}{2} + \\ m_w\lambda^2\Phi_1(Vt)\Phi_n(Vt)H_t & \dots & m_w\lambda^2\Phi_n(Vt)\Phi_n(Vt)H_t \end{bmatrix}$$

$$C_y = \begin{bmatrix} c_y\frac{L}{2} & 0 & 0 \\ 0 & \ddots & 0 \\ 0 & 0 & c_y\frac{L}{2} \end{bmatrix}$$

$$C_z = \begin{bmatrix} c_z\frac{L}{2} + & \dots & m_w2V\Phi_n(Vt)\frac{1}{L}\Phi_1'(Vt)H_t + \\ m_w2V\Phi_1(Vt)\frac{1}{L}\Phi_1'(Vt)H_t + & \dots & c_{S1}\Phi_n(Vt)\Phi_1(Vt)H_t \\ \vdots & \ddots & \vdots \\ \vdots & \ddots & c_z\frac{L}{2} \\ m_w2V\Phi_1(Vt)\frac{n\pi}{L}\Phi_n'(Vt)H_t + & \dots & m_w2V\Phi_n(Vt)\frac{n\pi}{L}\Phi_n'(Vt)H_t + \\ c_{S1}\Phi_1(Vt)\Phi_n(Vt)H_t & \dots & c_{S1}\Phi_n(Vt)\Phi_n(Vt)H_t \end{bmatrix}$$

$$C_\varphi = \begin{bmatrix} c_\varphi\frac{L}{2} + & \dots & m_w\lambda^22V\Phi_n(Vt)\frac{1}{L}\Phi_1'(Vt)H_t + \\ m_w\lambda^22V\Phi_1(Vt)\frac{1}{L}\Phi_1'(Vt)H_t + & \dots & c_{S1}\lambda^2\Phi_n(Vt)\Phi_1(Vt)H_t \\ \vdots & \ddots & \vdots \\ \vdots & \ddots & m\frac{L}{2} + \\ m_w\lambda^22V\Phi_1(Vt)\frac{n\pi}{L}\Phi_n'(Vt)H_t + & \dots & m_w\lambda^22V\Phi_n(Vt)\frac{n\pi}{L}\Phi_n'(Vt)H_t + \\ c_{S1}\lambda^2\Phi_1(Vt)\Phi_n(Vt)H_t & \dots & c_{S1}\lambda^2\Phi_n(Vt)\Phi_n(Vt)H_t \end{bmatrix}$$

$$K_y = \begin{bmatrix} \left(\frac{1\pi}{L}\right)^4 EI \frac{L}{2} + & \dots & \\ k_y \sum_{N=1}^{n_c} \Phi_1(x_N) \Phi_1(x_N) & & k_y \sum_{N=1}^{n_c} \Phi_n(x_N) \Phi_1(x_N) \\ \vdots & \ddots & \vdots \\ k_y \sum_{N=1}^{n_c} \Phi_1(x_N) \Phi_n(x_N) & \dots & k_y \sum_{N=1}^{n_c} \Phi_n(x_N) \Phi_n(x_N) + \left(\frac{n\pi}{L}\right)^4 EI \frac{L}{2} + \end{bmatrix}$$

$$K_z = \begin{bmatrix} \left(\frac{1\pi}{L}\right)^4 EI \frac{L}{2} + & & & \\ k_z \sum_{N=1}^{n_c} \Phi_1(x_N) \Phi_1(x_N) + & & k_z \sum_{N=1}^{n_c} \Phi_n(x_N) \Phi_1(x_N) + & \\ m_w V^2 \Phi_1(Vt) \frac{1\pi}{L} \Phi_1'(Vt) H_t + & \dots & m_w V^2 \Phi_n(Vt) \frac{1\pi}{L} \Phi_1'(Vt) H_t + & \\ k_{S1} \Phi_1(Vt) \Phi_1(Vt) H_t + & & k_{S1} \Phi_n(Vt) \Phi_1(Vt) H_t + & \\ c_{S1} V \Phi_1(Vt) \Phi_1'(Vt) H_t & & c_{S1} V \Phi_n(Vt) \Phi_1'(Vt) H_t & \\ \vdots & \ddots & \vdots & \\ \left(\frac{n\pi}{L}\right)^4 EI \frac{L}{2} + & & & \\ k_z \sum_{N=1}^{n_c} \Phi_1(x_N) \Phi_n(x_N) + & & k_z \sum_{N=1}^{n_c} \Phi_n(x_N) \Phi_n(x_N) + & \\ m_w V^2 \Phi_1(Vt) \frac{n\pi}{L} \Phi_n'(Vt) H_t + & \dots & m_w V^2 \Phi_n(Vt) \frac{n\pi}{L} \Phi_n'(Vt) & \\ k_{S1} \Phi_1(Vt) \Phi_n(Vt) H_t + & & k_{S1} \Phi_n(Vt) \Phi_n(Vt) + & \\ c_{S1} V \Phi_1(Vt) \Phi_n'(Vt) H_t & & c_{S1} V \Phi_n(Vt) \Phi_n'(Vt) H_t & \end{bmatrix}$$

$$K_\varphi = \begin{bmatrix} \left(\frac{1\pi}{L}\right)^2 GJ \frac{L}{2} + & & & \\ k_z \sum_{N=1}^{n_c} \Phi_1(x_N) \Phi_1(x_N) + & & k_z \sum_{N=1}^{n_c} \Phi_n(x_N) \Phi_1(x_N) + & \\ m_w \lambda^2 V^2 \Phi_1(Vt) \frac{1\pi}{L} \Phi_1''(Vt) H_t + & \dots & m_w \lambda^2 V^2 \Phi_n(Vt) \frac{1\pi}{L} \Phi_1''(Vt) H_t + & \\ k_{S1} \lambda^2 \Phi_1(Vt) \Phi_1(Vt) H_t + & & k_{S1} \lambda^2 \Phi_n(Vt) \Phi_1(Vt) H_t + & \\ c_{S1} \lambda^2 V \Phi_1(Vt) \Phi_1'(Vt) H_t & & c_{S1} \lambda^2 V \Phi_n(Vt) \Phi_1'(Vt) H_t & \\ \vdots & \ddots & \vdots & \\ \left(\frac{n\pi}{L}\right)^2 GJ \frac{L}{2} + & & & \\ k_z \sum_{N=1}^{n_c} \Phi_1(x_N) \Phi_n(x_N) + & & k_z \sum_{N=1}^{n_c} \Phi_n(x_N) \Phi_n(x_N) + & \\ m_w \lambda^2 V^2 \Phi_1(Vt) \frac{n\pi}{L} \Phi_n''(Vt) H_t + & \dots & m_w \lambda^2 V^2 \Phi_n(Vt) \frac{n\pi}{L} \Phi_n''(Vt) + & \\ k_{S1} \lambda^2 \Phi_1(Vt) \Phi_n(Vt) H_t + & & k_{S1} \lambda^2 \Phi_n(Vt) \Phi_n(Vt) + & \\ c_{S1} \lambda^2 V \Phi_1(Vt) \Phi_n'(Vt) H_t & & c_{S1} \lambda^2 V \Phi_n(Vt) \Phi_n'(Vt) H_t & \end{bmatrix}$$

$$C_{z\varphi} = \begin{bmatrix} m_w \lambda 2V \Phi_1(Vt) \frac{1\pi}{L} \Phi_1'(Vt) H_t + & \dots & m_w \lambda 2V \Phi_n(Vt) \frac{1\pi}{L} \Phi_1'(Vt) H_t + & \\ c_{S1} \lambda \Phi_1(Vt) \Phi_1(Vt) H_t & & c_{S1} \lambda \Phi_n(Vt) \Phi_1(Vt) H_t & \\ \vdots & \ddots & \vdots & \\ m_w \lambda 2V \Phi_1(Vt) \frac{n\pi}{L} \Phi_n'(Vt) H_t + & & m_w \lambda 2V \Phi_n(Vt) \frac{n\pi}{L} \Phi_n'(Vt) H_t + & \\ c_{S1} \lambda \Phi_1(Vt) \Phi_n(Vt) H_t & \dots & c_{S1} \lambda \Phi_n(Vt) \Phi_n(Vt) H_t & \end{bmatrix}$$

$$C_{\varphi z} = C_{z\varphi}^T$$

$$C_{zb} = C_{bz}^T = \begin{bmatrix} m_w \lambda 2V \Phi_1(Vt) \frac{1\pi}{L} \Phi_1'(Vt) H_t + & \dots & m_w \lambda 2V \Phi_n(Vt) \frac{1\pi}{L} \Phi_1'(Vt) H_t + & \\ c_{S1} \lambda \Phi_1(Vt) \Phi_1(Vt) H_t & & c_{S1} \lambda \Phi_n(Vt) \Phi_1(Vt) H_t & \\ \vdots & \ddots & \vdots & \\ m_w \lambda 2V \Phi_1(Vt) \frac{n\pi}{L} \Phi_n'(Vt) H_t + & & m_w \lambda 2V \Phi_n(Vt) \frac{n\pi}{L} \Phi_n'(Vt) H_t + & \\ c_{S1} \lambda \Phi_1(Vt) \Phi_n(Vt) H_t & \dots & c_{S1} \lambda \Phi_n(Vt) \Phi_n(Vt) H_t & \end{bmatrix}$$

$$C_{bz} = C_{zb}^T$$

$$C_{\varphi b} = C_{b\varphi}^T = \begin{bmatrix} m_w \lambda 2V \Phi_1(Vt) \frac{1\pi}{L} \Phi_1'(Vt) H_t + & \dots & m_w \lambda 2V \Phi_n(Vt) \frac{1\pi}{L} \Phi_1'(Vt) H_t + & \\ c_{S1} \lambda \Phi_1(Vt) \Phi_1(Vt) H_t & & c_{S1} \lambda \Phi_n(Vt) \Phi_1(Vt) H_t & \\ \vdots & \ddots & \vdots & \\ m_w \lambda 2V \Phi_1(Vt) \frac{n\pi}{L} \Phi_n'(Vt) H_t + & & m_w \lambda 2V \Phi_n(Vt) \frac{n\pi}{L} \Phi_n'(Vt) H_t + & \\ c_{S1} \lambda \Phi_1(Vt) \Phi_n(Vt) H_t & \dots & c_{S1} \lambda \Phi_n(Vt) \Phi_n(Vt) H_t & \end{bmatrix}$$

$$C_{b\varphi} = C_{\varphi b}^T$$

$$K_{y\varphi} = \begin{bmatrix} \frac{k_\varphi}{R} \sum_{N=1}^{n_c} \Phi_1(x_N) \Phi_1(x_N) & \dots & \frac{k_\varphi}{R} \sum_{N=1}^{n_c} \Phi_n(x_N) \Phi_1(x_N) \\ \vdots & \ddots & \vdots \\ \frac{k_\varphi}{R} \sum_{N=1}^{n_c} \Phi_1(x_N) \Phi_n(x_N) & \dots & \frac{k_\varphi}{R} \sum_{N=1}^{n_c} \Phi_n(x_N) \Phi_n(x_N) \end{bmatrix}$$

$$K_{\varphi y} = K_{y\varphi}^T$$

$$K_{z\varphi} = \begin{bmatrix} m_w \lambda V^2 \Phi_1(Vt) \left(\frac{1\pi}{L}\right)^2 \Phi_1''(Vt) H_t + & \dots & m_w \lambda V^2 \Phi_n(Vt) \left(\frac{1\pi}{L}\right)^2 \Phi_1''(Vt) H_t + \\ k_{S1} \lambda \Phi_1(Vt) \Phi_1(Vt) H_t & & k_{S1} \lambda \Phi_n(Vt) \Phi_1(Vt) H_t \\ \vdots & \ddots & \vdots \\ m_w \lambda V^2 \Phi_1(Vt) \left(\frac{n\pi}{L}\right)^2 \Phi_n''(Vt) H_t + & \dots & m_w \lambda V^2 \Phi_n(Vt) \left(\frac{n\pi}{L}\right)^2 \Phi_n''(Vt) H_t + \\ k_{S1} \lambda \Phi_1(Vt) \Phi_n(Vt) H_t & & k_{S1} \lambda \Phi_n(Vt) \Phi_n(Vt) H_t \end{bmatrix}$$

$$K_{\varphi z} = K_{z\varphi}^T$$

$$K_{zb} = \begin{bmatrix} m_w \lambda V^2 \Phi_1(Vt) \left(\frac{1\pi}{L}\right)^2 \Phi_1''(Vt) H_t + & \dots & m_w \lambda V^2 \Phi_n(Vt) \left(\frac{1\pi}{L}\right)^2 \Phi_1''(Vt) H_t + \\ k_{S1} \lambda V \Phi_1(Vt) \Phi_1(Vt) H_t & & k_{S1} \lambda V \Phi_n(Vt) \Phi_1(Vt) H_t \\ \vdots & \ddots & \vdots \\ m_w \lambda V^2 \Phi_1(Vt) \left(\frac{n\pi}{L}\right)^2 \Phi_n''(Vt) H_t + & \dots & m_w \lambda V^2 \Phi_n(Vt) \left(\frac{n\pi}{L}\right)^2 \Phi_n''(Vt) H_t + \\ k_{S1} \lambda V \Phi_1(Vt) \Phi_n(Vt) H_t & & k_{S1} \lambda V \Phi_n(Vt) \Phi_n(Vt) H_t \end{bmatrix}$$

$$K_{bz} = K_{zb}^T$$

$$K_{\varphi b} = \begin{bmatrix} m_w \lambda 2V \Phi_1(Vt) \frac{1\pi}{L} \Phi_1'(Vt) H_t + & \dots & m_w \lambda 2V \Phi_n(Vt) \frac{1\pi}{L} \Phi_1'(Vt) H_t + \\ c_{S1} \lambda \Phi_1(Vt) \Phi_1(Vt) H_t & & c_{S1} \lambda \Phi_n(Vt) \Phi_1(Vt) H_t \\ \vdots & \ddots & \vdots \\ m_w \lambda 2V \Phi_1(Vt) \frac{n\pi}{L} \Phi_n'(Vt) H_t + & \dots & m_w \lambda 2V \Phi_n(Vt) \frac{n\pi}{L} \Phi_n'(Vt) H_t + \\ c_{S1} \lambda \Phi_1(Vt) \Phi_n(Vt) H_t & & c_{S1} \lambda \Phi_n(Vt) \Phi_n(Vt) H_t \end{bmatrix}$$

$$K_{b\varphi} = K_{\varphi b}^T$$

The remaining matrices, that have not been presented in this section, will be shown in the separate derivation in Appendix E. The right-hand-side of the system, i.e. the force vector, is composed by the terms related to the fluid-structure-interaction and to the weight of the vehicle.

E

Train car model derivation

In this appendix it is presented the derivation of the vehicle-structure-interaction with the use of the contact forces as done in Youcef et al. [43]. Figure E.1 depicts the contact forces and the the DOFs used in the current derivation.

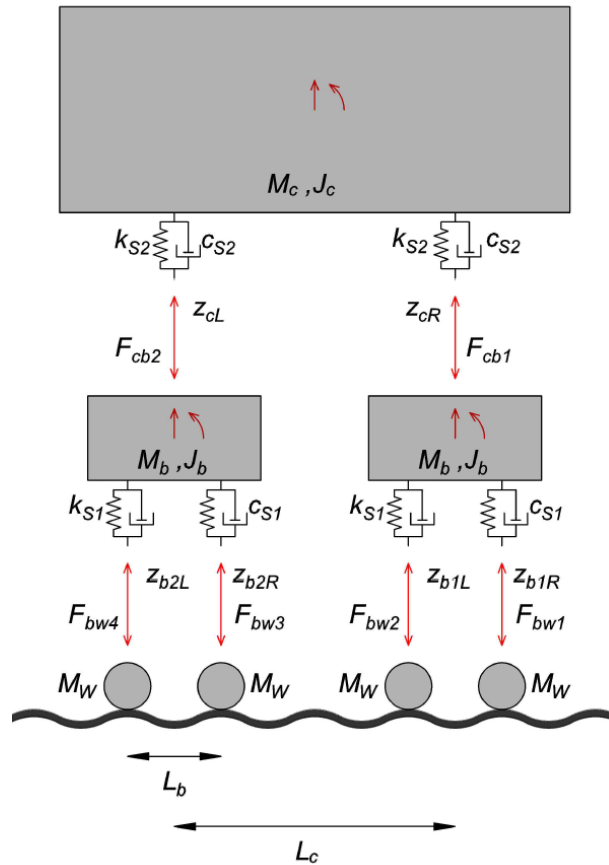


Figure E.1: Horizontal Displacement

The contact forces between the train car and the bogies are:

$$F_{cb1} = k_{S2}(z_{cR} - z_{b1}) + c_{S2}(\dot{z}_{cR} - \dot{z}_{b1}) \quad (\text{E.1a})$$

$$F_{cb2} = k_{S2}(z_{cL} - z_{b2}) + c_{S2}(\dot{z}_{cL} - \dot{z}_{b2}) \quad (\text{E.1b})$$

The contact forces between the bogies and the wheels are:

$$F_{bw1} = k_{S1}(z_{b1R} - z_{w1}) + c_{S1}(\dot{z}_{b1R} - \dot{z}_{w1}) \quad (\text{E.2a})$$

$$F_{bw2} = k_{S1}(z_{b1L} - z_{w2}) + c_{S1}(\dot{z}_{b1L} - \dot{z}_{w2}) \quad (\text{E.2b})$$

$$F_{bw3} = k_{S1}(z_{b2R} - z_{w3}) + c_{S1}(\dot{z}_{b2R} - \dot{z}_{w3}) \quad (\text{E.2c})$$

$$F_{bw4} = k_{S1}(z_{b2L} - z_{w4}) + c_{S1}(\dot{z}_{b2L} - \dot{z}_{w4}) \quad (\text{E.2d})$$

The equations of motions of the masses derived from the equilibrium of the forces are:

$$m_{car} \frac{L_c}{2} \ddot{z}_c + J_C \ddot{\varphi}_c + F_{cb1} L_c = 0 \quad (\text{E.3a})$$

$$m_{car} \frac{L_c}{2} \ddot{z}_c - J_C \ddot{\varphi}_c + F_{cb2} L_c = 0 \quad (\text{E.3b})$$

$$m_b \frac{L_b}{2} \ddot{z}_{b1} + J_b \ddot{\varphi}_{b1} - F_{cb1} \frac{L_b}{2} + F_{bw1} L_b = 0 \quad (\text{E.3c})$$

$$m_b \frac{L_b}{2} \ddot{z}_{b1} - J_b \ddot{\varphi}_{b1} - F_{cb1} \frac{L_b}{2} + F_{bw2} L_b = 0 \quad (\text{E.3d})$$

$$m_b \frac{L_b}{2} \ddot{z}_{b2} + J_b \ddot{\varphi}_{b2} - F_{cb2} \frac{L_b}{2} + F_{bw3} L_b = 0 \quad (\text{E.3e})$$

$$m_b \frac{L_b}{2} \ddot{z}_{b2} - J_b \ddot{\varphi}_{b2} - F_{cb2} \frac{L_b}{2} + F_{bw4} L_b = 0 \quad (\text{E.3f})$$

where

$$z_c = \frac{z_{cR} + z_{cL}}{2} \quad (\text{E.4a})$$

$$\varphi_c = \frac{z_{cR} - z_{cL}}{2} \quad (\text{E.4b})$$

$$z_{b1} = \frac{z_{b1R} + z_{b1L}}{2} \quad (\text{E.4c})$$

$$\varphi_{b1} = \frac{z_{b1R} - z_{b1L}}{2} \quad (\text{E.4d})$$

$$z_{b2} = \frac{z_{b2R} + z_{b2L}}{2} \quad (\text{E.4e})$$

$$\varphi_{b2} = \frac{z_{b2R} - z_{b2L}}{2} \quad (\text{E.4f})$$

and z_w and its derivatives can be computed as Equations (D.2) to (D.3b). Substituting Equations (E.1a) to (E.1b), Equations (E.2a) to (E.2d) and Equations (E.4a) to (E.4f) into Equations (E.3a) to (E.3f) it can be obtained the system of equations that will be used in the algorithm.

$$m_{car} \frac{L_c}{4} (\ddot{z}_{cR} + \ddot{z}_{cL}) + \frac{J_c}{L_c} (\ddot{z}_{cR} - \ddot{z}_{cL}) + c_{S2} L_c \left(\dot{z}_{cR} - \frac{\dot{z}_{b1R} + \dot{z}_{b1L}}{2} \right) + k_{S2} L_c \left(z_{cR} - \frac{z_{b1R} + z_{b1L}}{2} \right) = 0 \quad (\text{E.5a})$$

$$m_{car} \frac{L_c}{4} (\ddot{z}_{cR} + \ddot{z}_{cL}) - \frac{J_c}{L_c} (\ddot{z}_{cR} - \ddot{z}_{cL}) + c_{S2} L_c \left(\dot{z}_{cL} - \frac{\dot{z}_{b2R} + \dot{z}_{b2L}}{2} \right) + k_{S2} L_c \left(z_{cL} - \frac{z_{b2R} + z_{b2L}}{2} \right) = 0 \quad (\text{E.5b})$$

$$m_b \frac{L_b}{4} (\ddot{z}_{b1R} + \ddot{z}_{b1L}) + \frac{J_b}{L_b} (\ddot{z}_{b1R} - \ddot{z}_{b1L}) - c_{S2} L_c \left(\dot{z}_{cR} - \frac{\dot{z}_{b2R} + \dot{z}_{b2L}}{2} \right) - k_{S2} L_c \left(z_{cR} - \frac{z_{b2R} + z_{b2L}}{2} \right) + c_{S1} L_b (\dot{z}_{b1R} - \dot{w}_z - V w'_z - \lambda \dot{\varphi}_x - V \lambda \dot{\varphi}_x) + k_{S1} L_b (z_{b1R} - w_z - \lambda \varphi_x) = 0 \quad (\text{E.5c})$$

$$\begin{aligned}
& m_b \frac{L_b}{4} (\ddot{z}_{b1R} + \ddot{z}_{b1L}) + \frac{J_b}{L_b} (\ddot{z}_{b1R} - \ddot{z}_{b1L}) - \\
& c_{S2} L_c \left(\dot{z}_{cR} - \frac{\dot{z}_{b2R} + \dot{z}_{b2L}}{2} \right) - k_{S2} L_c \left(z_{cR} - \frac{z_{b2R} + z_{b2L}}{2} \right) + \\
& c_{S1} L_b (\dot{z}_{b1L} - \dot{w}_z - V w'_z - \lambda \dot{\varphi}_x - V \lambda \varphi'_x) + k_{S1} L_b (z_{b1L} - w_z - \lambda \varphi_x) = 0
\end{aligned} \tag{E.5d}$$

$$\begin{aligned}
& m_b \frac{L_b}{4} (\ddot{z}_{b2R} + \ddot{z}_{b2L}) + \frac{J_b}{L_b} (\ddot{z}_{b2R} - \ddot{z}_{b2L}) - \\
& c_{S2} L_c \left(\dot{z}_{cR} - \frac{\dot{z}_{b2R} + \dot{z}_{b2L}}{2} \right) - k_{S2} L_c \left(z_{cR} - \frac{z_{b2R} + z_{b2L}}{2} \right) + \\
& c_{S1} L_b (\dot{z}_{b2R} - \dot{w}_z - V w'_z - \lambda \dot{\varphi}_x - V \lambda \varphi'_x) + k_{S1} L_b (z_{b2R} - w_z - \lambda \varphi_x) = 0
\end{aligned} \tag{E.5e}$$

$$\begin{aligned}
& m_b \frac{L_b}{4} (\ddot{z}_{b2R} + \ddot{z}_{b2L}) + \frac{J_b}{L_b} (\ddot{z}_{b2R} - \ddot{z}_{b2L}) - \\
& c_{S2} L_c \left(\dot{z}_{cR} - \frac{\dot{z}_{b2R} + \dot{z}_{b2L}}{2} \right) - k_{S2} L_c \left(z_{cR} - \frac{z_{b2R} + z_{b2L}}{2} \right) + \\
& c_{S1} L_b (\dot{z}_{b2L} - \dot{w}_z - V w'_z - \lambda \dot{\varphi}_x - V \lambda \varphi'_x) + k_{S1} L_b (z_{b2L} - w_z - \lambda \varphi_x) = 0
\end{aligned} \tag{E.5f}$$

The mass, damping and stiffness matrices can be assembled as:

$$M = \begin{bmatrix} \frac{m_b}{4} + \frac{J_b}{L_b^2} & \frac{m_b}{4} - \frac{J_b}{L_b^2} & 0 & 0 & 0 & 0 \\ \frac{m_b}{4} - \frac{J_b}{L_b^2} & \frac{m_b}{4} + \frac{J_b}{L_b^2} & 0 & 0 & 0 & 0 \\ 0 & 0 & \frac{m_b}{4} + \frac{J_b}{L_b^2} & \frac{m_b}{4} - \frac{J_b}{L_b^2} & 0 & 0 \\ 0 & 0 & \frac{m_b}{4} - \frac{J_b}{L_b^2} & \frac{m_b}{4} + \frac{J_b}{L_b^2} & 0 & 0 \\ 0 & 0 & 0 & 0 & \frac{m_c}{4} + \frac{J_c}{L_c^2} & \frac{m_c}{4} - \frac{J_c}{L_c^2} \\ 0 & 0 & 0 & 0 & \frac{m_c}{4} - \frac{J_c}{L_c^2} & \frac{m_c}{4} + \frac{J_c}{L_c^2} \end{bmatrix}$$

$$C = \begin{bmatrix} c_{S1} + \frac{c_{S2}}{4} & \frac{c_{S2}}{4} & 0 & 0 & -\frac{c_{S2}}{2} & 0 \\ \frac{c_{S2}}{4} & c_{S1} + \frac{c_{S2}}{4} & 0 & 0 & -\frac{c_{S2}}{2} & 0 \\ 0 & 0 & c_{S1} + \frac{c_{S2}}{4} & \frac{c_{S2}}{4} & 0 & -\frac{c_{S2}}{2} \\ 0 & 0 & \frac{c_{S2}}{4} & c_{S1} + \frac{c_{S2}}{4} & 0 & -\frac{c_{S2}}{2} \\ -\frac{c_{S2}}{2} & -\frac{c_{S2}}{2} & 0 & 0 & c_{S2} & 0 \\ 0 & 0 & -\frac{c_{S2}}{2} & -\frac{c_{S2}}{2} & 0 & c_{S2} \end{bmatrix}$$

$$K = \begin{bmatrix} k_{S1} + \frac{k_{S2}}{4} & \frac{k_{S2}}{4} & 0 & 0 & -\frac{k_{S2}}{2} & 0 \\ \frac{k_{S2}}{4} & k_{S1} + \frac{k_{S2}}{4} & 0 & 0 & -\frac{k_{S2}}{2} & 0 \\ 0 & 0 & k_{S1} + \frac{k_{S2}}{4} & \frac{k_{S2}}{4} & 0 & -\frac{k_{S2}}{2} \\ 0 & 0 & \frac{k_{S2}}{4} & k_{S1} + \frac{k_{S2}}{4} & 0 & -\frac{k_{S2}}{2} \\ -\frac{k_{S2}}{2} & -\frac{k_{S2}}{2} & 0 & 0 & k_{S2} & 0 \\ 0 & 0 & -\frac{k_{S2}}{2} & -\frac{k_{S2}}{2} & 0 & k_{S2} \end{bmatrix}$$

F

Train car eigenvalue problem

In this appendix it is presented the eigenvalue problem of the vehicle. The mass, damping and stiffness matrices can be assembled as:

$$M = \begin{bmatrix} m_c & 0 & 0 & 0 & 0 & 0 \\ 0 & J_c & 0 & 0 & 0 & 0 \\ 0 & 0 & m_b & 0 & 0 & 0 \\ 0 & 0 & 0 & J_b & 0 & 0 \\ 0 & 0 & 0 & 0 & m_b & 0 \\ 0 & 0 & 0 & 0 & 0 & J_b \end{bmatrix}$$

$$C = \begin{bmatrix} 2c_{S2} & 0 & -c_{S2} & 0 & -c_{S2} & 0 \\ 0 & 2c_{S2} \frac{L_c^2}{4} & -c_{S2} \frac{L_c}{2} & 0 & c_{S2} \frac{L_c}{2} & 0 \\ -c_{S2} & -c_{S2} \frac{L_c}{2} & 2c_{S1} + c_{S2} & 0 & 0 & 0 \\ 0 & 0 & 0 & 2c_{S1} \frac{L_b^2}{4} & 0 & 0 \\ -c_{S2} & -c_{S2} \frac{L_c}{2} & 0 & 0 & 2c_{S1} + c_{S2} & 0 \\ 0 & 0 & 0 & 0 & 0 & 2c_{S1} \frac{L_b^2}{4} \end{bmatrix}$$

$$K = \begin{bmatrix} 2k_{S2} & 0 & -k_{S2} & 0 & -k_{S2} & 0 \\ 0 & 2k_{S2} \frac{L_c^2}{4} & -k_{S2} \frac{L_c}{2} & 0 & k_{S2} \frac{L_c}{2} & 0 \\ -k_{S2} & -k_{S2} \frac{L_c}{2} & 2k_{S1} + k_{S2} & 0 & 0 & 0 \\ 0 & 0 & 0 & 2k_{S1} \frac{L_b^2}{4} & 0 & 0 \\ -k_{S2} & -k_{S2} \frac{L_c}{2} & 0 & 0 & 2k_{S1} + k_{S2} & 0 \\ 0 & 0 & 0 & 0 & 0 & 2k_{S1} \frac{L_b^2}{4} \end{bmatrix}$$

The governing equation of the motion of the train car is then:

$$M\ddot{z} + C\dot{z} + Kz = 0 \quad (\text{E.1})$$

The damping is not considered when evaluating the eigenfrequencies and these can be found setting the determinant of the coefficients equal to zero and solving for ω :

$$\det(-\omega^2 M + K) = 0 \quad (\text{E.2})$$